UNIVERSITÀ
DEGLI STUDI
FIRENZE

International Doctorate in Atomic and Molecular Photonics
Ciclo XXIX

Coordinatore Prof. Roberto Righini

Tunable polymeric photonic structures

Settore Scientifico Disciplinare FIS/03

Dottorando
Dott. Sara Nocentini

Tutor
Prof. Diederik S. Wiersma

Coordinatore
Prof. Roberto Righini

2013–2016

Tunable polymeric photonic structures
International Doctorate in Atomic and Molecular Photonics, November 2016
Coordinator: Prof. Roberto Righini
Supervisor: Prof. Diederik S. Wiersma

Università degli Studi di Firenze
Laboratorio Europeo di Spectroscopia non Lineare
Via Nello Carrara 1, Sesto Fiorentino
50019 - Florence, Italy

Reviewers: Prof. Marc Brongersma and Prof. Martin Čopič

Preface

In the field of integrated micro-photonic devices, the progress in the lithographic techniques and the continuous advances in material science brought us to merge these two topics to study, analyze and fabricate tunable photonic components. Tunability, in fact, is a key block requirement to make dynamically reconfigurable structures and to reach this aim we addressed photo-responsitive polymers that allow a remote and non-invasive control of their optical properties. This thesis approached an intriguing class of materials and developed them towards photonic applications. After a concise description of the recent advances in photonic integrated circuits, advantages and disadvantages deriving from the use of polymers in such photonic devices are addressed together with the scopes of this work: to use a unique class of materials, liquid crystalline elastomers and to fabricate and study optically tunable photonic components, such as gratings and resonators. Among lithographic techniques, direct laser writing (DLW) allows for very flexible fabrication of micro scale objects with nanoscale precision. This technique is based on point-by-point polymerization induced by two-photon absorption in the focus of a pulsed high-power laser beam. A tiny voxel, the smallest polymerized volume element, defines the technique resolution. Moving the sample position in three dimensional space, the laser is able to polymerize - voxel by voxel- different photo-sensitive monomeric mixtures creating nearly any kind of 3D geometries. Direct laser writing has been used extensively in the past years to create photonic crystals and quasi-crystals. At the beginning of this research, the patterning of liquid crystalline elastomers in the microscale was not possible. In this work is demonstrated how, acting on both materials and writing parameters, it is possible to use them to create microstructured polymerized and cross-linked networks achieving very good resolutions, comparable with the other commercial resists. Liquid crystalline elastomer (LCEs) are smart polymers that combine the main features of liquid crystals with those of elastomers, thus inheriting the orientational order and sensitivity to different external stimuli from the former and elasticity and resilience to mechanical stresses from the latter. Among their unique characteristics, there is the ability to strongly deform in consequence of a given stimulus, like light, temperature, pH, electric or magnetic field. Such process is reversible, resulting hence in a shape memory material. To combine DLW and LCEs, a detailed study on the lithographic process and on liquid crystalline photoresists composition was necessary. They result in properly customized molecules and mixtures and in a

home-made calibration procedure. The possibility to retain contractive properties of the mixtures is demonstrated underlining LCE mixtures as good matrixes for tunable photo-elastic photonic devices realization by Direct Laser Writing technique, thanks to their high resolution, low degree of swelling, and broad range of parameters. The analysis on mechanical properties and light irradiation response of different LCEs, for instance by varying cross-linker percentage amount, underlined interesting behavior that can be tailored on demand to specific applications. In fact, different elastic moduli and response times emerged from the different polymeric structures both in the macro and micro scale for the different cross-linker percentages. Interestingly, it turned out that the mechanical properties observed on the macroscopic samples also reflected in the microscopic samples where materials with higher storage modulus presented smaller and slower responses in the micrometer scale. Furthermore, taking advantage from the wedged cell refractometer method an analysis on refractive index in dependence of temperature, crosslinking degree and dye percentage is presented determining the birefringence and the optical anisotropy for each studied mixture. In the second part of the thesis certain applications of LCE technology to photonics are presented. Namely we present applications as 2D tunable optical microstructured arrays and tunable beam steering devices. Angular deviation, photo-bleaching effects and temporal steering dynamics are deeply analyzed. Moreover, guided mode resonance filters (GMRF) are investigated: the first demonstration of a GMRF fabricated with LCE is here reported. Another class of photonic structure as whispering gallery mode resonators are approached both as polymeric passive and active cavities. In either cases, DLW is demonstrated as an excellent tool for their preparation. Passive cavities are carefully optically characterized and thanks to the DLW technique a polymeric three dimensional photonic integrated circuit, made of a single mode waveguide vertically coupled to a ring resonator, has been realized. To reach a tunable optical cavity, we exploit the shape change properties of LCE as a micro-actuator to remotely tune the lasing wavelength of a goblet micro laser. This thesis, at its end, presents a deep investigation of non conventional materials and techniques and their optimization and combination. With this technique, we demonstrate a new method to optically control the optical properties of different photonic structures that can be potentially integrated in many other different micro photonic devices.

Contents

CHAPTER 1

Polymeric Integrated Photonics: static and tunable elements

Photonics is continuously acquiring a dominant role in the new technologies, spreading from the well-known telecom and datacom platforms to sensors, from bio-medical applications to metrology studies. One of the most prominent development field is the realization of photonic devices in integrated circuits (ICs) for their numerous advantages respect to the electronic elements. In fact, to satisfy the requirements of low power consumption, large bandwidth, low prices in robust chip with greater functionalities, optical interconnections and devices are becoming a key enabling technology. In between the available technological platforms, polymers offer the possibility to overcome some drawbacks of silicon photonics. However this technology can not be considered as a substitute for the photonic semiconductor circuits but as a complementary strategy to reduce the power consumption, to introduce further functionalities and to connect the long distance fiber communication with the electronic chip as optical transceiver. In this chapter, the different photonic platforms will be briefly introduced with special attention to the capabilities of polymer components. We will underline the importance of tunable components to manipulate, control and stabilize the optical signal. In between the integrated photonic components that allow the transport and manipulation of light in the micro-scale, all the photonic crystal structures can not be forgotten. These well investigated structures will be studied and introduced to add some functionalities as beam steering or wavelength filtering.

1.1 Photonic Integrated Circuit platforms

The actual and alive research field of integrated optics is based primarily on the fact that light waves can propagate through well designed transparent materials. By combining together optical layers, and shaping them into appropriate configurations, integrated-

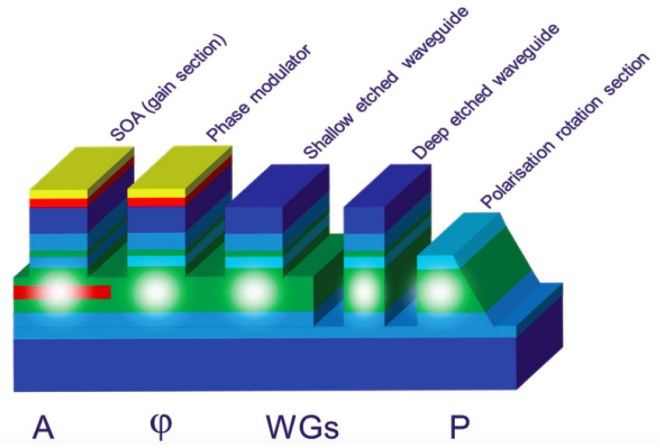

Fig. 1.1: Integration scheme of different building blocks on a single chip (Image from [1]).

optics technology has realized a large variety of components which can perform a wide range of operations. Thus, light can be guided, modulated, deflected, filtered, radiated into space or, by using laser action, it can also be generated within a thin-film structure. These components are small and compact and they can promote a variety of goals, of which the most promising is optical signal processing in optical communications. For this field, as for other related applications, the aim is to develop integrated devices having miniature dimensions, which are expected to be robust, durable, reliable and with low power consumption. Unlike Si-dominated electronic ICs, photonic integrated circuits, PICs, have been fabricated in a variety of host material systems, including elemental semiconductors (Si- and Ge-related), compound semiconductors (InP and gallium arsenide (GaAs)-based), dielectrics (SiO_2 and SiN_x-related), polymers and nonlinear crystal materials (e.g. $LiNbO_3$). The properties of different material systems place them into desirable but discrete functionality regimes. For example, InP and GaAs are flagship materials for light sources, while silica- and Si-based waveguides exhibit at least an order of magnitude lower propagation loss than III–V counterparts. The solution to mediate these peculiarities is the material integration. Due to the complex and multiple fabrication processes, integration can be more properly defined as heterogenization of the photonic circuits: a variety of different materials and waveguide platforms will be used on a single substrate, most notably silicon. The materials are typically integrated by a variety of techniques such as epitaxial growth, bonding, ion implantation and slicing, etch back or spin-on-glass. In this way, passive and active areas can be defined on the same substrate creating on chip lasers, phase modulators, waveguides and polarization controllers (Fig. 1.1). Both the generation, the manipulation and the analysis of the optical signal can be combined on a single chip. Transmitters and receivers are synthesized on the same substrate thank to complex fabrication procedures and different material properties. Through these fundamental functions the main building blocks of an integrated circuit can be achieved. Passive components as waveguides, ring resonator (RR) filters, array waveguide gratings (AWGs) and multimode interference (MMI) couplers can be realized both on InP, Silicon and SiN substrates, while to obtain active components as laser, switches and modulators, InP and Silicon should be addressed.

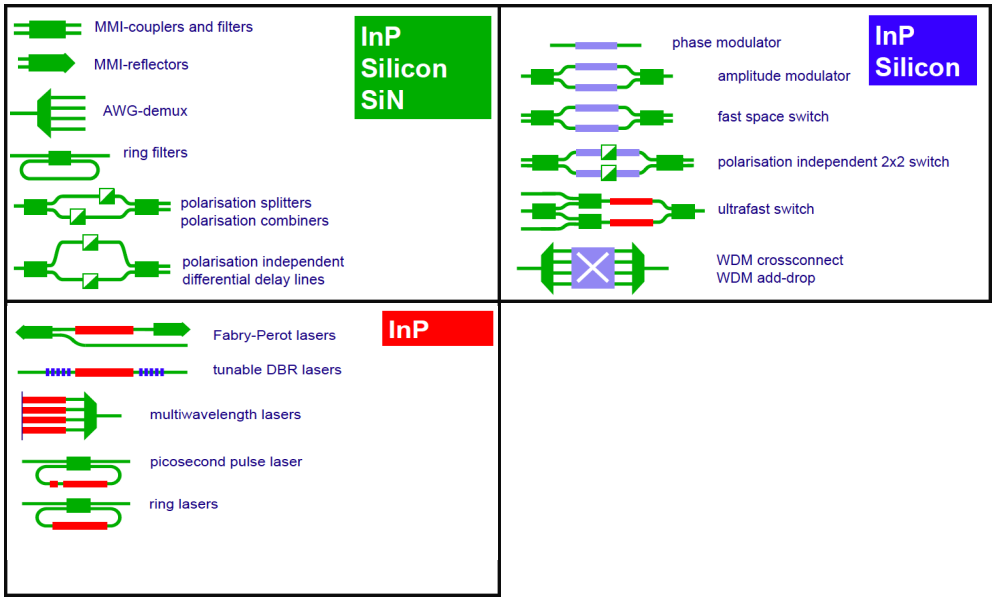

Fig. 1.2: Scheme of the constituent material of different building blocks on a photonic chip.

A grafic scheme is reported in Figure 1.2. However it is important to notice that for active devices, like lasers and modulators, InP performs far better than silicon-based technologies despite recent and hard won advances in the field. At the same time a lot of efforts have been accomplished towards the integration of light sources in the silicon platforms and recently some examples have been reported in literature [2, 3].
The continuous research growth into the photonic technologies is pushed forward by the numerous fields of application. More than 450 B$ are invested each year, already the 20% of the electronic market. The most attractive field at the moment is the next generation telecom and datacom system but not less important are all the sensors and security applications like surveillance, in-line inspection of manufacturing, monitoring of construction and especially the medical sector. Before addressing the research of this work focused on the polymer photonics, an overview of some examples of photonic integrated circuits, already available on the market is shown in Fig. 1.3. Optical micro-components can be integrated to handle optical data, to analyze signals from fiber sensors, for medical and bio-imaging, in lasers, to create optical switching and become connectors from the fiber net to home users. There is a steady increase in the move from electrical to optical technologies. It is likely that optical technology will spread to the very shortest intra-chip distances (eventually) in response to the demands posed by increases in data rates.

1.2 Silicon Photonics vs Polymer Photonics

The main technologies currently used in photonic integration are typically categorized as Silicon, III-V Material and Dielectric Photonics.
The III-V Materials technology platform offers light amplification and detection, next

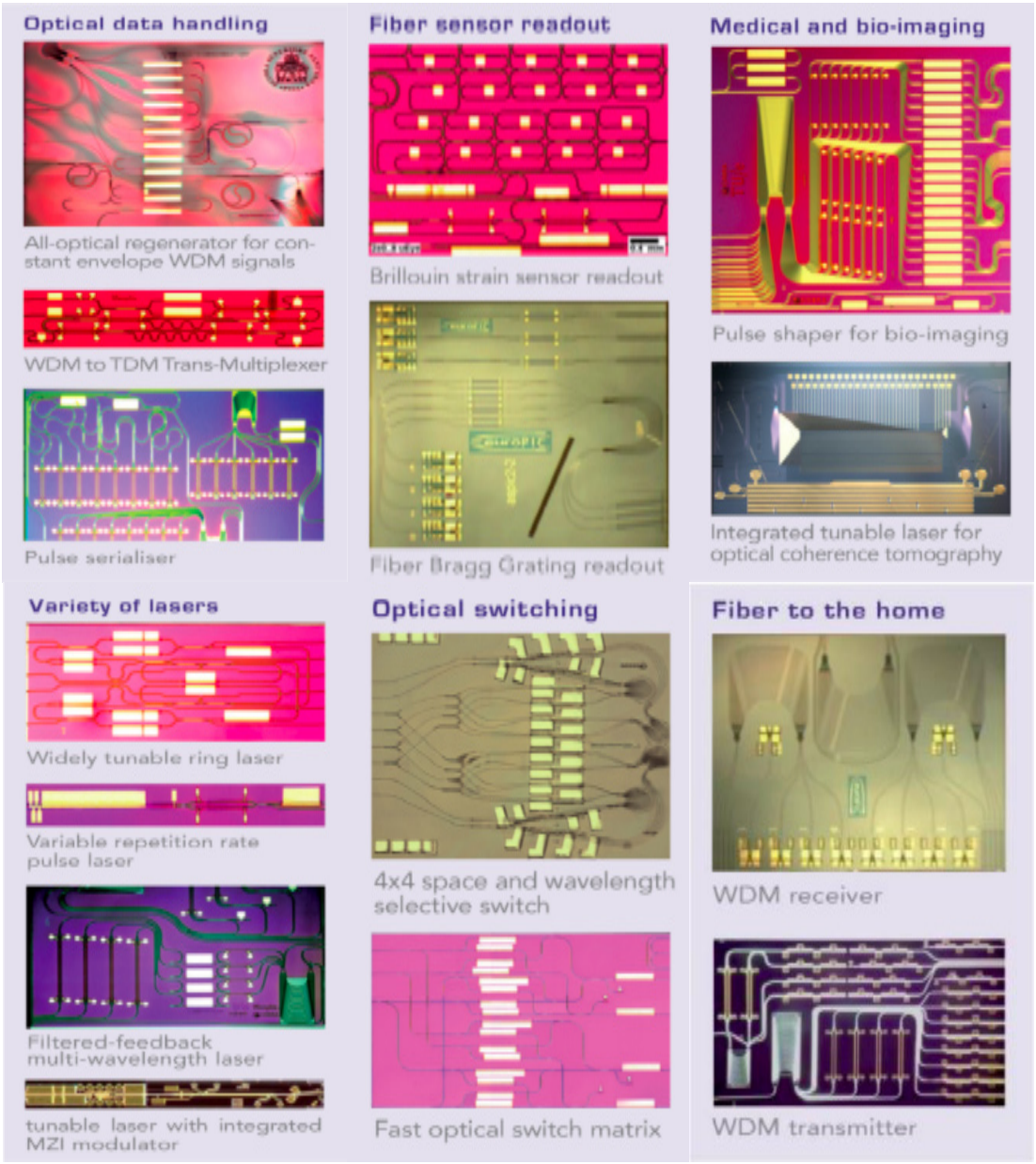

Fig. 1.3: Application of photonic integrated circuits: some examples.

to passive light manipulation as filtering, splitting or interfering. In the past 20 years, this technology has been widely used by chip manufacturers to make lasers, modulators and detectors. The main materials for this platform are Indium Phosphide (InP) and Gallium Arsenide (GaAs).
Silicon Photonics, using Silicon-on-Insulator, offers passive light manipulation at a very small footprint, allowed by the relative high contrast index of silicon. The small chip size and the CMOS fabrication compatibility result as great advantages. However, light amplification has been achieved only in low-dimensional systems [4, 5], adding active impurities in the lattice [6] or in silicon nanocrystals [7]. Since silicon is not transparent for wavelengths below 1 μm, Silicon Photonics can not be used for visible light applications. Silicon platforms have still a prominent role in the photonic application field thanks to compatible processing protocols currently used in the microelectronic industry. It results as an already affirmed technology that benefits of the vast microelectronic infrastructures leading to the integration of photonic and electronic functionality in a cost-effective and monolithic manner [8, 9]. The remarkable characteristic of silicon is the high refractive index that allows to tightly confine the electric field squeezing the photonic structure dimensions. In fact, the waveguide core can be shrunk down to a submicron cross-section, while still maintaining good mode confinement at the wavelengths of $1.3 - 1.55\,\mu$m. At the same time, such extreme light confinement allows the minimal bent radius to be reduced to the micron range. However, the higher the refractive index contrast the higher the sensitivity to waveguide imperfections [10]. This introduces propagation losses due to the waveguide roughness but it is not the only loss source. The other contribute to propagation losses is due to the high nonlinear two-photon absorption, that bulk and amorphous crystalline silicon suffers [11, 12], in all telecommunication bands with wavelengths shorter than about 2000 nm. This represents a fundamental limitation, being an intrinsic property of silicon's band structure.
A promising platform that solves this request exhibiting low, linear and non-linear, losses is Silicon Nitride (Si_3N_4). Other properties that make Si_3N_4 highly attractive is the CMOS fabrication compatibility, the high stability, good optical properties and the ability to engineer the optical dispersion. Among the dielectric technologies, it shows the highest refractive index (around 2 at telecom wavelength) which hence allows a good field confinement.
The other main materials for dielectric platform are Silicon Dioxide or Silica (SiO_2), TripleX™ and polymers. In particular, polymer active and passive optical components have shown potentials for enabling economically viable optical systems crucial combined with good optical properties and the possibility of integration on different substrates with different lithographic technique. For example polymer waveguide materials can be highly transparent, and the absorption loss can be made below 0.1 dB/cm at all key communication wavelengths [13]. The refractive index of most polymers $(1.5 - 1.7)$ is nearly matched to that of glass optical fibers $(1.5 - 1.6)$ enabling small Fresnel reflection loss at the interfaces in butt-coupling configuration of waveguides and fibers. If we compare the polymer platform with the other already introduced, several advantages emerge. First, the properties of polymers can be widely tuned by chemically modifying the structure of the monomer, the functional groups or chromophores, or the polymer backbones. Second, polymeric materials can be easily manipulated by several conventional or frontier fabrication techniques. Third, compared to semiconductor chips, polymeric materials

provide for easy and low-cost fabrication of optical devices. Fourth and more important, functional polymeric materials provide an excellent platform for integrating several diversified materials with different functions. Summing up, optical polymers are considered as a particularly attractive material for integrated photonic circuits because of their rapid processability, low costs, high performance (good transparency, no birefringence or large birefringence depending on the desired application) and even more important they provide an ideal platform for the incorporation of more complex material functionalities [14]. This is the key point our work is addressing: combining materials with different chemical and physical properties to obtain a completely reconfigurable optical device.

1.3 Polymer Integrated Photonics

Polymeric integrated optical devices include different photonic structures; among them, the fundamental building block is the waveguide. An optical polymer waveguide guides the light on the photonic chip for total internal reflection that is guaranteed by the refractive index contrast with the substrate or the cladding. Such element can be employed in the realization of other common structures like beam splitters, directional couplers, ring resonators and multimode interference devices. The mostly used lithographic techniques are e-beam lithography, optical-lithography and laser writing techniques.
The polymer optical properties define the behavior of light inside the structure by tuning the chemical and physical properties of the materials. They can be chosen and optimized to nicely match the requested functionalities. The most important parameter is the refractive index that determines the mode propagation inside the structures. It depends on the chemical composition of the material, on the molecular orientational order (determining the optical anisotropy, i. e. the birefringence) and on the fabrication parameters. To elucidate this last dependence, the laser writing technique is considered: in this case, the polymerization degree, that determines the material density and therefore the refractive index, is affected by the writing speed and the polymerization laser power (see Paragraph 2.1.1). The refractive index is not a material fixed value, it exhibits a relevant dependence on the temperature variation, on the humidity degree and on the optical dispersion. Other important polymer properties are the optical losses, the mechanical properties as rigidity or elasticity and the thermal stability.
All these properties should be considered depending on the photonic structure to be realized.
In literature, examples of optical interconnections between chips can be found. In this case, the advantage in using optical interconnects comes from their dielectric nature that does not limit the communication speed and the integration density due to the low power dissipation (drawback that strongly affects electronics). Samples realized both with direct laser writing [15] and mask lithography techniques [16] have been proposed. While considering the photonic passive components that can be integrated on a chip, we referred to waveguides, splitter, directional couplers and array waveguide grating (AWG) as planar elements for wavelength division multiplexing. Another important function that should be included on chip, is filtering. This is usually obtained through whispering gallery mode resonators [17] for small bandwidth or combined ring resonators (side coupled integrated spaced sequence of resonator, SCISSOR) for a broadband transfer function [18].

(a) (b)

Fig. 1.4: (a) LCE molecule nematic network on the left. With an external stimulus (temperature, light, electric field..), the material contracts along the director and expands in the perpendicular plane elastically. It recovers the initial shape, once the stimulus is turned off. (b) An example of a LCE micro-robot (Image from the cover page of Adv. Mat. 27, 26 (2015)).

On the other side, to dynamical control circuit optical properties, active elements as switches and Mach-Zehnder interferometers can be added. To address this request electro-active polymers are usually employed.

1.3.1 Liquid Crystal Elastomers for innovative photonics

Liquid crystals constitute a fascinating class of soft condensed matter characterized by the counterintuitive combination of fluidity and long-range order. Today they are best known for their exceptionally successful application in flat panel displays. However, the use of liquid crystals in photonic devices also deserve some drawbacks. The most evident one is their fluid consistence, which requires proper encapsulation schemes in order to confine the LC close to the active region – for instance, the pixel element of a screen. This drawback can be overcome with a unique material science concept, that of liquid crystalline elastomer (LCE). In LCE, the mesogenic liquid crystal units are incorporated in a crosslinked polymer, thus forming a flexible but selfstanding molecular network [19, 20]. These materials merge the essential properties of an ordinary liquid crystal, like optical birefringence, responsivity to electrical stimuli and temperature, with a unique shape morphing behavior. In this work, working towards the realization of a light-controlled photonic device, we use a laser source as external stimulus. The resulting deformation, under the stimulus exposure, for nematic liquid crystal (with a preferential molecular alignment direction, called director), is a contraction along the director and an expansion in the perpendicular plane as shown in Figure 1.4.a. These peculiarities have been harnessed to devise novel classes of sensors and actuators [21], which also leverage on the possibility to be structured in a complex three-dimensional fashion [22], to include functional composites [23] and to be driven optically [24, 25].
The application of LCE in photonic devices is still in its infancy, but it is likely to assume a leading role in the next few years. Indeed, one of the most challenging issues – that is, the fabrication of LCE nanostructures - has been recently tackled by means of the direct laser writing technique (see figure 1.4.a) [26, 27]. However, the quality of the fabricated nanostructures is not yet comparable with that of nanostructures realized from more conventional materials, and the photonic designer must tackle with some

compromises until further technological improvements would guarantee a full control over the nanoscale geometry. In this work, LCE material studies and improvements have been accomplished so that tunable photonic structures have been realized.

1.3.2 Tunable components

Photonic integrated circuits that bend, split, couple, and filter light have been demonstrated on different platforms. However, these structures are usually passive, which means that their optical properties are predetermined by the structure design and thus cannot be modified once fabricated. Switches and modulators have been demonstrated by employing III–V compound materials based on photoexcited free-carrier concentrations resulting from one- or two-photon absorption [28]. In silicon, switching has been shown only by use of extremely high powers [29] in large or nonplanar structures that are inappropriate for effective on-chip integration.
The purpose of this work is to use the possibility to functionalize polymers in such a way to fabricate devices whose optical properties could be tuned or switched in response to an external stimulus. This is a key-feature that is requested both in fundamental physical experiments and in real commercial devices. Among the optical elements that have been introduced, tunability is a particularly interesting feature for whispering gallery mode resonators (WGMR). The other structure that requires intrinsically a dynamic control in its working mechanism is the Mach-Zehnder interferometer [30] that are predominantly driven by an electro-optic effect. Mach-Zehnder interferometers and a delay ring resonator in one of its arms can also be combined in a configuration, the so called ring loaded Mach-Zender interferometer [31]. This arrangement might perform as an interleaver filter or as an optical filter with a flat response, depending on the length of the ring and the path difference at the upper and lower branches.
The peculiar and attractive features of WGMR are the small resonant mode volume and the high quality factors, that hence create sharp spectral resonances. Numerous attempts have been made to develop an active microring resonator to achieve optical operational functions such as optical modulation [32, 33] and optical bistability [34, 35]. The most common tuning methods are based on electro-optic effect [36], thermo-optic effect [37], free carrier injection (in semiconductors) [32], mechanical deformation [38] and liquid crystal layer deposition [39, 40]. The above mentioned strategies are associated with problems like high power consumption, low integrability due to on chip invasive structures, small tuning range and operational speed limitation. The two quantities in WGMRs that can be controlled after the fabrication process and determine the resonant wavelength are the cavity radius and the refractive index. However with less invasive techniques is difficult to achieve a reversible tuning over the whole free spectral range (FSR). In fact, electrical thermo-optic tuning of a $75\,\mu$m diameter microtorus over up to 30% of a FSR has been demonstrated [37]. It relies on the temperature dependence of the refractive index of silica, $\partial n/\partial T = 1.3 \cdot 10^{-5\circ} K^{-1}$. Another solution for tuning is to elastically deform the resonator through mechanical strain. For a diameter of $80\,\mu m$ microsphere, tuning over 50% of an FSR has been achieved with this method, limited by the mechanical damage threshold of the resonator setup [38]. Finally, it should be noted that for a $50\,\mu m$ diameter equatorial WGM with Q = 109 (very low quality factor) the resonance linewidth is only 10^{-7} of a FSR. Therefore, even if a tuning device reached a

full FSR tuning range, it would be a challenging task to guarantee the corresponding passive stability.
Here, we propose to tune the optical properties of high quality factor WGMRs through a remote optical control. In this way, no additional structure should be implemented on chip since the laser beam triggers the tunable response of the resonator. The transducer that converts the light into a mechanical deformation is a micro-structured actuator made of a soft elastic material, a liquid crystalline elastomeric micro-cylinder. This application will be deeply discussed in Chapter 5.

References

[1] M. Smit et al. "An introduction to InP-based generic integration technology". In: *Semiconductor Science and Technology* 29.8 (2014), p. 083001.

[2] Z. Zhou, B. Yin, and J. Michel. "On-chip light sources for silicon photonics". In: *Light: Science & Applications* 4.11 (2015), e358.

[3] D. Liang and J. E. Bowers. "Recent progress in lasers on silicon". In: *Nature Photonics* 4.8 (2010), pp. 511–517.

[4] A. Cullis and L. Canham. "Visible light emission due to quantum size effects in highly porous crystalline silicon". In: *Nature* 353 (1991), pp. 335–338.

[5] K. Hirschman et al. "Silicon-based visible light-emitting devices integrated into microelectronic circuits". In: *Nature* 384.6607 (1996), pp. 338–341.

[6] G. Franzo et al. "Room-temperature electroluminescence from Er-doped crystalline Si". In: *Applied physics letters* 64.17 (1994), pp. 2235–2237.

[7] L. Pavesi et al. "Optical gain in silicon nanocrystals". In: *Nature* 408.6811 (2000), pp. 440–444.

[8] L. Kimerling et al. "Electronic-photonic integrated circuits on the CMOS platform". In: *Integrated Optoelectronic Devices 2006*. International Society for Optics and Photonics. 2006, pp. 612502–612502.

[9] R. Soref. "The past, present, and future of silicon photonics". In: *IEEE Journal of selected topics in quantum electronics* 12.6 (2006), pp. 1678–1687.

[10] F. Morichetti et al. "Roughness induced backscattering in optical silicon waveguides". In: *Physical review letters* 104.3 (2010), p. 033902.

[11] S. Grillanda and F. Morichetti. "Light-induced metal-like surface of silicon photonic waveguides". In: *Nature communications* 6 (2015).

[12] J. Leuthold, C. Koos, and W. Freude. "Nonlinear silicon photonics." In: *Nature Photonics* 4.8 (2010).

[13] H. Ma, A.-Y. Jen, and L. R. Dalton. "Polymer-Based Optical Waveguides: Materials, Processing, and Devices". In: *Advanced materials* 14.19 (2002), pp. 1339–1365.

[14] M. Lee et al. "Broadband modulation of light by using an electro-optic polymer". In: *Science* 298.5597 (2002), pp. 1401–1403.

[15] N. Lindenmann et al. "Photonic wire bonding: a novel concept for chip-scale interconnects". In: *Optics express* 20.16 (2012), pp. 17667–17677.

[16] R. Dangel et al. "Polymer waveguides for electro-optical integration in data centers and high-performance computers". In: *Optics express* 23.4 (2015), pp. 4736–4750.

[17] G. Righini et al. "Whispering gallery mode microresonators: fundamentals and applications". In: *Rivista del Nuovo Cimento* 34.7 (2011), pp. 435–488.

[18] J. E. Heebner and R. W. Boyd. "'Slow'and'fast'light in resonator-coupled waveguides". In: *Journal of modern optics* 49.14-15 (2002), pp. 2629–2636.

[19] H. Finkelmann, H.-J. Kock, and G. Rehage. "Investigations on liquid crystalline polysiloxanes 3. Liquid crystalline elastomers—a new type of liquid crystalline material". In: *Die Makromolekulare Chemie, Rapid Communications* 2.4 (1981), pp. 317–322.

[20] F. Brömmel, D. Kramer, and H. Finkelmann. "Preparation of liquid crystalline elastomers". In: *Liquid Crystal Elastomers: Materials and Applications*. Springer, 2012, pp. 1–48.

[21] C. Ohm, M. Brehmer, and R. Zentel. "Liquid crystalline elastomers as actuators and sensors". In: *Advanced Materials* 22.31 (2010), pp. 3366–3387.

[22] L. T. de Haan, A. P. Schenning, and D. J. Broer. "Programmed morphing of liquid crystal networks". In: *Polymer* 55.23 (2014), pp. 5885–5896.

[23] M. Chambers et al. "Liquid crystal elastomer–nanoparticle systems for actuation". In: *Journal of Materials Chemistry* 19.11 (2009), pp. 1524–1531.

[24] M.-H. Li et al. "Light-Driven Side-On Nematic Elastomer Actuators". In: *Advanced Materials* 15.7-8 (2003), pp. 569–572.

[25] T. Ikeda, J.-i. Mamiya, and Y. Yu. "Photomechanics of liquid-crystalline elastomers and other polymers". In: *Angewandte Chemie International Edition* 46.4 (2007), pp. 506–528.

[26] H. Zeng et al. "Light-Fueled Microscopic Walkers". In: *Advanced Materials* 27.26 (2015), pp. 3883–3887.

[27] H. Zeng et al. "High-resolution 3D direct laser writing for liquid-crystalline elastomer microstructures". In: *Advanced materials* 26.15 (2014), pp. 2319–2322.

[28] T. A. Ibrahim et al. "Lightwave switching in semiconductor microring devices by free carrier injection". In: *Journal of lightwave technology* 21.12 (2003), p. 2997.

[29] H. Tsang et al. "Optical dispersion, two-photon absorption and self-phase modulation in silicon waveguides at 1.5 μm wavelength". In: *Applied Physics Letters* 80.3 (2002), pp. 416–418.

[30] J. Liu et al. "Recent advances in polymer electro-optic modulators". In: *Rsc Advances* 5.21 (2015), pp. 15784–15794.

[31] K. Oda et al. "A wide-band guided-wave periodic multi/demultiplexer with a ring resonator for optical FDM transmission systems". In: *Journal of lightwave technology* 6.6 (1988), pp. 1016–1023.

[32] V. R. Almeida et al. "All-optical control of light on a silicon chip". In: *Nature* 431.7012 (2004), pp. 1081–1084.

[33] L. Fan et al. "An all-silicon passive optical diode". In: *Science* 335.6067 (2012), pp. 447–450.

[34] Q. Xu and M. Lipson. "Carrier-induced optical bistability in silicon ring resonators". In: *Optics letters* 31.3 (2006), pp. 341–343.

[35] Y. Yu et al. "Optical-force-induced bistability in nanomachined ring resonator systems". In: *Applied Physics Letters* 100.9 (2012), p. 093108.

[36] T.-J. Wang, C.-H. Chu, and C.-Y. Lin. "Electro-optically tunable microring resonators on lithium niobate". In: *Optics letters* 32.19 (2007), pp. 2777–2779.

[37] D. Armani et al. "Electrical thermo-optic tuning of ultrahigh-Q microtoroid resonators". In: *Applied physics letters* 85.22 (2004), pp. 5439–5441.

[38] W. von Klitzing et al. "Tunable whispering gallery modes for spectroscopy and CQED experiments". In: *New journal of physics* 3.1 (2001), p. 14.

[39] B. Maune et al. "Electrically tunable ring resonators incorporating nematic liquid crystals as cladding layers". In: *Applied physics letters* 83.23 (2003), pp. 4689–4691.

[40] C.-T. Wang et al. "Optical bistability in a silicon nitride microring resonator with azo dye-doped liquid crystal as cladding material". In: *Optics express* 21.9 (2013), pp. 10989–10994.

CHAPTER 2

Materials and techniques for polymer micropatterning

The main constituent materials studied in this work are polymers with peculiar properties that have been shaped with two different lithographic techniques turning them into on-chip micro-optical components.
In this chapter, the chemical and physical material properties are introduced, in addiction, the potentialities and limitations of the lithographic techniques are discussed. We focus the attention on the three-dimensional lithographic technique named Direct Laser Writing (DLW). A brief introduction about the electron beam technique (EBL) is also given.

2.1 Lithographic techniques

In the telecommunication band, both photonic wires and photonic crystals have dimensions and features of hundred nanometers. However, the accuracy required for the fabrication is even higher; roughness induced losses and the deviation from the perfectly periodic structure affect significantly the mode propagation. For research purposes, nanophotonic components with the highest resolution are traditionally fabricated using e-beam lithography. While this is a very accurate technique, it is slow and unsuitable for mass-fabrication. In fact for commercial applications, conventional photolithography, as used for the fabrication of current photonic ICs, is employed but lacks the resolution to define many nanophotonic structures. Deep UV lithography at 248 nm or 193 nm, the technology used for advanced CMOS fabrication, offers both the resolution and throughput needed for commercial applications. To reach our purposes of material integration and three-dimensional structures, e-beam lithography and direct laser writing provide all the required characteristics and possibilities to address our requests.

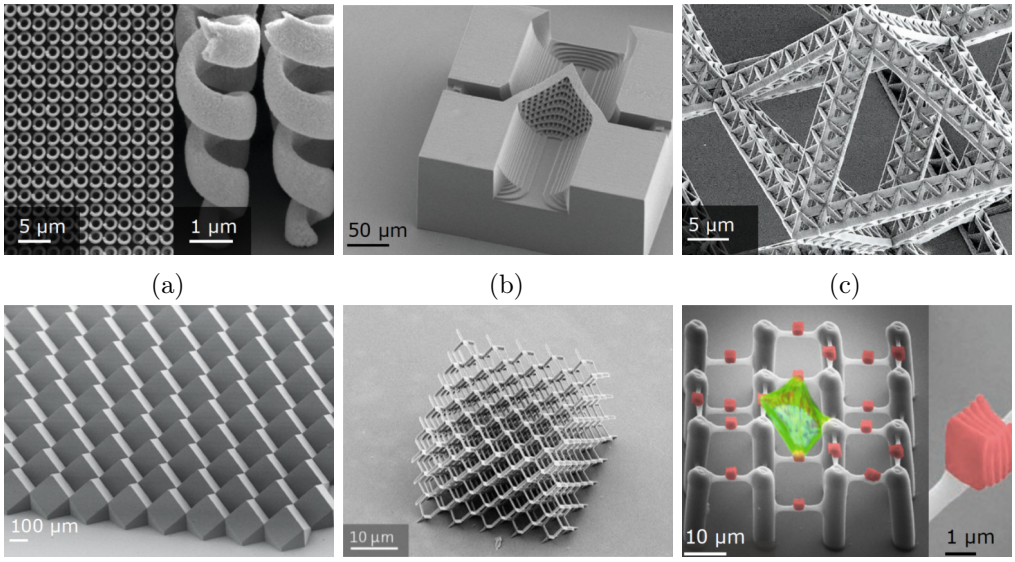

Fig. 2.1: SEM pictures of structure realized by the DLW on different materials and substrates: (a) a tapered gold-helix metamaterial structure as improved circular polarizer [10], (b) a micro porous filter in SU-8, (c) a fractal-like mechanical structure [11] (d) an optical reflector, (e) a 3D photonic crystal and (f) a cell scaffold for cell growing with of a cell-repellent material (grey) and a cell adhesion promoting material (red)[12].

2.1.1 Direct Laser Writing

Direct laser writing (DLW) is an unique lithographic technique based on ultra-localized polymerization. It consents to produce 3D micro/nano-structures for diverse applications in microoptics [1, 2], photonics [3–5], micro-fluidics [6] and biomedicine [7]. Furthermore, it allows integration of several components and combination of a few of the above mentioned functions [8, 9].

DLW technique is attractive for its flexibility to materialize differentiated 3D models (also using CAD platform) out of a wide spectrum of materials on the desired substrates [9, 13–15]. Scanning electron micrograph (SEM) images of different structures realized are shown in Figure 2.1. DLW technique allows to patter many geometries on different polymers opening to applications in many fields.
It is based on a non-linear photo-polymerization process that allows to transform the liquid resist in the desired polymeric structure. Laser induced photo-crosslinking can be achieved by tightly focusing ultra short pulses into photo-sensitive mixtures [16]. A point-by-point exposure of the material to laser radiation allows rapid prototyping of fully 3D structures with sub micrometer spatial resolution. In 3D DLW, a pulsed[1] laser is focused into a diffraction-limited spot within the volume of a thick-film/drop photoresist. By exploiting two-photon absorption, the effectively exposed volume is restricted to the focal region and only in the central part of the laser spot, the light intensity overcomes

[1] DLW has been demonstrated for pulsed laser but also for continuous one [17]

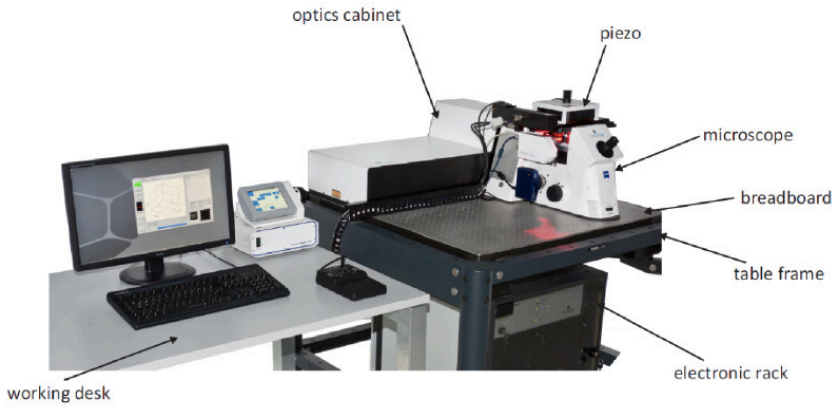

(a)

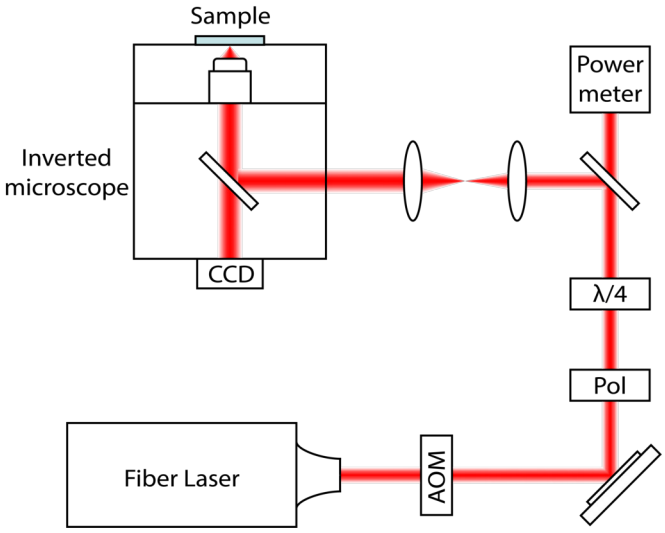

(b)

Fig. 2.2: Direct Laser Writing setup:(a) a photo and (b) a representation scheme.

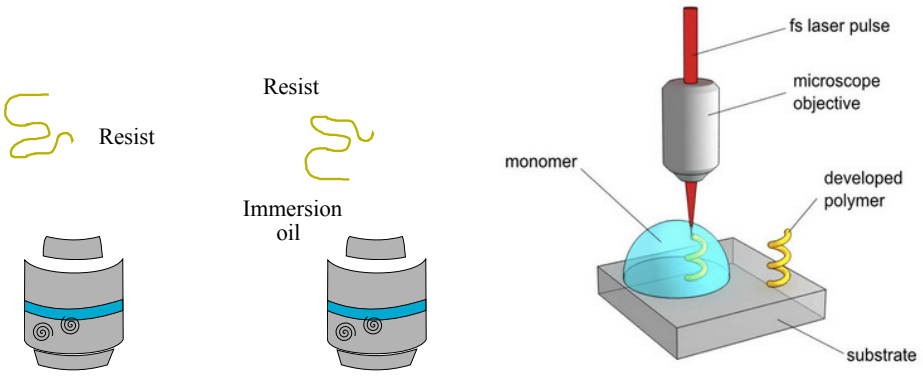

Fig. 2.3: Direct Laser Writing setup: (a) the difference in between the "standard" configuration, on the right, and the reversed one (DiLL system), on the left. (b) The laser polymerization effect in the resist drop.

the polymerization threshold. This threshold process leads to the polymerization of an ellipsoidal volume element, the “voxel” (in analogy to the picture element commonly referred as pixel) (Fig. 2.3.a). The size and shape of these so-called voxels depend on the iso-intensity surfaces of the microscope objective, and the exposure threshold for multiphoton processes of the photosensitive medium. Thanks to this non-linearity the achieved lateral resolution is 120 nm [18].
Higher resolutions have been demonstrated introducing the concept of stimulated emission depletion exported from fluorescence optical microscopy by S. Hell [19]. If this idea is applied to optical lithography, the depletion DLW system (STED-DLW [20]) allows, inhibiting partially the polymerization and then effectively reducing the photoresisit sensitivity, to reach a lateral resolution of 65 nm. Additionally, beam shaping techniques employing spatial light modulators (SLM) or diffractive optical elements (DOEs) can be used to obtain parallel processing and dramatically increase fabrication throughput [21]. But the high resolution is not the more remarkable feature of this lithographic technique. In fact, respect to UV photo-lithography, it boasts to be a mask-less system that in a single process creates a 3D structure. The unique possibility of fabricating three dimensional structures, also employing different materials, is the key feature that differentiates DLW from e-beam lithography. Moreover being a mask-less system, with a simpler setup than the EBL one, DLW is a cheap lithographic system also because of the reduced costs of polymeric resists.
The DLW commercial workstation used for the sample fabrication inside this study, is the Photonic Professional system (Figure 2.2.a) (Nanoscribe GmbH). Two-photon absorption polymerization is induced by a focused laser beam from pulsed erbium doped femtosecond (120 fs) fiber laser source at a center wavelength of 780 nm with a repetition rate of 100 MHz. The laser beam is then tightly focused through an immersion oil objective (Plan Apocromat, NA 1.4, Carl Zeiss,Oberkochen, Germany) into a cell when the photosensitive resist is dropped or spin-coated. A schematic representation of the DLW system is reported in Figure 2.2.b.
Two different objective configurations (see Fig. 2.3.a) are possible within this system: a

normal one where the high NA immersion objective is in contact with the glass substrate through a drop of refractive index matching oil; while the reversed configuration (DiLL system) provide the possibility to use a special resist as matching oil and the structures can be realized up side down. This latest method allows to decrease the shrinkage of the structure and to fabricate really tall stable structures [22].

Two-Photon Absorption Polymerization

Photo-polymerization refers to polymerization reaction (mainly based on chain growth) that is initiated by light absorption. Such process allows to transform single molecules, maintained in their liquid state, into a polymeric, solid and insoluble material. Moreover, polymerization can be followed, or proceed with, cross-linking processes: different polymer chains are connected each other, under illumination, affording more rigid structures. In order to promote radical formation, molecules, that form initiating species of radicals or cations by absorbing photons, are added. Such small molecules are called photo-initiators and they play the important role of polymerization starters. After the polymeric chain termination, once two radical chains neutralize each other, the polymer backbone network is realized and the material acquires a solid phase. The physical, chemical and mechanical properties of the solidified resin strictly depend on the nature and structure of the different monomers. 3D lithography is achieved through a non linear process: two-photon absorption (TPA). TPA is a quantum mechanical three-body process, where an electron absorbs two photons simultaneously to transcend the energy gap in one excitation event. In the case of TPA photopolymerization, when the sum of the two absorbed photons is resonant with the transition, photo-initiators are excited to triplet states and decay into radicals that trigger the polymerization (Figure 2.4.a). In fact they promote the formation of a radical that, reacting with monomers in a cascade process, forms a monomer radical chain and it will be neutralized with another radical to form a polymeric chain. A fundamental quantity in TPA polymerization is the photo-polymerization threshold that is determined by the production efficiency of radicals from excited triplet states, which is characterized by the quantum yield of polymerization. The reactions that produce radicals should compete with monomer quenching, oxygen quenching and other pathways of deactivation of the excited states like phosphorescence emission. The threshold is also determined by the reactivity of radicals and monomers. Experimentally, it has been demonstrated that the predominant role in radical quenching is played by oxygen and also the duration of polymerization reaction is largely dominated by oxygen quenching [23]. The other threshold that defines the dynamic range is the laser induced breakdown. It causes an ablation process at sample surface and micro-explosion inside the bulk; it is detrimental to photo-polymerization because breakdown-induced resin bubbling damages existing structures and prevents further reactions. For our studies, the non linear polymerization threshold is particularly important because it defines the possibility of creating a 3D voxel and, at the same time, the power range of monomer activation. This under-diffraction limit resolution is achieved thank to the non-linear process that, due to the squared intensity I dependence of the two photon absorption cross section, allows the excitation to be localized within the focal volume of the laser beam. To understand better which are the parameters that influence the voxel dimension and therefore the resolution, it is important to remember

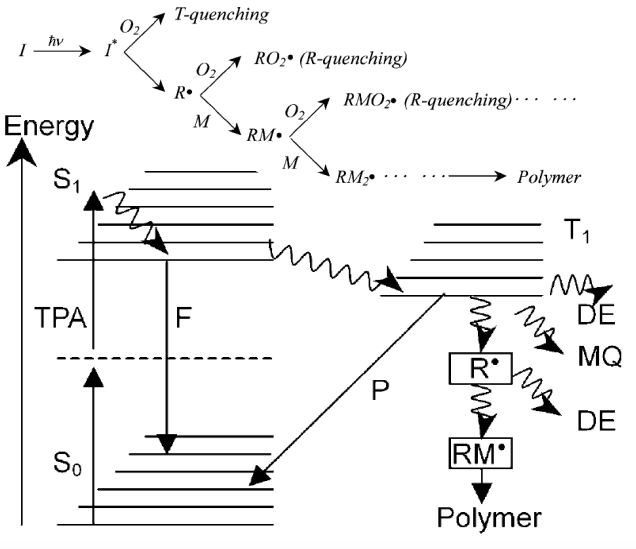

(a)

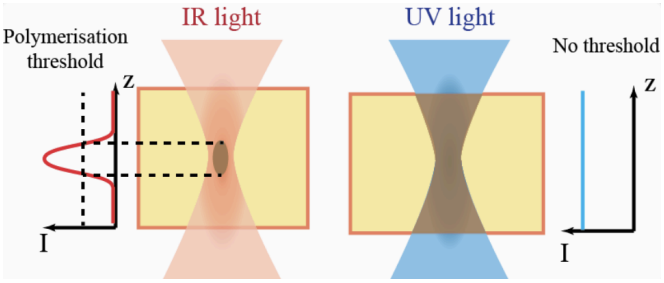

(b)

Fig. 2.4: Two photon absorption: (a) energy level diagram of the TPA photo-polymerization starting from two-photon excitation of the photo-initiator. In the level diagram and in the chain process above is represented the whole polymerization process ,[2] (b) one photon absorption and TPA voxel polymerization comparison.

the two-photon absorption cross section δ dependencies:

$$\delta = \frac{8\pi^2 h\nu^2}{c^2 n^2 N} I^2 \mathrm{Im}\left[\chi^{(3)}\right] \tag{2.1}$$

where $h\nu$ is the photon energy, N the number density of the absorbing molecules, n the refractive index and $\chi^{(3)}$ the third order susceptibility. Since the two-photon absorption cross section for many material is very small, it is common to employ ultrafast (hundreds of femtosecond) lasers with a high instantaneous pulse intensity, favorable for TPA, but, because the pulses are five to six orders of magnitude shorter than the repetition period (usually tens of MHz that corresponds in time to a period of hundreds of ns) of the laser, the average power is low.

2.1.2 Electron Beam Lithography

Electron Beam Lithography (EBL) consents to realize extremely fine patterns (up to $\backsim$ 5 nm [24]). Derived from the early scanning electron microscopes, the technique in brief consists of scanning a beam of electrons across a surface covered with a electron sensitive resist film, thus depositing energy in the desired pattern.
The main attributes of the technology are the very high resolution, the flexibility of working with a variety of materials, not high fabrication speeds being one or more orders of magnitude slower than optical lithography and the high costs.
The basic idea behind EBL is identical to any other lithographies. The substrate is coated with a thin layer of resist, which is chemically changed under exposure to the electron beam, so that the exposed (non-exposed) areas can be dissolved in specific solvents (positive (negative) lithography). The fundamental condition, that the EBL substrate should satisfy, is to be conductive to not accumulate the incident electric charges that can then deflect the electron beam. The most widely used substrate is silicon with a thin insulating layer of silicon dioxide on top. Other possible substrates that can be used are glass plates coated with metal (ITO [25], chrome on glass, widely used in mask production [26]), in which case the metal layer should be grounded before drawing.
One of the first materials developed for e-beam lithography was polymethyl methacrilate (PMMA) [27]. It is the standard positive e-beam resist and remains one of the highest resolution available resist. PMMA is spun on the substrate and baked at $170 - 200$℃. Electron beam exposure breaks the polymer into fragments that can be dissolved in a mixture of isopropanol and methyl isobutyl ketone, MIBK, (3:1, because MIBK alone is able to dissolve also unexposed resist). Both the exposed and the unexposed PMMA

[2] Valence electrons of an initiator are excited from the ground S_0 to the first excited S_1 singlet state by simultaneously absorbing two photons. The excited electrons then relax by transition to the triplet state T_1 via inter-system crossing, where the initiator is liable to undergo bond cleavages, producing radicals for photopolymerization. The excited states can also be relaxed by radiative processes: fluorescence emission from singlet states F or phosphorescence emission from triplet states P. Both the triplet state and photo produced radicals can be deactivated DE, for example by monomer quenching MQ for the former, and by radical quenching RQ for the latter. Efficient photopolymerization generally needs these competing processes F, P, DE minimized but there are a few cases, for instance RQ, which find use for it in reducing voxel sizes. The dashed line denotes a virtual energy level for TPA photopolymerization quenching by oxygen molecules under two mechanisms: triplet state quenching (T-quenching) and radical quenching (R-quenching). The latter is the major factor that works in the sub-diffraction-limit fabrication.

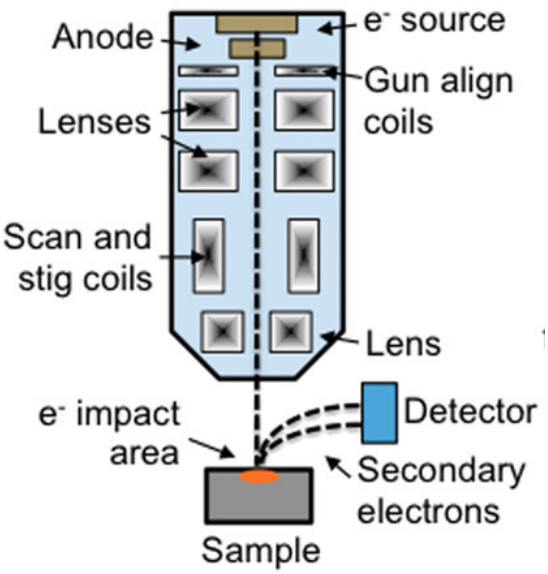

Fig. 2.5: EBL scheme.

can be dissolved in pyrrolidone or acetone. Normally, the direct write systems use a finely focused Gaussian round beam that moves respect to the wafer to expose one pixel at a time. Basically, as shown in Fig. 2.5, a direct writing system consists of a source of electrons, a focusing optics set, a blanker to turn the beam on and off, a deflection system for moving the beam, and a stage for holding the substrate. The field of EBL applications is also varied. It was originally developed for manufacturing integrated circuits and is also used for creating nanotechnology architectures. Moreover the fabrication at the nanoscale level on metallic substrates or dielectric ones allow the realization not only of integrated photonic circuit but also of plasmonic [28, 29] and metamaterials [30–32] based devices. Among the photonic structures that can be fabricated with the e-beam lithography, photonic crystal slabs [33, 34] are well-known platform that deserved to be mentioned. These ones are only few examples of the various devices that can be realized.

2.2 Materials

As the glass optical fibers are nowadays used for high-speed, long distance data transfer, on the micro-scale polymeric photonic circuits can be realized on small chips surging economic criteria and technical requirements. The choice of polymers has been driven by many different reasons but the key point of this study is the opportunity to chemically modify their molecular structure to achieve the desired chemical and physical behavior. The chemical knowledge inside the group allowed to design and combine the molecules in order to match the physical requirements of the fabrication setup, like the operational wavelength, and at the same time the mechanical properties for the photonic structures.

One of the relevant advantages is that polymers are cheap materials especially compared with the silicon technology but also less fragile than glass fibers. Moreover they can be integrated on different substrates and diversified materials [35] to combine more functionalities. They can be easily manipulated by several conventional techniques as dry and wet etching[36, 37], embossing [38] and soft lithography [39] creating a low-cost reliable platform. Many of the samples studied in this work have been realized with a direct laser writing technique but it will be shown how it is possible to combine structure realized with this method with other photonic devices fabricated by electron beam lithography.
The different techniques require different resists. For e-beam lithography and photolithography, positive resist should be employed. In this case, the polymeric part that is exposed to UV light (with the employ of masks) or to the electron beam, is the region that should be removed. In fact, the exposure changes the chemical structure of the resist so that it becomes more soluble in the developer. The sample is therefore put in the solvent bath, leaving the final sample. Regarding the negative resist, instead, the process is the opposite. Starting from an unpolymerized mixture (monomeric mixture in the liquid state), using for example the direct laser writing technique, light starts the polymerization process and the exposed part becomes solid and not more soluble in the developer. The solvent in then used to remove the unpolymerized mixture.
The employed polymers can be divided into two main categories: rigid and soft ones. The first ones are used to create static photonic structures as waveguides, whispering gallery mode resonators and photonic crystal with different dimensionality. On the other side, the soft and elastic ones are the main character materials of this work as reconfigurable matter, polymeric matrix for tunable photonic structures. The possibility to modify the geometrical and physical properties of photonic devices, through an active external stimulus, motivates this research line in order to achieve the demonstration of an optically tunable photonic structure. In particular we are interested in the possibility to convert the light energy into a mechanical deformation, controlling the three-dimensional movement through the molecular alignment and triggering it with the light irradiation.

2.2.1 Commercial acrylate-based polymers

For the fabrication of rigid photonic structures, commercial monomers have been used. The choice fell on the product sold by the company that fabricated the lithographic system (Nanoscribe GmbH). This resit has already been optimized in terms of resolution, rigidity and swelling. In particular, we address Ip-Dip (Figure 2.6.a), a negative liquid photoresist for upside down fabrication. This particular configuration is permitted by this resist behavior both as a photo-sensitive polymerizable medium and as an immersion oil for the high numerical aperture objective. Due to its refractive index matched to the focusing optics, IP-Dip guarantees ideal focusing and hence highest resolution for this unique lithographic configuration. It does not require any pre-bake or post-bake process, it can be developed with a first 10 minutes bath PGMEA (Propylene glycol methyl ether acetate) and a second one in isopropanol. The refractive index at 1500 nm before light exposure is 1.52 and it increases of 2% after polymerization. For enhancing the refractive index contrast with the glass substrates, low refractive index material as silica substrate ($n = 1.455$ @ 1500 nm) are used. The lithographic features are high lateral resolution,

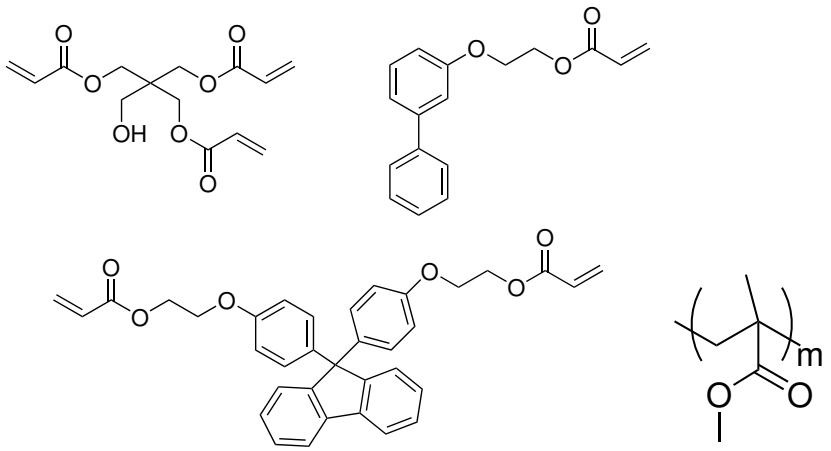

(a) (b)

Fig. 2.6: Chemical formulation: (a) Ip-Dip resist for Direct Laser writing lithography (Dip-in Lithography), (b) PMMA employed for e-beam lithography.

150 nm, high stability and rigidity, low proximity effect and shrinkage. It is defined as percent size variation of the upper layer of the fabricated micro-structures due to the reduced glass strain - that the structure upper layers resent - and the developer outflow after the structure drying [40]. The amount of the developer (and monomers while the structure is still inside the monomer drop) that can penetrate inside the structure depends on the crosslinking degree of the polymeric network. It is then determined by the laser power. If a traditional writing configuration, bottom-up polymerization, the laser beam light is partially diffracted by the already polymerized structures and optical aberrations decrease the effective power employed for the polymerization of the upper levels of the structures. To solve this drawback, a power compensation can be actuated or a reverse configuration can be used (DiLL configuration for this specific lithographic system). For simplicity and broader application, the second approach has been chosen in this study.

The other acrylate based polymer employed in the realization of dielectric resonators is the PMMA (Polymethyl methacrylate, Figure 2.6.b). It has good optical properties as transparency in the visible and infrared region and good rigidity (more elastic that Ip-Dip with a lower Young modulus of $2 - 3$ GPa). As in our case, it is employed as a common high resolution positive resist for electron beam lithography. In fact, polymeric chains are broken by the electron shower and through a developer, the exposed part is removed. Its employ with e-beam lithography is well established and it represents far and away the most popular e-beam resist, offering extremely high-resolution, ease of handling, excellent film characteristics, and wide process latitude. Its refractive index is commonly 1.48 but since it is usually suspended on silicon substrates, the refractive index contrast with the surrounding air is enough to confine the electric field with a suitable engineering of the photonic structures.

2.2.2 Liquid Crystal Elastomers

Liquid crystals (LCs) have been recognized as a state of matter that characterize the technological application of the last century. After the dominant diffusion in the display technology, today their application reaches the bio-medical field [41], the photonic devices [42, 43] and the robotic research [44]. However, the use of liquid crystals in many applications also deserves some drawbacks. The most evident one is that their fluid consistence, which requires proper encapsulation schemes in order to confine the LC close to the active region – for instance, the pixel element of a screen. They are characterized by a self-organization in phases with a typical long-range order at molecular level (that reminds the crystalline nature) and a liquid phase. The most studied mesophases are the nematic and chiral one (one dimensional order) or smettic variants (two dimension order). If the liquid crystalline molecules are combined with cross-linking units, a polymeric material that exhibits the properties of liquid crystals is formed. These materials merge the essential properties of an ordinary liquid crystal, like optical birefringence, responsivity to different external stimuli, with a unique shape morphing behavior. Different classes of liquid crystalline polymers can be prepared depending on the positional order of the mesogenic unit: main chain or side chain. Moreover chemical compositions, crosslinking densities and thermo-dynamical properties create a division in between liquid crystal polymers (LCPs), liquid crystalline polymeric networks (LCNs) or liquid crystal elastomers (LCEs) [45]. The first ones are rigid linear polymers (without cross-linking molecules in their composition) with liquid crystalline phases and a very high Young modulus above 100 GPa; LCNs have a glass transition temperature in the interval $40 - 100\,^{\circ}\mathrm{C}$ and a Young modulus of around 1 GPa; LCEs are a subclass of the LCNs and are characterized by lower than room temperature glass transition and a low degree of crosslinking that brings the Young modulus down to MPa. Whereas LPCs show no change in the order parameter, LCEs and LCNs exhibit a quite large reshaping under an appropriate stimulus. This elastic macroscopic deformation is connected to the transition from two different phases and is their remarkable property. Analyzing the properties of the materials we used, we underlined their LCN nature but associated with good elasticity and a relatively low glass transition temperature.
After the first examples of liquid crystalline elastomers (LCE), prepared by Finkelmann by grafting mesogenic cores on a polisiloxanes chains [46], several synthetic strategies have been developed. Acrylate based free radical polymerization is one of the more studied: even if it conducts to glassy material with higher elastic modulus, this reaction allows to integrate complex alignment inside the polymeric matrix or to pattern the material by photolithographic technique [47]. Moreover, acrylate based photopolymers have several properties which make them attractive for multi-photon polymerization applications: a wide variety of the full composites or their monomers are commercially available; they are transparent at visible and near-infra-red wavelengths, and can be therefore be processed by near infrared (NIR) and visible (VIS) ultra-fast lasers; they can be developed in common, non-aggressive solvents such as isopropanol; they can be polymerized rapidly (that enables the use of fast scanning velocity and the TPA) and with low shrinkage; and, after polymerization they are mechanically and chemically stable.
The first aspect that is important to control, is the polymer deformation that opens

to bending, twisting or more complex movements. The second one allows the use of LCN for microscale patterning by masks [48], molds [49] or more complexes technique such as Direct Laser Writing [50], that has been introduced in 2.1.1. In this thesis, side-chain polymer configuration has been chosen and after the liquid crystal monomer orientation the cross-linking procedure and acrylate polymerization has been reached during a photo-polymerization process.

2.2.3 Our Liquid Crystalline Network

Liquid crystalline networks (LCNs) retain the initial monomer alignment and are able to elastically deform in corrispondence of the liquid crystalline to isotropic phase transition [46, 51, 52]. The crosslinked structure allows the recovery of the initial shape after removing of the external stimulus while, the type of shape-change is determined by the initial alignment inside the polymer [53], that could be engineered by all the possible alignment techniques for low molecular mass LC. In the case of nematic LCN, where in the equilibrium state the molecules have an orientation order along one axis, called director, the transition to the isotropic case forces a contraction along the director and an expansion in the perpendicular plane. The order parameter, used in LC to define the orientation order of LC, is defined as

$$S = \langle \frac{3\cos^2\theta - 1}{2} \rangle$$

where θ is the angle between the liquid crystal molecular axis and the director. During the nematic to isotropic phase transition, S passes from $S = 1$ to $S = 0$ in the isotropic sample. This is the effect that will be widely exploited inside this work. Moreover in our case, the LCE mixture will be applied to the realization of microstructures with the lithographic technique of DLW; such proof can be found in a recent work [50].
The preparation of our LCE mixture requires three components: a mesogen, responsible of the material alignment; a crosslinker, which allows the formation of a network with an elastic mechanic response; and a photo-initiator, to achieve the spatial control of the radical reaction. The first two components need to be functionalized with one or two photo-polymerizable groups, such as the acrylate group. In order to obtain a photo-responsive material, a dye, an azobenzene molecule, is added in the monomeric formulation. Commonly azo-dyes in polymeric matrices are usually responsible for the optical transition from the nematic to the isotropic phase thanks to the *trans-cis* isomerisation [54–56]. This isomerisation describes the transition from the azo *trans* state (elongated molecule, fundamental state) to the *cis* state (bent excited state). In our material the typical light activation transition contributes only marginally to the network deformation. In fact we can not define it as a pure optical effect but as a light induced thermal phase transition. The role attributed to the photo-responsive azo-dye is the enhancement of the local temperature of the LCE structures when it undergoes fast *trans-cis* isomerization via the absorption of resonant photons
Molecules employed in this study are depicted in Figure 2.7. M1 and CL1 were purchased from Synthon Chemical (SYNTHON Chemicals GmbH & Co. KG,Wolfen, Germany), Irgacure 369 was purchased from Sigma Aldrich (Sigma Aldrich SRL, Milano,Italy), and D1 was prepared in our labs to match the technical requirement of the operational

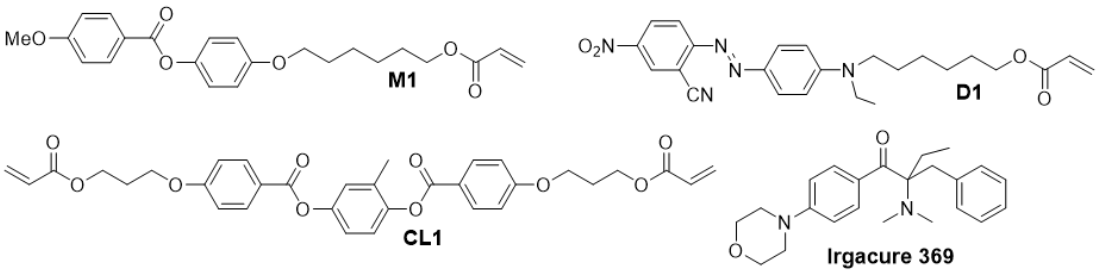

Fig. 2.7: Monomer structure.

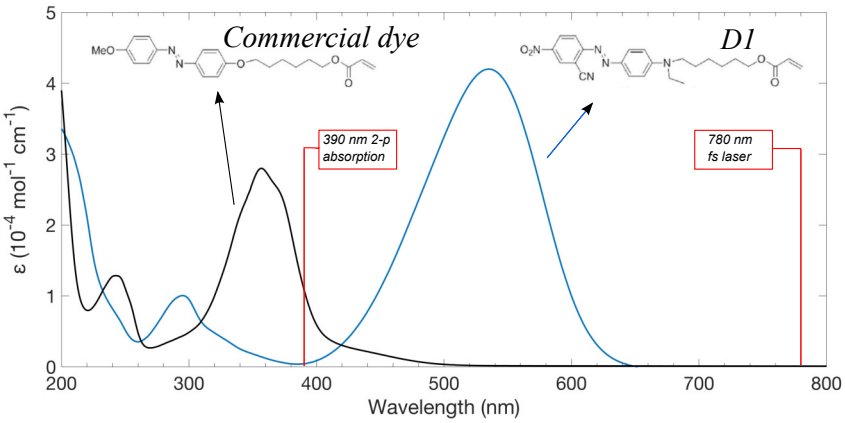

Fig. 2.8: Absorption spectra of the azo-dye before and after the chemical modification of the substituents on the aromatic rings.

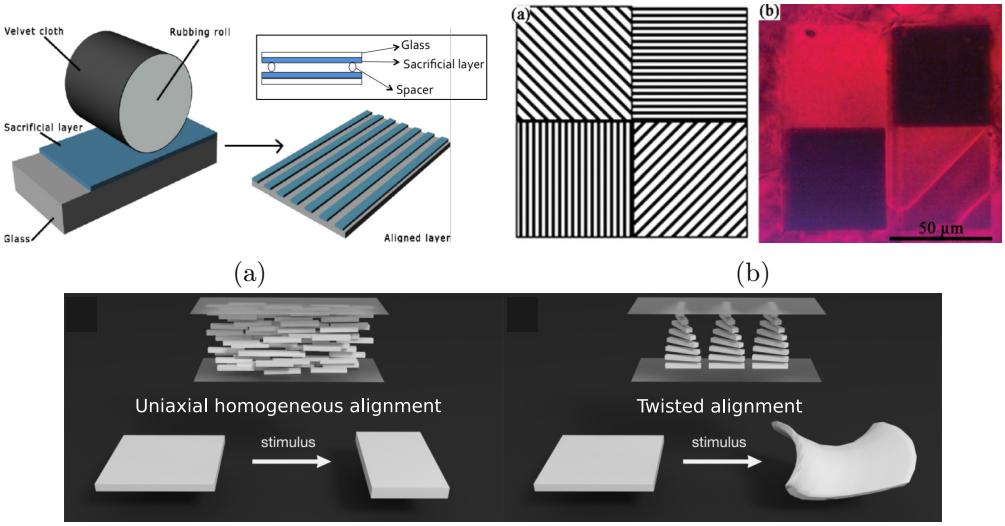

Fig. 2.9: (a) Rubbing technique for LCE alignment (b) Micro-patterning made with DLW: on the left, four kinds of micro-grating patterns designed for LCE laser writing, on the right, POM image of the monomer mixture alignment induced by the micro-grating. (c) Different alignment configurations: the uniaxial one on the left and the twisted one on the right. The respective deformations in response to an external stimulus are reported.

wavelength of the lithographic technique. In fact, many commercial azo-dyes have an absorption band in the UV spectral region (Commercial Dye, in Figure 2.8) but they are not suitable for direct laser writing fabrication, as this overlaps with the photoinitiator two-photon absorption peak used in the system. To circumvent this, the azo-dye absorption has been tuned by changing the substituents on the aromatic rings, thus opening a gap of minimum absorption around 390 nm and a transparency window above 700 nm (Figure 2.8).

To control the cross-linking degree of different mixtures, the relative percentage of mesogen and cross-linker are varied. The minimum amount of cross linker that leads to the fabrication of a solid micro-structure with a defined shape is the 10%. We will consider how increasing this quantity, the resolution would change and the deformation would be reduced.

The LC molecular orientation can be controlled inside the liquid crystal cells creating alignment patterns in two different way: an uniform cell alignment and a local micron-squared size pattern. The first one exploits a polymeric sacrificial layer (polyimide) spin-coated on a cleaned glass and subsequently rubbed (or not) with a velvet tissue. For the homogeneus uniaxial alignment (PI 130 Nissan Chemical), creating a groove pattern along one direction, the molecules tend to align along this axis that becomes the LC director. Using polymeric coatings, not only homogeneous uniaxial alignment is achievable (two rubbed glasses with parallel groove orientation, see Fig. 2.9.a). In fact,

homeotropic alignment provides a molecule orientation perpendicular to the glass using a polyimide layer (PI 1211 Nissan Chemical) with no rubbing. Bent-splayed alignment combines one glass for the homeotropic and the homogeneous cell in such a way to generate a bending of the resulting structure. The twisting of nematic liquid crystals is instead guaranteed in a cell made from two uniaxial rubbed glasses with a perpendicular disposition of the groove direction (Figure 2.9.c). But, if a more precise control over the alignment is required on the microscale, the previously described techniques can not be applied anymore. To engineer different movements on the same micro-structure, that means for example a contraction of one part of the micro-device and a bending of the remanent one, micro-pattern can be realized on the cell walls by DLW [57] as showed in Figure 2.9.b. Local control over the molecular orientation is then achieved on molecular level by imprinting micro-grating patterns, with an arbitrary form that can be from 1 to 100 μm in size, on the inside walls of a glass cell and then subsequently infiltrating with the elastomeric mixture. The liquid crystalline monomers were first oriented by the micro-gratings and thus the elastomeric structures can be patterned with the designed molecular order. The resulting micro-structures can be given complex shapes and a much broader scale of functionalities than is possible with existing techniques. A scheme of two of the most diffuse alignments is shown in Figure 2.9.c. The monomer infiltration inside the cell, already prepared with the alignment treated glasses separated by spherical spacers (from 5 μm up to 270 μm), is carried out at 75 ℃ in LC mixture isotropic state. Cooling slowly down the cell at room temperature into the nematic phase, the LC mixture organizes the desired alignment following an epitaxial growth on the coating surface. Type and quality of the reached alignment are evaluated by a polarized optical microscope (POM) observation measuring the sample transmittance as function of the rotating angle. This characterization is based on the optical anisotropic LC texture observation between two crossed polarizers and gives information about the molecular arrangement within the medium. The texture depends on the structural defects of the LC phase and it provides also a valuable diagnostic tool for the mesophase identification [58] and the alignment quality.
Once infiltrated the glass cell and checked the LC alignment, the monomer mixture is polymerized by an UV lamp to create macroscopic films or by two-photon absorption polymerization to fabricate micro-structures. The polymerization process in both cases is a free radical polymerization process triggered by the photo-initiator. After the elastic structure realization, the shape and refractive index control can be led by light.
Combining the employ of photo-responsive elastic materials, applications not only in the photonic field were demonstrated. 3D LCE structures with nanoscale feature size led to the first demonstration of a walking micro-robot [59]. By irradiation of non-structured light, this structure is able to walk on different surfaces with a spatial and temporal control on the structure deformations. Another example of light-driven micro-robot is reported for a micro-fish swimming in viscous glycerol-water solution [60].
Depending on the photonic structure that should be addressed, different properties of the liquid crystalline elastomeric mixture are required. The property tuning is achieved both on the chemical point of view, modifying the molecular chemical structure or the mixture elements percent weight, and on the physical side, acting on the lithographic parameters to control the polymerization process. As function of these parameters, physical and chemical properties of the LCE mixture have been studied. The refractive

Mixture	M1[2]	CL1[2]	IN1[2]	Irgacure 369[2]	T_{CrI}(℃) [3]	T_{NI}(℃)[4]
MM-10	88%	10%	1%	1%	55	50
MM-20	78%	20%	1%	1%	53	57
MM-30	68%	30%	1%	1%	46	64
MM-40	58%	40%	1%	1%	46	71

Table 2.1: Composition and mesomorphic properties of monomeric mixtures.

index, physical quantity of fundamental importance for the photonic properties, has been measured with a refractometer method. The time responses of the different mixtures have been characterized: a comparison in the response time scale of micro and macro structures is reported. Moreover, a more technical analysis on the writing parameters for the different mixtures has been done to identify the best mixture for each application.

LCE dynamical behavior: an effect of the crosslinking degree

In this section, the attention is focused on the mechanical properties and on the light irradiation response of different LCNs prepared by adjusting the ratio between the mesogenic acrylate M1 and the mesogenic diacrylate CL1. Before focusing the attention on the experimental results, some physical quantities have to be introduced for LCE monomeric mixtures and polymerized LCE films.
A thermotropic phase is defined as enantiotropic or monotropic referring to its thermal stability with respect to the crystalline phase. An enatiotropic phase is thermodynamically stable and forms by heating the crystalline material above a certain temperature and by cooling the isotropic liquid [45]. A monotropic phase, instead, is a metastable phase that occurs only by cooling the isotropic liquid below the characteristic transition temperature and is due to hysteresis in the crystallization process. For monomeric mixtures the relevant transition temperatures are the T_{CrI} and the T_{NI}. The first one is the transition temperature in between the molecule crystalline state and the isotropic one recorded in the heating process while the second one is the point when the monomeric mixtures organize from the isotropic state to a mesophase on cooling. Our liquid crystalline mixture, is a monotropic one so that on heating we have only the transition from the crystalline form to the isotropic one while on cooling a wide range of temperatures sustains the nematic phase. When we are talking about polymers, these two quantities can not be defined anymore or acquire a different meaning. In fact, the characteristic properties for films and microstructures too, are the glass temperature, T_g, that corresponds to the glass transition when the material becomes from an hard and "glassy" state, more viscous or rubbery (as in the case of elastomers) and the nematic-isotropic phase transition temperature, T_{NI}, that rules the deformation point of LCEs [61].
The employed molecules are the ones described in the Paragraph 2.2.3; here we evaluate the physical and chemical effect of the different percentage of M1 and CL1. We demonstrate how the balance in between the two molecules impacts strongly the mechanical behavior and how this is reflected in the microscopic sample response. The

[2] %mol/(molon the total mixture).

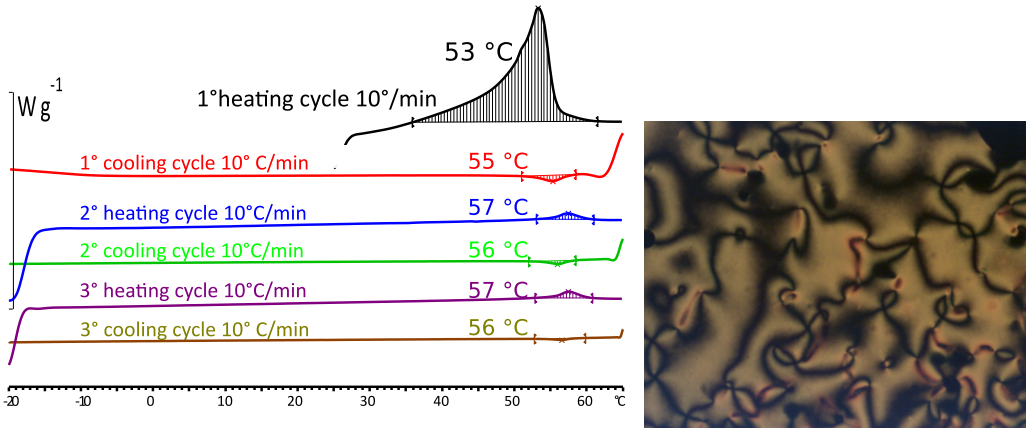

(a) (b)

Fig. 2.10: (a) DSC graphics for the monomeric LCE formulation and (b) a POM image of MM-20 at 50°C. This type of mesophase is uniquely assigned thanks to the typical nematic schlieren textures with 2-brush and 4-brush defects [62].

different monomeric mixtures are listed in Table 2.1 and noted as MM-x where x is the percentage of the crosslinker CL1. All mixtures contain 1% mol of the azo-dye and 1% of Irgacure 369 according to previous studies [50]. Mixture mesomorphic properties have been investigated by Differential Scanning Calorimetry (DSC) [5] and Polarized Optical Microscopy (POM) .[6] With both techniques, in the heating scan, they melt directly in the isotropic phase between 50 °C and 70 °C, depending on the crosslinker percentage, while on cooling, they show an exothermic transition attributed to the appearance of a monotropic nematic phase that persists in a very broad range of temperature. The mixtures keep the nematic phase also at room temperature, as we could observe in the DCS traces reported in Figure 2.10.a. Such behavior has been demonstrated fundamental for the use of the mixtures as photoresist in the DLW micro-structuring as shown in the next two paragraphs. Our analysis considers splayed films prepared infiltrating, for capillarity, the melt mixture inside the polymerization cell, previously spin coated with polyimide coating and rubbed in such a way to guarantee splayed alignment. DSC film analysis showed a linear increase of the T_g with the crosslinker percentage but no other clear information could be deduced (see Figure 2.10.a). Moreover, POM observation,

[3]Determined from the peak maximum in the first heating scan of DSC trace.
[4]Determined from the peak maximum in the first cooling scan of DSC trace.
[5]The differential scanning calorimetry (DSC) is a technique used to investigate the response of polymers to heating. DSC can be used to study the melting of a crystalline polymer or the glass transition. It is composed of a computer and a measurement chamber: the sample under investigation and a reference one are contained in two different measurement chambers. The computer is used to monitor the temperature and regulate the rate (a typical heating rate is around 10°C/min) at which the temperature of the pans changes. The difference on the rate of temperature change for the two samples depends on the composition of the pan contents as well as physical changes such as phase changes. Differential scanning calorimetry was carried out using a Mettler-Toledo DSC 821 apparatus.
[6]Polarized optical microscopy was performed using the inverted microscope Zeiss, Axio Observer A1 with cross polarizers.

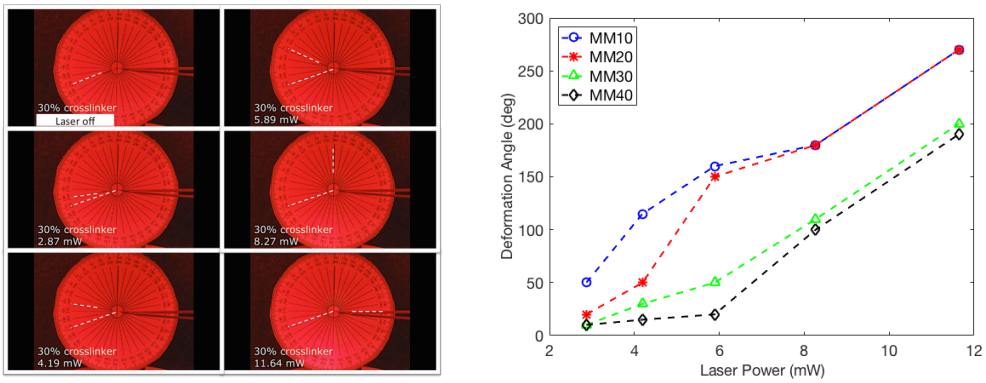

(a) (b)

Fig. 2.11: Response of splayed films to laser irradiation: (a) photos of splayed MM-30 during irradiation, (b) laser power dependence of the bending angle for the different mixtures.

reported in Figure 2.10.b for film MM-20 on heating, highlighted the birefringence of the polymers above 150℃. Also in previous studies on such type of LCNs, T_{NI} could not be clearly detectable and estimated around 200℃ even if a paranematic state persist even at higher temperatures [63, 64].
Irradiation with selective wavelength is able to induce deformations in azobenzene containing LCN according to the dye characteristics: its absorption spectrum selects the wavelength required to the actuation. Moreover, the phase transition mechanism can be different depending on the aromatic ring substituents that affect mainly the lifetime of the *cis* azobenzene and its percentage at the photo-stationary state [65]. In our cases, D1 acts mainly as nanoscale heater able to induce the nematic to isotropic phase transition after absorption of light in the visible region but quite high laser power are required to induce observable deformations. Above a certain power of irradiation, the photo-thermal effect is predominant and it is able to deform the polymers. Studies on such effect are conducted on splayed LCE film irradiated from the top with a green laser. Such films are able to display controlled bending deformation as function of temperature: in these systems, the difference of the thermal expansion coefficient on the two faces, due to the bigger thermal expansion in the perpendicular direction in respect to the alignment one, results in film bending. In general, the film bending is also due to the finite absorption depth but in this case, due to the excitation light direction, that is lateral to the stripe (see Fig. 2.11.a where the laser light beam is perpendicular to the image), we can assume that the only contribute to the deformation is due to the molecular alignment. The bending angle is function of the film temperature [66]. In Figure 2.11, we reported the relationship between the laser power and the induced bending angle: in Figure 2.11.a the photos obtained for the splayed MM30 sample during irradiation at increasing laser power are depicted, and the relationship between the laser power and the induced bending angle is reported in Figure 2.11.b. Even if the power threshold to obtain a bending was found rather similar in all samples (around 2.87 mW), the bending angle resulted very different, with bigger angles for less cross-linked films, especially at lower irradiation power (for example: 160° for MM-10 and 20° MM-40 by

Mixt.	**2.87** mW		**4.19** mW		**5.89** mW		**8.27** mW	
	$\mathbf{t_{bend}}$ $[\overline{v}_{bend}]$	$\mathbf{t_{relax}}$ $[\overline{v}_{relax}]$	$\mathbf{t_{bend}}$ $[\overline{v}_{bend}]$	$\mathbf{t_{relax}}$ $[\overline{v}_{relax}]$	$\mathbf{t_{bend}}$ $[\overline{v}_{bend}]$	$\mathbf{t_{relax}}$ $[\overline{v}_{relax}]$	$\mathbf{t_{bend}}$ $[\overline{v}_{bend}]$	$\mathbf{t_{relax}}$ $[\overline{v}_{relax}]$
MM-10	2.5 s [20]	1.8 s [28]	2.9 s [40]	2.2 s [52]	1.9 s [84]	1.9 s [84]	2.2 s [82]	2.2 s [82]
MM-20	4.5 s [4]	1.5 s [13]	2.3 s [22]	0.9 s [55]	1.5 s [100]	1.0 s [150]	0.5 s [360]	0.9 s [200]
MM-30	1.7 s [6]	0.6 s [17]	2.0 s [15]	0.8 s [38]	1.4 s [36]	1.1 s [15]	0.7 s [157]	1.3 s [85]
MM-40	1.2 s [8]	0.9 s [11]	1.3 s [12]	1.3 s [12]	1.0 s [20]	1.0 s [20]	0.9 s [111]	1.3 s [77]

Table 2.2: Bending and relaxation times, and related average angular speeds $\overline{v}$ expressed in rad/s for the LCN macro-stripes for different excitation powers.

irradiation with 5.89 mW). By increasing the power, the bending angle kept increasing, until the complete folding of the cantilevers on themselves, and without following a linear trend with laser power (Figure 2.11.b). The response time to the light stimulus and the relaxation time are reported in Table 2.2. Increasing the excitation power, the response time was faster due to the higher number of absorbed photons that caused a higher local temperature. On the other hand, it was difficult to retrieve a trend for the relaxation times. It can be noticed that they were independent of the bending angle (and therefore of the laser power) because the relaxation dynamics was due only to the thermal capacitance of the material, while the activation time is strictly connected to the energy density adsorbed by the film. In fact, for all samples, average speed increases together with the laser power. Since the actuation speed was not constant during the bending movement, we reported an average angular speed. For the higher powers (5.89 and 8.27 mW), we observed bending time of less than 1.5 s and relaxation time of about 1.3 s for all the mixtures except for MM-10, that moved slowly due to the lower cross-linking density and high softness. Bending resulted slower increasing the crosslinking percentage for the laser powers analyzed, such as for the relaxation times, probably due the higher rigidity. Comparison of the different mixture response times is not straightforward because of the non-Gaussian laser focal spot and the not exactly reproducible tip mechanical constraints.
For the same reason, and because it would required a laser with bigger spot to cover the whole film surface, studying the contraction of homogeneous films results more difficult and less accurate than investigating the bending of splayed stripes. We observed bending time of less than 1 sec and relaxation time of about 1 sec for all the mixtures except for MM-10, that moves slowly due to the lower cross-linking density. Since the actuation speed is not constant during the bending movement, we report the actuation time and the bending angle instead of the angular speed for the different mixtures. To compare the different response time in the micro-scale of the different mixtures, with the DLW technique, micro-blocks ($100 \times 20 \times 20\ \mu m^3$) have been fabricated. Also in this case, the alignment quality can be verified trough POM observation, as reported in Fig. 2.12.a-b, by checking the transmittance extinction with a sample rotation of

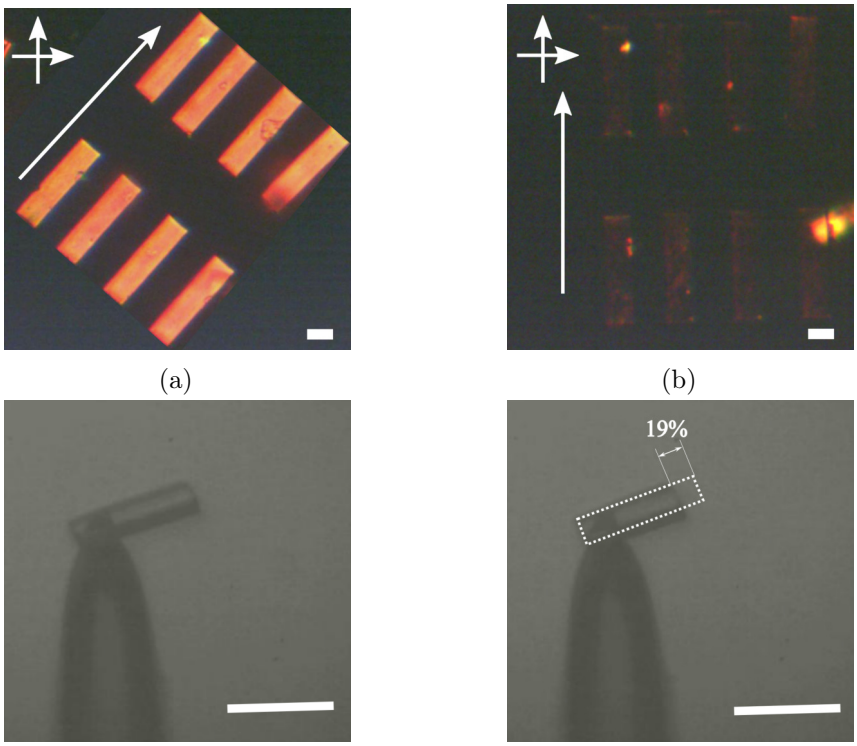

(a) (b)

(c) (d)

Fig. 2.12: POM images of different block parallel (a) and 45° in respect to the polarizer directions (crossed arrows) (b). The scale bar is 20μm and the big arrow indicates the rubbing direction. (c-d) Optical images of the blocks prepared with DLW by MM-10 mixture and suspended on the fiber in the equilibrium position (no green laser excitation) (c) and under a green laser light exposition (d). The scale bar is 80μm.

Mixture	t_{contr}	t_{exp}	Max contraction
MM-10	12 ms	16 ms	19%
MM-20	20 ms	20 ms	16%
MM-30	20 ms	16 ms	17%
MM-40	16 ms	16 ms	10%

Table 2.3: Contraction and expansion times (respectively t_{contr} and t_{exp}) and maximum light induced contraction of LCN blocks realized by DLW.

45°. In such scale and because of the soft nature of the polymer, through structure bending is not possible to achieve an accurate analysis of the material response. Longer cantilever, difficult to detach and manipulate would be required and the bending angles for such small elements are difficult to evaluate. For this reason, we evaluated the contraction of homogeneous samples during the illumination with green laser (Figure 2.12.c-d) reporting percentages of contractions and response times. We then compare the time behavior between macroscopic and microscopic samples. From Table 2.3, we point out that the movement dynamics happens in the timescale of tens of milliseconds. The comparison with the macroscale stripe bending time underlines that we can obtain micro-actuators with a two orders of magnitude faster response time. Increasing the cross-linker percentage in the mixtures brings to a slower dynamics and to a smaller contraction due to the lower degree of freedom and a higher rigidity of the material. We then compare the dynamics timescales for the bending of macrostructures with the expansion/contraction of the micro-elements as indicators of two evolution timescale to the external stimuli in the micro and macro world. We notice that, in the macroscale, the time from the relaxed state to the deformed one (bent stripe) is higher while, in the microscale, the opposite behavior is detected. In fact, the time needed for the contraction is shorter in respect to the one necessary for recovering the non-stimulated state. Moreover, in the microscale, the relaxing time is independent from the cross-linker concentration inside the mixture while we can appreciate a faster contraction dynamics for the less cross-linked structure. Because of the different alignments, thermal diffusion and geometric properties between the structures realized in the two different scales, a complete comparison of movement dynamics cannot be done. For examples, the macro stripes have a larger ratio of the lateral surface over the total volume in respect to the micro-blocks, such as the heat release to the environment is faster respect to the bending time. However similarities and the evolution time dynamics trend can be evaluated depending on the cross linker amount of the polymeric structure.

LCE refractive index dependence from the crosslinking degree

The LC molecule order is reflected in the macroscopic and microscopic optical properties. Considering a nematic alignment, LC monomers are highly birefringent with a higher refractive index along the axis parallel to the LC director (extraordinary refractive index n_e) and a lower one (ordinary refractive index n_o) in the perpendicular plane. This property remains valid under the clearing temperature, T_c, that corresponds to the phase transition from the nematic to the isotropic state (for this nematic liquid crystal network,

the clearing temperature, T_c, corresponds to the liquid crystalline to isotropic phase transition temperature, T_{NI}). Overcoming T_c, the monomers have only one homogeneous refractive index, n_i. As observed for conventional liquid crystal and also for LC side-chain polymers, n_e shows a stronger temperature dependence than n_o [63, 67]. We can explain this behavior from the balance between an increase of n_o, due orientation loss, and a decrease due to the decreasing density with the temperature increase. With respect to n_e, the loss of orientation and the decreasing density work in the same direction, which causes its steep decrease at increasing temperature. The mean refractive index $\overline{n}$ in the nematic phase is given by $\overline{n} = \sqrt{(n_e^2 + 2n_o^2)/3}$. The mean refractive index has a smooth dependence on tempererature and even at the nematic-isotropic transition remains nearly constant. The net consequence is that n_o must decrease two times less than n_e increases. This is due to the fact that order parameter is a traceless tensor [68]. After the polymerization process, both n_o and n_e increase because of the density raise (polymerization shrinkage [51]), and we have to notice that n_e gets even bigger because, in this particular case, the order parameter increases slightly more. By photopolymerization, the molecular orientation is in general preserved, although the degree of order might be somewhat affected by the molecular packing when the monomers are being squeezed during the formation of the polymer chains [69]. Most interestingly, no isotropic phase is formed upon further heating of the polymer to thermal degradation, and the birefringence $\Delta n = n_e - n_o$ is only marginally reduced. This behavior is observed for all LC diacrylates and a phase, called para-nematic phase is reached [70, 71].
A larger temperature dependence is found for systems with larger spacer lengths or lower cross-link densities. Birefringence values are most often found between 0.05 and 0.25 depending on the aromaticity of the monomers and the eventual incorporation of strong dipoles. One can vary the birefringence of the networks by selecting the appropriate polymerization temperature. When polymerized in the ordered state, all polymers were highly birefringent, but increasing the polymerization temperature, n_e decreases and n_o increases creating a lower value of S [67].
To have a more precise characterization of the refractive index of our polymer, that will be later on involved in the fabrication of polymeric photonic structures, we proceed with a direct measurement of the refractive index as function of the temperature for all the mixtures described in Table 2.1.
Several experimental techniques have been developed to describe the temperature dependence of refractive indexes of LCs. Balzarini studied the temperature dependence of birefringence in the LC methoxy benzylidene-n-butylaniline by measuring the birefringence of a thin sample placed between crossed polarizers [72]. Jun Li and S. T. Wu developed extended Cauchy equations for describing the wavelength and temperature-dependent refractive indexes of liquid crystal compounds and mixtures. The model fits well with thee experimental results of 5CB crystal [73]. Jun Li and his collaborators analyzed the physical origins of the temperature gradient of the ordinary refractive index $\partial n_o/\partial T$ of two LC mixtures (UCF-1 and UCF-2) and compared their physical properties with commonly used commercial LC compounds (5C B and 6 CB) [74]. Simple methods, such as voltage- or wavelength-dependent phase retardation methods, have been developed for measuring the NIR birefringence of LCs [75]. However, only few methods, e.g., the Talbot–Rayleigh refractometer [76] and wedged cell refractometer are available for measuring the individual extraordinary n_e and ordinary n_o refractive

Mixture	Wedge cell angle
MM-10	–
MM-20	1.63°
MM-30	1.71°
MM-40	2.16°

Table 2.4: Wedge cell angles realized for the different mixtures. No data are reported for mixture MM-10 because in this configuration it is difficult to align.

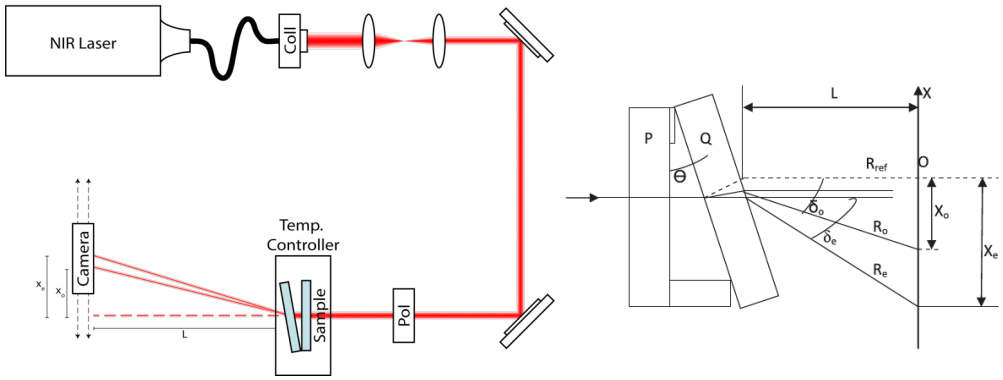

(a) (b)

Fig. 2.13: Experimental setup (a) and geometrical ray representation of the laser beam through the LCE cell (b) (Image from [79]).

indexes in the NIR region [77, 78]. By contrast, in the visible spectral region the LC refractive indexes can be measured quite easily by the commercial Abbe refractometer. Its accuracy is up to the fourth decimal point. However, the usable range of Abbe refractometer is limited to visible and near IR because of the faint refractive light from the main prism and the transparency of the prism.
The refractive indexes of these LCEs were measured by using the wedged cell refractometer method [79, 80]. The cell is composed by two glass substrates, 3 mm thick glass windows, separated by one spacer on one side and glued at both ends. The wedged angle was measured by mounting cell on a rotating goniometer, then a He–Ne laser beam is sent on a substrate of the cell Fig. 2.13.b. The beam is multiple reflected because of multiple reflections at the glass substrates. These reflected beams are visualized on a screen. The position of the first spot is marked on the screen, then the cell is rotated until the second reflected spot is conform on the position previously marked. The rotation of the goniometer is the wedge cell angle. Table 2.4 shows the angle value of five samples. The wedge cell does not allow to obtain a homogeneous uniaxial alignment for the MM-10 mixture because of the minor concentration of CL5, that for its liquid crystalline nature acts both as a crosslinker and a liquid crystal molecule. The experimental setup used for measuring the refractive indexes of LCEs is shown in Fig. 2.13.a. The laser source used is a semiconductor laser operating at a wavelength of 1550 nm and is designed to be coupled to an optical fiber. A beam collimator has been connected to the output

side of the fiber. The laser light is linearly polarized. A beam condenser, formed by two lenses placed in a confocal configuration, allows to obtain a quite narrow laser spot (approximately 1 mm beam diameter) of an excellent Gaussian shape. To control the polarization impinging on the wedged cell, a half-wave plate was placed before the sample in the beam path and rotated in such a way to align the light polarization direction to form a 45° with respect to the director axis of the sample. The wedged cell has been placed inside a Mettler Toledo SH82 hot stage that controls the temperature up to 375℃ paying attention to put the first cell plate (i.e. the first encountered by the laser beam) perpendicular to the wave vector of the incident laser radiation. An infrared pyroelectric camera (Spiricon Pyrocam III, model PY-III-C-A), interfaced with a personal computer, was mounted on a double motorized linear long-travel translational stages (Thorlabs). The alignment of the NLC molecules is homogeneous and is obtained by coating the inner surfaces of the windows by PI 130 (polyimide by Nissan Chemical group) and rubbing the surfaces with a soft cloth. After the mixture infiltration, the correctness of the alignment has been checked by means of a polarizing microscope and then it was polymerized under an UV lamp for 30 min at room temperature and left at 80℃ for 10 min to terminate the polymerization process.
This measurement method is based on the light polarization sensitivity to the different refractive indexes. In fact the laser beam, polarized at 45° with respect to the LC director, splits itself in an "ordinary ray" and an "extraordinary ray". Measuring the deviation angle of these rays with respect to the situation where the LCE cell is absent, we retrieve the two refractive indexes of the liquid crystal by means of the refraction laws. The point where ray (2.13.b), emerging from the empty wedge, encounters the observation plane p, perpendicular to laser beam direction, is determined experimentally by translating the detector along the X axis by means of the micrometric translator until the position correspondent to the peak of the spot is reached. After that the LC cell positioning and the two refracted beams R_o and R_e appear (see Fig. 2.13.b). The camera is now translated in order to bring the center of the detector exactly in coincidence with the peak corresponding to the ordinary beam. The displacement X_o from the point O is recorded. With a proper choice of the camera distance from the sample, the ordinary and extraordinary beam are sufficiently separated to be observed as two different spots and at the same time not so much split to not enter in the camera field. From geometrical considerations (see Fig. 2.13.a) we can retrieve the two indexes of refraction following the formulas:

$$\begin{aligned} n_o &= \frac{\sin(\theta + \delta_o)}{sin\theta} \\ n_e &= \frac{\sin(\theta + \delta_e)}{sin\theta} \end{aligned} \tag{2.2}$$

where θ is the angle of the wedge formed by the two glass plates, δ_o and δ_e are the angles formed by the two beams R_o and R_e with respect to the beam R_{ref} emerging from the wedge in absence of the LCE cell. With some simple algebra and elementary geometrical considerations, we can retrieve the two refractive index expressions as

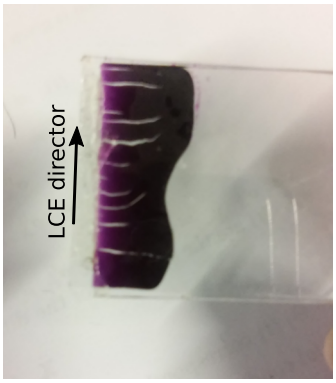

Fig. 2.14: Glass cell infiltrated with LCEs and polymerized. After approaching the transition temperature, the attempts of the film to contract along the director cause the cuts perpendicular to the alignment direction.

function of geometrical parameters that can be measured directly:

$$\begin{aligned} n_o &= \frac{\sin\theta + \tan^{-1}(X_o/L)}{sin\theta} \\ n_e &= \frac{\sin\theta + \tan^{-1}(X_e/L)}{sin\theta} \end{aligned} \tag{2.3}$$

Each measurement has been repeated many times changing the temperature of the sample in order to reconstruct the temperature dependence of the refractive indexes. Every time the temperature was changed, we waited few minutes in order to have a good thermalization of the sample. The temperature range that was explored, starts from room temperature up to the temperature where the sample showed the appearance of damages. Approaching the T_{NI}, the material in between the two cell glasses, would start to contract along the director and expand in the perpendicular plane. For the strain of the glass substrate, it was forced to not move and, trying to contract along the director, reported some cuts perpendicular to the alignment direction as can be observed in Figure 2.14. To evaluate the position of the two beam varying the temperature, the centroid of the two beams has been evaluated by a simple Matlab program starting from the images in Figure 2.15. In Fig. 2.16 we report the measured extraordinary refractive index (open circles), the ordinary refractive index (solid dots) and the average refractive index $\overline{n}$. These measurements allowed us to measure independently the ordinary and extraordinary refractive index of our mixture and evaluate them as function of temperature. As we expected, the LCE polymers do not show a complete transition to the isotropic phase, as can be easily observed in the case of monomers. In fact they reach the so called para-nematic phase where the alignment is partially destroyed but without originating an isotropic distribution of the molecule orientations. This is the reason why the T_{NI} can not be evaluated for these polymers. Observing the refractive index dependence as a function of the cross-linker amount in the mixture we can notice that the refractive index increases with the cross linker percentage. As it can be easily understood the molecular anisotropy as a function of temperature decreases with the percentage of CL. To have a more deep understanding about the molecule influence over the refractive

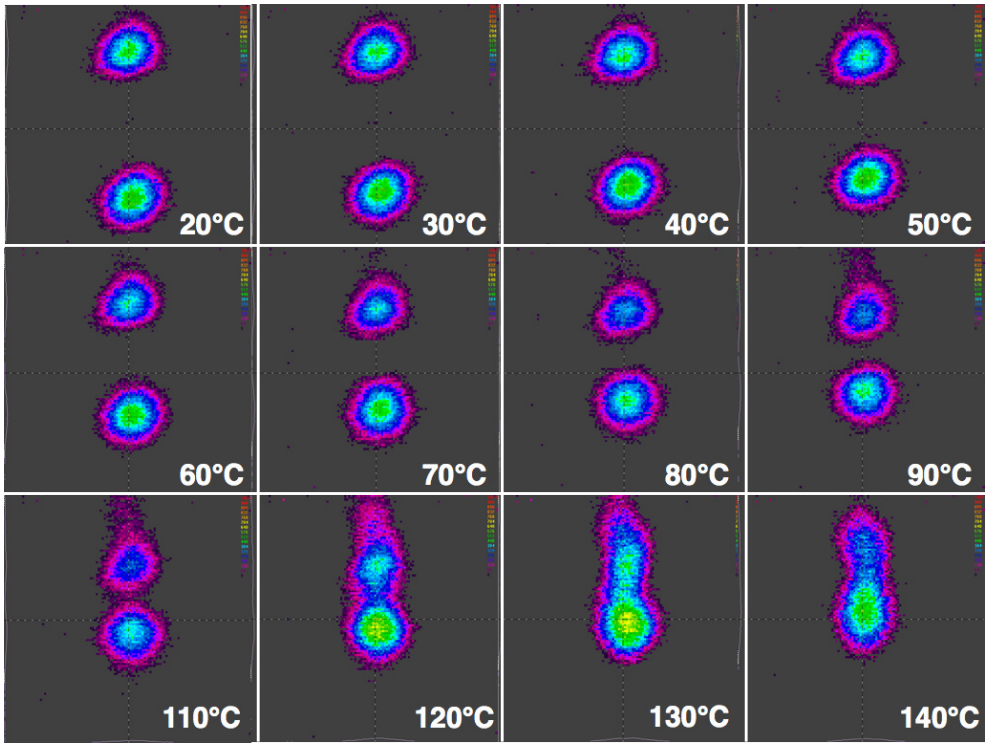

Fig. 2.15: Ordinary and extraordinary beam spot on the NIR camera as function of the temperature.

index behavior, we produced mixtures with a different percentage of dye D1 (up to the 5%) keeping the percentage of cross linker fixed at 30%. From Figure 2.17, it can be noticed that a higher dye percentage brings to an increase of the refractive index and of the anisotropy in function of the temperature, too. Increasing the temperature, the higher number of azo-dye molecules (in the mixture with 5% of dye) impresses a easier network contraction, creating a more 'isotropic' medium than the lower dye concentration mixtures. As a result for D5%, the optical anisotropy is strongly reduced as reported in the graphs in Fig. 2.18.

LCE design for direct laser writing

Regarding the material design for polymer photonics, research efforts have been mainly concentrated on the improvement of the spatial resolution and the obtainment of low-shrinkage structures [40]. Only very recently, the possibility to pattern gradient-index materials has been studied [81]. Currently, a great challenge centers on the realization of responsive materials that can be employed in the realization of tunable devices. LCE nanostructures fabrication issue has been recently tackled by means of the direct laser writing technique [50]. However, the quality of the fabricated nanostructures is not yet comparable with that of nanostructures realized from more conventional materials, and the photonic designer must deal with some compromises until further technological improvements would guarantee a full control over the nanoscale geometry.
To integrate the LCE synthesis with this setup, we need to exploit a photo-activated

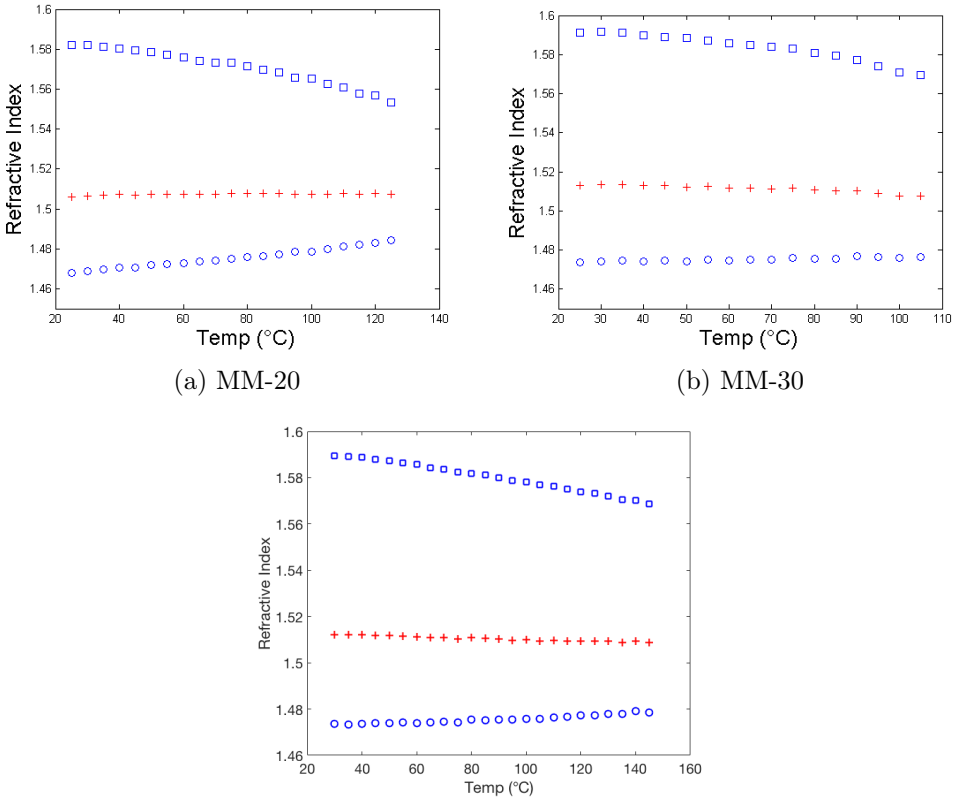

(a) MM-20

(b) MM-30

(c) MM-40

Fig. 2.16: Refractive index temperature dependence for the different mixtures.

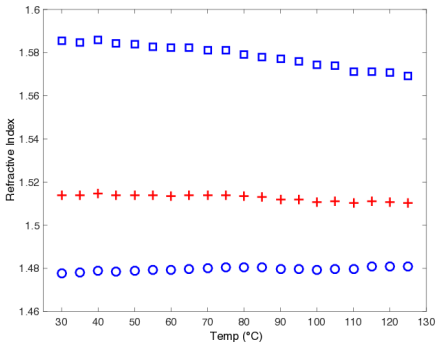

(a) D1: 0%

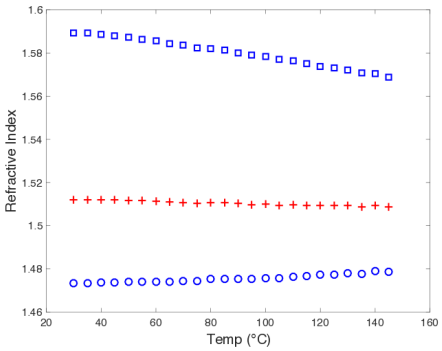

(b) D1: 1%

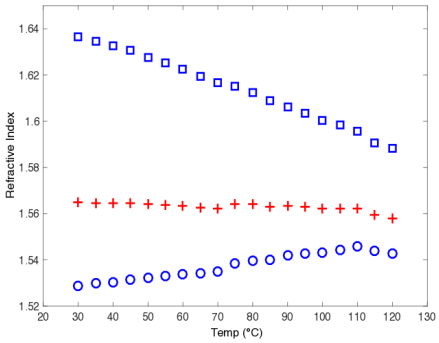

(c) D1: 5%

Fig. 2.17: Refractive index temperature dependence for the different mixtures.

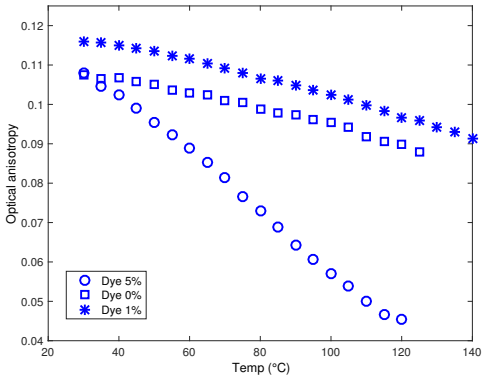

Fig. 2.18: Dependence of the optical anisotropy upon temperature. Different mixtures with different amount of azo-dye are compared.

reaction, such as photo-polymerization of acrylate/metacrylate groups [50] or thiol-yne click chemistry [46]. In this work, polymerization of acrylate-based mesogens was successfully used to create 3D microstructures. The potential applications of the polymer combined with the DLW technique open up the ability to create more complex photonic devices tunable by light. Management of the softness of these elastic materials, in contrast with the rigidity and high resolution often requested, will give access to more complex geometries of photonic devices. This is the reason that motivates this detailed study on the LCE resolution and properties in the micro-scale. We investigate the fabrication of LCE microstructures for different liquid crystalline mixture compositions. For each photoresist, the writing conditions are studied and the possibility to create free-standing structures is demonstrated. At the same time the structure deformation by irradiation with a green laser is always checked to not neglect the contraction percentage, another main key-feature of LCE actuators in photonic devices.
Many parameters are involved in the DLW technique. The repetition rate has been set at 100 MHz, since it has been demonstrated that high repetition rates and short pulses lead to high-resolution structures [82, 83]. The mechanism behind the polymerization process, within this repetition rate range, has to be attributed to a multi-photon activation of the photo-initiator [83]. Moreover, for Irgacure 369, it has been demonstrated that a high repetition rate leads to a higher dynamic range [83]. Once this parameter is fixed, writing speed and laser power play the dominant role in the writing conditions. We evaluate the resolution and rigidity properties as a function of these DLW variables using empirical tests for the different mixtures. In respect to other polymers, the characterization of the voxel dimensions is particularly critical because of the soft nature of the LCEs and the high percentage of swelling of the unpolymerized monomers inside the written structures. To better quantify this effect a further study on the line warping of a suspended line is reported later on. After the writing step, the unpolymerized monomers are removed with a development bath in hot 2-propanol. This choice is motivated by the reduced degree of swelling of this organic solvent in respect to toluene, previously used for the development of this polymer [50], and propylene glycol methyl ether acetate (PGMEA). However, since the monomers are low soluble in 2-propanol, heating above 50° is required to completely dissolve the unpolymerized material without any degradation of the polymerized structures.
The different mixtures that are analyzed are the ones reported in Table 2.1 because varying the molar mass ratio of the monomer (M1) and cross-linker (CL1), we achieve a different crosslinking degree that leads to the control of the structure rigidity. The interesting quantities for the DLW characterization are the polymerization threshold and therefore the dynamic range, defined as the laser power range in between the polymerization threshold and the breakdown threshold, where the too much high power deteriorates the polymerized structures. Moreover we are interested at the voxel dimensions, strictly connected with the resolution properties and to the rigidity of self standing structures.
The polymerization threshold is defined as the lowest power able to create a well-defined polymeric line at the glass-resist interface after the development process [84]. This parameter depends on several effects, such as monomer quenching, oxygen quenching, and the different reactivity of each of the radicals and monomers. To experimentally determine these values, writing tests at the glass-resist interface have been performed

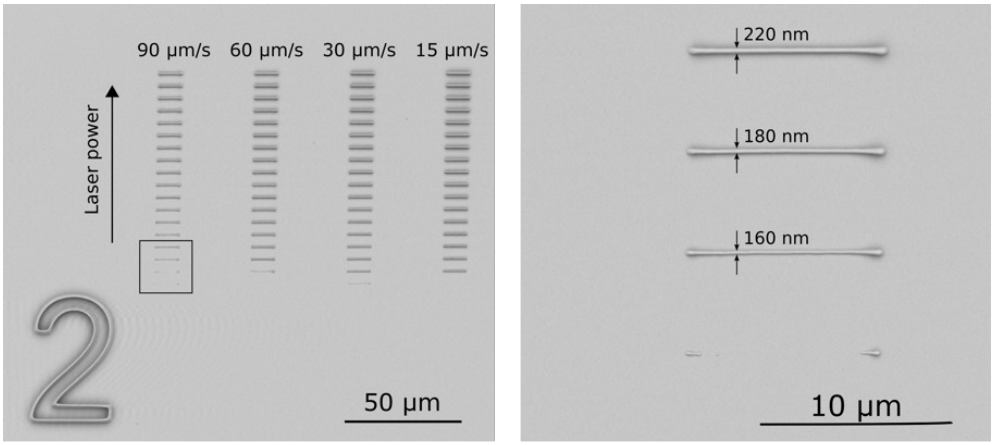

(a) (b)

Fig. 2.19: SEM images of the threshold power tests for MM-20: laser power and writing speed dependence. (a) Laser power is varied from less than 1 mW up to 10 mW, adding 0.44 mW from one segment to the next with each increase in the y-position; (b) detail of the threshold lines, zoom of the square in the (a) image.

Mixture	Polymerization threshold
MM-10	3.52 mW
MM-20	2.2 mW
MM-30	3.52 mW
MM-40	2.64 mW

Table 2.5: Photoresist polymerization thresholds.

while varying the writing speed and the laser power. Figure 2.19.a shows the results for mixture MM-20. Line patterns are written while increasing the laser power value for different writing speeds ranging from 15 up to 90 μ/s. The indicated power values are measured at the objective position. From this calibration, we observed that while varying the writing speed that the polymerization threshold remains the same, with a fluctuation of 1%˘2% around that laser power value. In Figure 2.19.b the effect of the acceleration and deceleration time of the laser pencil beam can be observed. In fact, to reach the constant writing speed, the piezo translation stage needs a certain acceleration/deceleration time. Consequently, the energy deposited at the beginning and at the end of the segment is higher and leads to a partial polymerization. Table 2.5 summarizes the polymerization thresholds: no correlation between these values and the cross-linker percentages can be deduced. Above a certain energy density accumulated in the mixture, polymerization is not well controlled and some micro-explosions, characterized by air bubble formations, can occur. A damage threshold is difficult to define because of imperfections and inhomogeneities within the mixtures. A possible explanation for the explosion occurrence can be found in the presence of one-photon absorption from the impurities leading to locally incurred damage to the

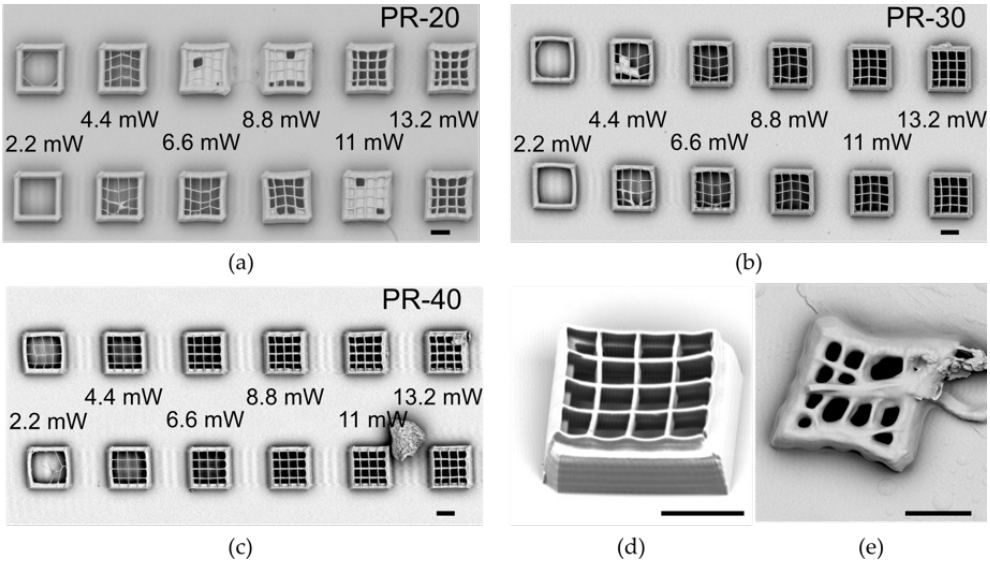

Fig. 2.20: Writing tests for the rigidity and rod dimensions at varying laser powers and writing speeds (90 μm/s for the first row and 60 μm/s for the second row). In the SEM images are shown: (a) MM-20; (b) MM-30; (c) MM-40; (d) A grid of MM-40 realized with a writing speed of 90 μm/s and a laser power of 12.9 mW; (e) a grid realized with MM-10, a writing speed of 90 μm/s, and a laser power of 12.9 mW. The scale bar is 10 μm.

polymerized structure [83]. In our case, explosions are more frequent above 16 mW, showing a broad dynamic range. To increase the structure rigidity, we can act not only on the molar percentage of the crosslinker but also on the writing parameters. Increasing the laser power and decreasing the writing speed, the crosslinking density increases, thereby reducing the possibility of the surrounding monomers swelling inside the polymerized structures [81]. This effect is relevant especially for the fabrication of suspended lines required for 3D photonic crystals, like woodpiles. Figure 2.20 shows the calibration for suspended grids up to a LCE wall for the different mixtures. MM-10 results a too soft polymer to create 3D structures, and no data are reported because the bad quality of the written structures (Figure 2.20.e). From Figure 2.20, it is clear that the structures realized with the MM-20 mixture are softer, with less sharp edges and higher thickness of the rods. Of course, increasing the amount of the crosslinker in the mixture results in the grids being more rigid and straight, as can be observed for the structure realized with MM-40 in the SEM image reported in Figure 2.20.d and recorded with the samples placed at 45°. To sort out the characteristic voxel dimensions, we analyzed the lines written on the glass-resist interface in order to evaluate the thickness (minor axis of the voxel), and we analyzed those suspended in between two walls or a grid to estimate the height (major axis of the voxel ellipsoid). Voxel dimensions as a function of the writing laser powers are reported in Figure 2.21 for MM-20 and MM-40 mixtures. For the other mixture, we can refer to the supplementary information of [85]. There is not a linear dependence in between these two quantities as also expected for the relation between the laser irradiation and degree of conversion [81]. The percentage of the crosslinker highly affects the dimension of the polymerized rods above a certain laser power value especially

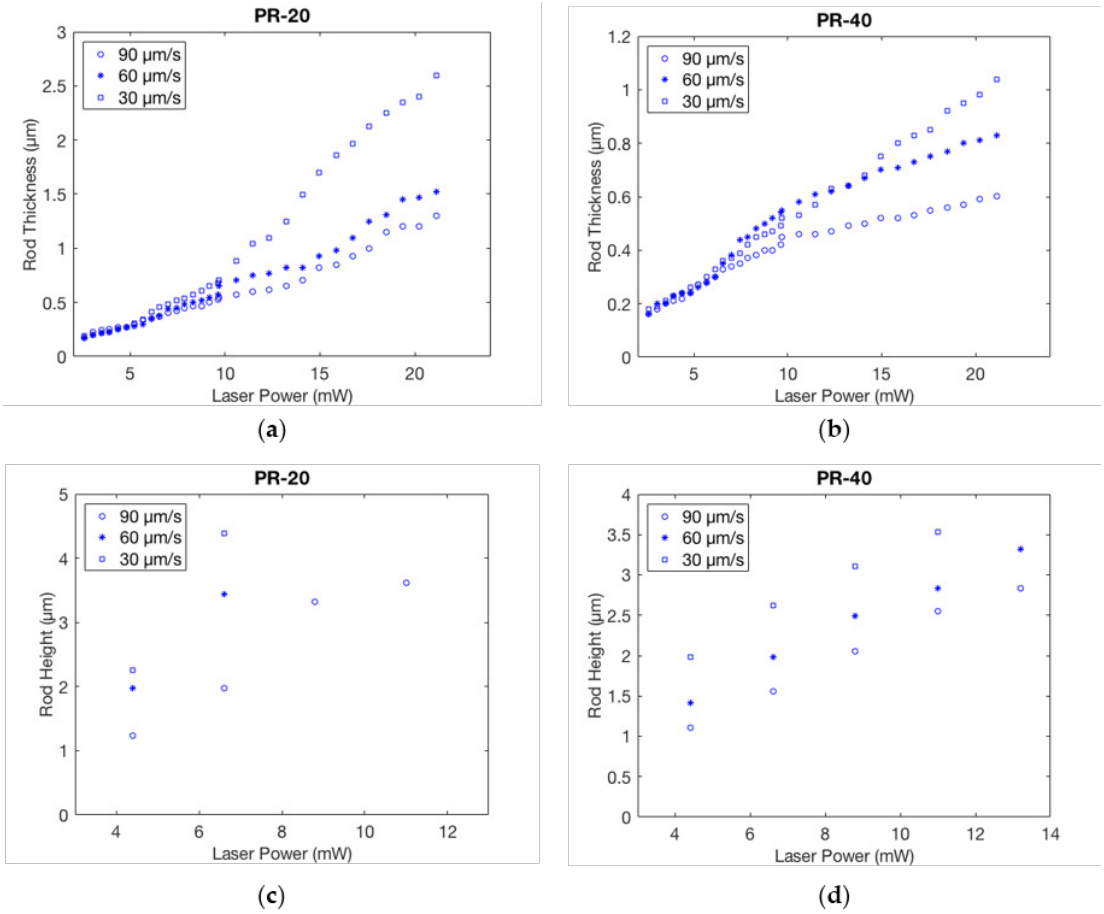

Fig. 2.21: Thicknesses and heights of the voxel depending on the writing speed and the laser power. The values are reported for PR-20 in (a,c) and PR-40 in (b,d)

for lower writing speeds. In fact, the thicknesses for MM-20 (Figure 2.21.a) realized at 30 μm/s speed reach 2.5 μm for a laser power of 20 mW, which is more than double in respect to the value for the MM-40 (Figure 2.21.b). Moreover, it is particularly significant how the voxel height in MM-20 increases while decreasing the writing speed. Even if the thickness for the different writing speeds differs by only around 100 nm, the difference in height varies from 2.3 μm to 4.4 μm. This behavior is consistent with the values reported in the literature where it is reported how an increasing writing power results in voxel lateral size saturation while the voxel height keeps increasing [86]. For less crosslinked mixtures, the higher mobility of the monomers emphasizes this unbalance, leading to thicker and taller rods. Defining the aspect ratio of the ellipsoid as the ratio between the major axis over the minor one, we observed, from Table 3, how for slower writing speeds it reaches a value of 10 for MM-20 and 7.7 for MM-40. For even higher writing speeds, the aspect ratio does not decrease below 5, while for commercial photoresist, like the IP-Dip/Ip-l (Nanoscribe GmbH), the aspect ratio is 2.7 for the writing speed of 100 μm/s [87]. With LCEs, the higher aspect ratio can be attributed to the higher refractive index value with respect to the commercial photoresist previously introduced (as Ip-Dip). In fact, the dependence of the numerical aperture on the refractive index influences the elongated shape of the voxel resulting in a higher aspect ratio. With this analysis we observed that for each mixture, the polymerization degree increases as a function of the laser power and writing speed, thereby leading to lower shrinkage of the structures during the fabrication process. Unfortunately, high exposure energy produces high voxel dimensions and the photoresist birefringence also has to be taken into account to determine the voxel aspect ratio. Increasing the crosslinker percentage is a good strategy for obtaining freestanding polymeric objects with nanometric feature sizes, and, in particular, photoresist MM-40 is the more promising option for creating suspended elements. In contrast, the resolution at threshold is almost invariant for the different writing speeds and mixtures. The contractive properties are retained for all mixtures even if the crosslinker percentage affects the actuation threshold power. Another important parameter for the three-dimensional structures is the line swelling and how this behavior affects the 3D fabrication and reproducibility [88]. To quantify this effect we define the line warping as the deviation from linearity (Figure 2.22), and is quantified averaging over the values measured on the three lines constituting each test pattern. Only the warping of horizontal lines has been considered, as the effect on vertical lines is much smaller. This is due to the temporal sequence of the writing procedure: horizontal lines have been written first, and then vertical lines; hence, vertical lines were forced not to warp by the existing constraint. The warping effect is macroscopically evident and is expected to mostly affect structures with a large aspect ratio, like long and thin rods. Moreover, large and thin structures like membranes are expected to be affected as well, since their writing procedure involves the definition of a sequence of contiguous lines. These effects can pose a challenge when looking for the realization of submicrometric photonic structures, where slight deviations from ideality can lead to significant weakening of the desired performance. Indeed, the strategies of increasing the laser power and/or reducing the writing speed may not be always viable, since both imply an increase of the voxel size. The warping effect is ultimately a consequence of polymer swelling, i.e., of the volume increase of the polymer voxels in the time interval which follows polymerization; this effect is in turn due to monomer

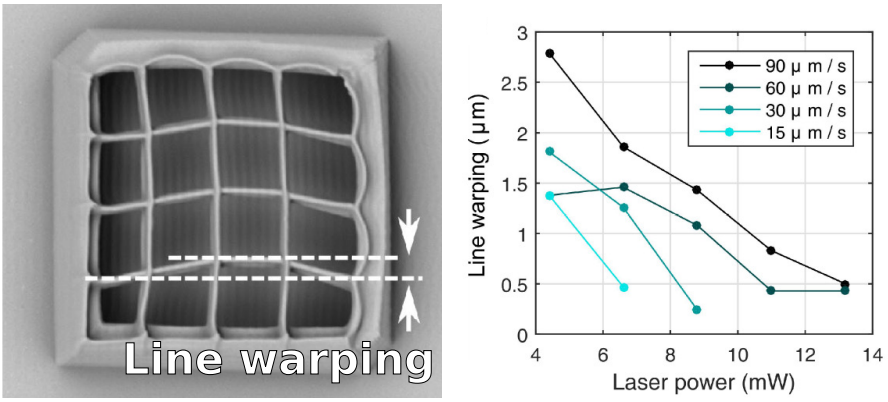

(a) (b)

Fig. 2.22: Test patterns for assessing the line warping effect. (a) Detail of a single test pattern, with the definition of line warping. (b) Dependence of line warping upon the fabrication parameters under analysis (Figure from [88].

penetration into the polymerized volumes. Being the voxel elongated in the direction orthogonal to the substrate, line warping occurs predominantly on the plane parallel to the substrate. Further studies aimed at mitigating this effect are required, similarly to what has been performed about other polymeric materials. Two different options to explore could be to write at low temperatures to decrease the monomer mobility in order to reduce the material swelling or to employ more viscous LCE resists as smectic liquid crystal elastomers.

References

[1] T. Gissibl et al. “Sub-micrometre accurate free-form optics by three-dimensional printing on single-mode fibres”. In: *Nature Communications* 7 (2016).

[2] T. Gissibl et al. “Two-photon direct laser writing of ultracompact multi-lens objectives”. In: *Nature Photonics* (2016).

[3] G. Von Freymann et al. “Three-Dimensional Nanostructures for Photonics”. In: *Advanced Functional Materials* 20.7 (2010), pp. 1038–1052.

[4] A. Radke et al. “Three-dimensional bichiral plasmonic crystals fabricated by direct laser writing and electroless silver plating”. In: *Advanced Materials* 23.27 (2011), pp. 3018–3021.

[5] J. Trull et al. “Formation of collimated beams behind the woodpile photonic crystal”. In: *Physical Review A* 84.3 (2011), p. 033812.

[6] D. Wu et al. “Femtosecond laser rapid prototyping of nanoshells and suspending components towards microfluidic devices”. In: *Lab on a Chip* 9.16 (2009), pp. 2391–2394.

[7] A. Ovsianikov et al. “Three-dimensional laser micro-and nano-structuring of acrylated poly (ethylene glycol) materials and evaluation of their cytoxicity for tissue engineering applications”. In: *Acta biomaterialia* 7.3 (2011), pp. 967–974.

[8] P. Danilevicius et al. “Micro-structured polymer scaffolds fabricated by direct laser writing for tissue engineering”. In: *Journal of biomedical optics* 17.8 (2012), pp. 0814051–0814057.

[9] K. Terzaki et al. “3D conducting nanostructures fabricated using direct laser writing”. In: *Optical Materials Express* 1.4 (2011), pp. 586–597.

[10] J. K. Gansel et al. “Tapered gold-helix metamaterials as improved circular polarizers”. In: *Applied Physics Letters* 100.10 (2012), p. 101109.

[11] L. R. Meza et al. “Resilient 3D hierarchical architected metamaterials”. In: *Proceedings of the National Academy of Sciences* 112.37 (2015), pp. 11502–11507.

[12] F. Klein et al. “Two-component polymer scaffolds for controlled three-dimensional cell culture”. In: *Advanced materials* 23.11 (2011), pp. 1341–1345.

[13] T. Grossmann et al. “Direct laser writing for active and passive high-Q polymer microdisks on silicon”. In: *Optics express* 19.12 (2011), pp. 11451–11456.

[14] Y. Zhou et al. “Microstructuring of graphene oxide nanosheets using direct laser writing”. In: *Advanced Materials* 22.1 (2010), pp. 67–71.

[15] S. Rekštytė, T. Jonavičius, and M. Malinauskas. “Direct laser writing of microstructures on optically opaque and reflective surfaces”. In: *Optics and Lasers in Engineering* 53 (2014), pp. 90–97.

[16] S. Maruo, O. Nakamura, and S. Kawata. “Three-dimensional microfabrication with two-photon-absorbed photopolymerization”. In: *Optics letters* 22.2 (1997), pp. 132–134.

[17] M. Thiel et al. “Direct laser writing of three-dimensional submicron structures using a continuous-wave laser at 532 nm”. In: *Applied Physics Letters* 97.22 (2010), p. 221102.

[18] S. Kawata et al. “Finer features for functional microdevices”. In: *Nature* 412.6848 (2001), pp. 697–698.

[19] S. W. Hell and J. Wichmann. “Breaking the diffraction resolution limit by stimulated emission: stimulated-emission-depletion fluorescence microscopy”. In: *Optics letters* 19.11 (1994), pp. 780–782.

[20] J. Fischer, G. von Freymann, and M. Wegener. “The Materials Challenge in Diffraction-Unlimited Direct-Laser-Writing Optical Lithography”. In: *Advanced materials* 22.32 (2010), pp. 3578–3582.

[21] F. Formanek et al. “Three-dimensional fabrication of metallic nanostructures over large areas by two-photon polymerization”. In: *Optics express* 14.2 (2006), pp. 800–809.

[22] T. Bückmann et al. “Tailored 3D mechanical metamaterials made by dip-in direct-laser-writing optical lithography”. In: *Advanced Materials* 24.20 (2012), pp. 2710–2714.

[23] J. B. Mueller et al. “Polymerization Kinetics in Three-Dimensional Direct Laser Writing”. In: *Advanced Materials* 26.38 (2014), pp. 6566–6571.

[24] V. R. Manfrinato et al. “Resolution limits of electron-beam lithography toward the atomic scale”. In: *Nano letters* 13.4 (2013), pp. 1555–1558.

[25] J. W. Lussi et al. “Selective molecular assembly patterning at the nanoscale: a novel platform for producing protein patterns by electron-beam lithography on SiO2/indium tin oxide-coated glass substrates”. In: *Nanotechnology* 16.9 (2005), p. 1781.

[26] A. A. Tseng et al. “Electron beam lithography in nanoscale fabrication: recent development”. In: *IEEE Transactions on electronics packaging manufacturing* 26.2 (2003), pp. 141–149.

[27] C. Vieu et al. “Electron beam lithography: resolution limits and applications”. In: *Applied Surface Science* 164.1 (2000), pp. 111–117.

[28] S. I. Bozhevolnyi et al. “Channel plasmon subwavelength waveguide components including interferometers and ring resonators”. In: *Nature* 440.7083 (2006), pp. 508–511.

[29] L. Novotny and N. Van Hulst. “Antennas for light”. In: *Nature Photonics* 5.2 (2011), pp. 83–90.

[30] D. Lin et al. “Dielectric gradient metasurface optical elements”. In: *science* 345.6194 (2014), pp. 298–302.

[31] N. Engheta. “Circuits with light at nanoscales: optical nanocircuits inspired by metamaterials”. In: *Science* 317.5845 (2007), pp. 1698–1702.

[32] A. Alù and N. Engheta. “Achieving transparency with plasmonic and metamaterial coatings”. In: *Physical Review E* 72.1 (2005), p. 016623.

[33] S. Fan et al. "High extraction efficiency of spontaneous emission from slabs of photonic crystals". In: *Physical Review Letters* 78.17 (1997), p. 3294.

[34] B.-S. Song et al. "Ultra-high-Q photonic double-heterostructure nanocavity". In: *Nature materials* 4.3 (2005), pp. 207–210.

[35] M. Schumann et al. "Hybrid 2D-3D optical devices for integrated optics by direct laser writing". In: *Light: Science and Applications* 3.6 (2014), e175.

[36] Y.-G. Zhao et al. "Polymer waveguides useful over a very wide wavelength range from the ultraviolet to infrared". In: *Applied Physics Letters* 77.19 (2000), pp. 2961–2963.

[37] Y. Enami et al. "Hybrid electro-optic polymer/sol–gel waveguide modulator fabricated by all-wet etching process". In: *Applied physics letters* 83.23 (2003), pp. 4692–4694.

[38] Q. Xia et al. "Ultrafast patterning of nanostructures in polymers using laser assisted nanoimprint lithography". In: *Applied physics letters* 83.21 (2003), pp. 4417–4419.

[39] Y. Xia et al. "Complex optical surfaces formed by replica molding against elastomeric masters". In: *Science* 273.5273 (1996), p. 347.

[40] A. Ovsianikov et al. "Ultra-low shrinkage hybrid photosensitive material for two-photon polymerization microfabrication". In: *Acs Nano* 2.11 (2008), pp. 2257–2262.

[41] S. J. Woltman, G. D. Jay, and G. P. Crawford. "Liquid-crystal materials find a new order in biomedical applications". In: *Nature materials* 6.12 (2007), pp. 929–938.

[42] B. Maune et al. "Electrically tunable ring resonators incorporating nematic liquid crystals as cladding layers". In: *Applied physics letters* 83.23 (2003), pp. 4689–4691.

[43] C.-T. Wang et al. "Optical bistability in a silicon nitride microring resonator with azo dye-doped liquid crystal as cladding material". In: *Optics express* 21.9 (2013), pp. 10989–10994.

[44] H. Jiang, S. Kelch, and A. Lendlein. "Polymers move in response to light". In: *Advanced Materials* 18.11 (2006), pp. 1471–1475.

[45] M. Warner and E. M. Terentjev. *Liquid crystal elastomers*. Vol. 120. OUP Oxford, 2003.

[46] H. Finkelmann, H.-J. Kock, and G. Rehage. "Investigations on liquid crystalline polysiloxanes 3. Liquid crystalline elastomers—a new type of liquid crystalline material". In: *Die Makromolekulare Chemie, Rapid Communications* 2.4 (1981), pp. 317–322.

[47] T. J. White and D. J. Broer. "Programmable and adaptive mechanics with liquid crystal polymer networks and elastomers". In: *Nature materials* 14.11 (2015), pp. 1087–1098.

[48] A. Elias et al. "Photopatterned liquid crystalline polymers for microactuators". In: *Journal of Materials Chemistry* 16.28 (2006), pp. 2903–2912.

[49] A. Buguin et al. "Micro-actuators: When artificial muscles made of nematic liquid crystal elastomers meet soft lithography". In: *Journal of the American Chemical Society* 128.4 (2006), pp. 1088–1089.

[50] H. Zeng et al. “High-resolution 3D direct laser writing for liquid-crystalline elastomer microstructures”. In: *Advanced materials* 26.15 (2014), pp. 2319–2322.

[51] C. Ohm, M. Brehmer, and R. Zentel. “Liquid crystalline elastomers as actuators and sensors”. In: *Advanced Materials* 22.31 (2010), pp. 3366–3387.

[52] F. Brömmel, D. Kramer, and H. Finkelmann. “Preparation of liquid crystalline elastomers”. In: *Liquid Crystal Elastomers: Materials and Applications*. Springer, 2012, pp. 1–48.

[53] L. T. de Haan, A. P. Schenning, and D. J. Broer. “Programmed morphing of liquid crystal networks”. In: *Polymer* 55.23 (2014), pp. 5885–5896.

[54] Y. Yu, M. Nakano, and T. Ikeda. “Photomechanics: directed bending of a polymer film by light”. In: *Nature* 425.6954 (2003), pp. 145–145.

[55] T. Ikeda, J.-i. Mamiya, and Y. Yu. “Photomechanics of liquid-crystalline elastomers and other polymers”. In: *Angewandte Chemie International Edition* 46.4 (2007), pp. 506–528.

[56] M.-H. Li et al. “Light-Driven Side-On Nematic Elastomer Actuators”. In: *Advanced Materials* 15.7-8 (2003), pp. 569–572.

[57] H. Zeng et al. “Alignment engineering in liquid crystalline elastomers: Free-form microstructures with multiple functionalities”. In: *Applied Physics Letters* 106.11 (2015), p. 111902.

[58] P. J. Collings and M. Hird. *Introduction to liquid crystals: chemistry and physics*. CRC Press, 1997.

[59] H. Zeng et al. “Light-Fueled Microscopic Walkers”. In: *Advanced Materials* 27.26 (2015), pp. 3883–3887.

[60] S. Palagi et al. “Structured light enables biomimetic swimming and versatile locomotion of photoresponsive soft microrobots”. In: *Nature materials* (2016).

[61] D. L. Thomsen et al. “Liquid crystal elastomers with mechanical properties of a muscle”. In: *Macromolecules* 34.17 (2001), pp. 5868–5875.

[62] I. Dierking. *Textures of liquid crystals*. John Wiley & Sons, 2003.

[63] D. Liu and D. J. Broer. “Liquid crystal polymer networks: preparation, properties, and applications of films with patterned molecular alignment”. In: *Langmuir* 30.45 (2014), pp. 13499–13509.

[64] H. Shahsavan et al. “Smart Muscle-Driven Self-Cleaning of Biomimetic Microstructures from Liquid Crystal Elastomers”. In: *Advanced Materials* 27.43 (2015), pp. 6828–6833.

[65] H. D. Bandara and S. C. Burdette. “Photoisomerization in different classes of azobenzene”. In: *Chemical Society Reviews* 41.5 (2012), pp. 1809–1825.

[66] G. N. Mol et al. “Thermo-Mechanical Responses of Liquid-Crystal Networks with a Splayed Molecular Organization”. In: *Advanced Functional Materials* 15.7 (2005), pp. 1155–1159.

[67] D. J. Broer et al. "In-situ photopolymerization of oriented liquid-crystalline acrylates, 3. Oriented polymer networks from a mesogenic diacrylate". In: *Die Makromolekulare Chemie* 190.9 (1989), pp. 2255–2268.

[68] Y. Galerne and J. Marcerou. "Temperature behavior of the order-parameter invariants in the uniaxial and biaxial nematic phases of a lyotropic liquid crystal". In: *Physical review letters* 51.23 (1983), p. 2109.

[69] R. A. Hikmet. "Anisotropic gels in liquid crystal devices". In: *Advanced Materials* 4.10 (1992), pp. 679–683.

[70] J. Küpfer and H. Finkelmann. "Nematic liquid single crystal elastomers". In: *Die Makromolekulare Chemie, Rapid Communications* 12.12 (1991), pp. 717–726.

[71] J. Schätzle, W. Kaufhold, and H. Finkelmann. "Nematic elastomers: The influence of external mechanical stress on the liquid-crystalline phase behavior". In: *Die Makromolekulare Chemie* 190.12 (1989), pp. 3269–3284.

[72] D. A. Balzarini. "Temperature dependence of birefringence in liquid crystals". In: *Physical Review Letters* 25.14 (1970), p. 914.

[73] J. Li and S.-T. Wu. "Extended Cauchy equations for the refractive indices of liquid crystals". In: *Journal of applied physics* 95.3 (2004), pp. 896–901.

[74] J. Li, S. Gauzia, and S.-T. Wu. "High temperature-gradient refractive index liquid crystals". In: *Optics express* 12.9 (2004), pp. 2002–2010.

[75] S.-T. Wu, U. Efron, and L. D. Hess. "Birefringence measurements of liquid crystals". In: *Applied optics* 23.21 (1984), pp. 3911–3915.

[76] M. Warenghem and G. Joly. "Liquid crystals refractive indices behavior versus wavelength and temperature". In: *Molecular Crystals and Liquid Crystals* 207.1 (1991), pp. 205–218.

[77] S. Brugioni, S. Faetti, and R. Meucci. "Mid-infrared refractive indices of the nematic mixture E7". In: *Liquid crystals* 30.8 (2003), pp. 927–930.

[78] J. Li et al. "Infrared refractive indices of liquid crystals". In: *Journal of Applied Physics* 97.7 (2005), p. 073501.

[79] L. Abdulkareem et al. "Temperature effect on nonlinear refractive indices of liquid crystals in visible and NIR". In: *Optics Communications* 363 (2016), pp. 188–194.

[80] S. Brugioni and R. Meucci. "Refractive indices of the nematic mixture E7 at 1550nm". In: *Infrared physics & technology* 49.3 (2007), pp. 210–212.

[81] A. Žukauskas et al. "Tuning the refractive index in 3D direct laser writing lithography: towards GRIN microoptics". In: *Laser & Photonics Reviews* 9.6 (2015), pp. 706–712.

[82] M. Malinauskas, P. Danilevičius, and S. Juodkazis. "Three-dimensional micro-/nano-structuring via direct write polymerization with picosecond laser pulses". In: *Optics express* 19.6 (2011), pp. 5602–5610.

[83] J. Fischer et al. "Three-dimensional multi-photon direct laser writing with variable repetition rate". In: *Optics express* 21.22 (2013), pp. 26244–26260.

[84] M. Malinauskas et al. “Ultrafast laser nanostructuring of photopolymers: A decade of advances”. In: *Physics Reports* 533.1 (2013), pp. 1–31.

[85] S. Nocentini et al. “Photoresist Design for Elastomeric Light Tunable Photonic Devices”. In: *Materials* 9.7 (2016), p. 525.

[86] H.-B. Sun, T. Tanaka, and S. Kawata. “Three-dimensional focal spots related to two-photon excitation”. In: *Applied physics letters* 80.20 (2002), pp. 3673–3675.

[87] M. Deubel et al. “Direct laser writing of three-dimensional photonic-crystal templates for telecommunications”. In: *Nature materials* 3.7 (2004), pp. 444–447.

[88] S. Nocentini et al. “Towards liquid crystalline elastomer optically tunable photonic microstructures”. In: *SPIE Nanoscience+ Engineering*. International Society for Optics and Photonics. 2016, pp. 992025–992025.

CHAPTER 3

2D tunable optical microstructured array

In this chapter, we demonstrate how the concepts exposed in the previous part can be applied to photonics. In particular, the DLW lithographic technique enables the fabrication of 3D photonic component in different polymeric matrices.
The key point of this work is one of the most desirable photonic property: tunability. The requirement for tunability is evident in view of applications such as flexible networks, reconfigurable switches, and displays, but also in more theoretical studies as, for example, those about weak and strong coupling of emitters with resonant cavities. Among all the complex photonic structure design, our attention has been attracted, at the beginning, by simple and demonstrative devices: the bi-dimensional gratings. This structure offers many applications depending on the operational wavelength. We will show how an optical beam steerer for the visible range can be realized. More complex physics has been studied for a LCE 1D periodic structure: a guided mode resonance filter (GMRF) for the telecommunication band. The striking point of the investigated structures is the chance to tune their optical properties through light-driven shape and refractive index change of the LCE polymers in a remote and non invasive way.

3.1 Microstructured dielectric periodic arrays

Periodic arrays of scattering elements have a very long scientific history, starting more than a century ago with the concept of diffraction grating. Despite their apparent simplicity, the rich variety of their optical properties has driven continuous efforts and interest in the nanophotonics community, pushed ahead by the huge development of technological and material capabilities. We consider resonant microstructured arrays and gratings illuminated by free-space plane waves. Their optical behavior can be generally described starting for their typical periodic lengthscale. 2D elements, arranged in semi-infinite dielectric membranes (slabs surrounded by a vacuum), periodically microstructured in one dimension, are depicted in Figure 3.1. In the 1D case, the

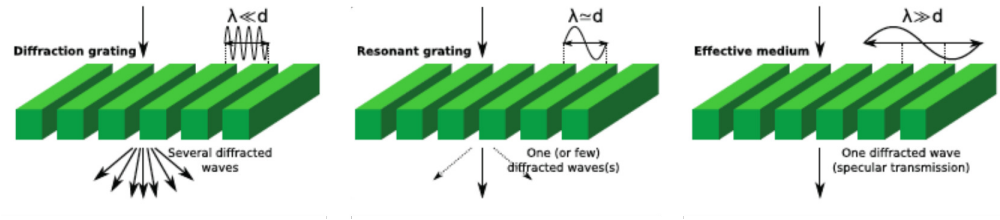

(a) (b) (c)

Fig. 3.1: 1D free-standing dielectric period structure in different regimes: (a) diffraction grating, (b) resonant (sub-wavelength) grating and (c) effective medium slab (Image from [1].

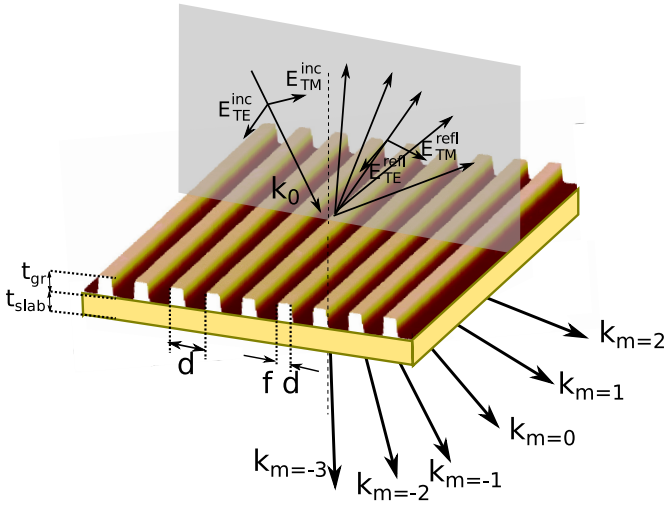

Fig. 3.2: Electric field components choice and geometric parameter description for light impinging on a 1D diffractive grating.

structure is ideally infinite in y and infinitely periodic in x, the electromagnetic solutions are independent of y. In 2D, the structure is ideally infinitely periodic in x and y. The electromagnetic field above and below a 2D array is described as the sum of propagating and evanescent plane waves (Rayleigh expansion), whose in-plane wavevectors $\vec{k}_p^{(m,q)}$ are quantized:

$$\vec{k}_p^{(m,q)} = \left(k_{x,0} + m\frac{2\pi}{d_x}\right)\hat{x} + \left(k_{y,0} + q\frac{2\pi}{d_y}\right)\hat{y} \tag{3.1}$$

where $k_{x,0}\hat{x} + k_{y,0}\hat{y}$ is the in-plane wavevector of an incident plane wave, (d_x, d_y) are the periods of the array along the directions given by the unit vectors $(\hat{x}, \hat{y})$ and (m, q) are integers. The basics of the electromagnetic theory of gratings and periodic nanostructures can be found in [2].
A simple dielectric membrane of sub-wavelength thickness with a refractive index n, drilled with a periodical arrangement of 1D rectangular grooves is mostly characterized by the ratio of the period d to the wavelength λ. In the short wavelength range ($\lambda \ll d$), the periodic structure acts as a diffraction grating. In the long wavelength limit ($\lambda \gg d$),

the membrane behaves like a homogeneous layer with an effective refractive index, in accordance with the effective medium theory. In the case of slightly sub-wavelength gratings ($\lambda \geq d$), different regimes can be depicted, depending on the filling fraction f. For $f \to 1$, sub-wavelength dielectric gratings exhibit guided mode resonance (GMR) effects [3]. For $f \sim 0.5$, the structure is often referred as a photonic crystal PC slab whose optical properties are basically described by interference effects. Their most peculiar property is that, below the light cone ,[1] photonic crystals exhibit a photonic band gap (PBG) or a stop band depending on the refractive index contrast of the structure respect to the surrounding medium. Above the light cone, guided modes can interact with free-space radiation in complex ways [4]. For $f \to 0$, the structure can no longer be described as a guided-mode structure: it is made of nanorods with a diameter much smaller than the wavelength and its optical response can be described by a simple model based on multiple scattering [5]. We will consider here only structures with a periodicity close to the wavelength as GMR filters and diffractive grating whose periodicity is larger than the wavelength of the impinging beam. These latest structures can be employed as beam steerer if their optical properties, as the diffraction angle can be controlled by an external stimulus. To reach the higher degree of non-invasiveness and a remote reversible control, we chose light as triggering signal.

3.2 Beam steering

Most of the systems for optical-beam deflection and modulation are of rather large dimensions. Nowadays, diffractive optical elements are versatile components with a huge variety of optical applications, not only as beam steerer, but also ranging from holograms [6] to diffractive mirrors for lasers [7] and optical tweezers [8]. A non-mechanical beam steering diffraction device is a critical component in many optical systems, optical interconnects [9], optical communications [10], projection displays [11], and optical data storage [12]. These diverse applications of high-performance beam steering devices entice further innovation of this appealing technology. It should be noticed that traditional beam steering techniques are based on charge excitation in semiconductors, electromechanical, thermo-optic [13] and acousto-optic phenomena [14]. The latters offer switching times of microseconds but many applications require switching times on the order of a few milliseconds, which can be also realized by means of piezo-electrical actuators. We would like to reproduce these results but in a non invasive way pushing the research lines towards the optical control of phase change materials (as liquid crystal).
The spatial period and structure height are the significant characteristics of diffractive micro-optical elements, typically in the range of a few micrometers. Depending on the material properties, the optical features can be slightly tuned through an electric field signal that can change the electro-optic properties or the alignment of liquid crystals; if materials with small Young modulus are employed, a mechanichal deformation can also

[1] In a band diagram representation, the projected (along one reciprocal space direction) band structure of all states in the bulk substrate/superstrate versus their in-plane wavevector component are reported and creates a map of what states can radiate vertically and what states can propagate inside the structure. Only states with a wave vector larger than the vacuum wave number k_0 at that frequency are strictly confined. These states are located under the line that defines the propagation in free space, the so-called light-cone defined by $|k_0| = \omega/c_0$.

be applied. Without applying an external mechanical [15] or electrical field, in terms of tuning grating periods, this restriction can be overcome by elastic, rubber-like materials sensitive to light stimuli as the previously introduced liquid crystal elastomers (Chapter 2). Recently one of the most investigated switching mechanism is the optically induced beam steering based on liquid crystal. In literature, electrically activated macroscopic devices have been described: a wide-angle non-mechanical beam steerer utilizing polarization gratings has been proposed and demonstrated [16]. Another proposed alternative is constituted by chiral liquid crystal (CLC)-based diffraction gratings that feature non-mechanical beam steering, precision steering with full beam agility in addition to small size, reduced weight, and low power consumption [17]. A significant result has been reported in [18] where the presented optically tunable beam steering grating is based on a high helical twisting power that generates a light-driven axially chiral molecular switch-doped CLC fingerprint texture. The significant changes of the chiral molecular conformation, switched upon photo-isomerization, vary the pitch of CLC [19], and consequently shifts the diffraction angle of the CLC grating. Another demonstration of application of CLC to beam steering, that triggered much scientific interest, can be found in [20]. They report three-dimensional manipulation of the helical axis of a CLC, together with inversion of its handedness, achieved solely with a light stimulus. This technique carries out light-activated, wide-area, reversible two-dimensional beam steering. During the three-dimensional manipulation by light, the helical axis undergoes, in sequence, a reversible transition from perpendicular to parallel, followed by in-plane rotation on the substrate surface. Many examples of LCE diffraction grating are described by Čopič group. They show how macroscopic holographic gratings, realized on liquid crystalline elastomeric soft films, can be easily tuned either by temperature modification or by straining with a grating lattice deformation dynamics on the minutes scale [21, 22]. Polarization analysis as clamped/free sample constraints is investigated in [23]. All the presented works show a light-driven beam steering on the time scale of tens of seconds. To the best of our knowledge, we are going to explain the first LCE beam steerer with an actuation time-scale of milliseconds.

3.2.1 LCE enabled beam steering

The working mechanism of beam steering grating is very simple. It is based on the diffraction law. In fact, considering a grating at normal incidence, the angular separation as a function of wavelength is determined from the basic grating relation:

$$m\lambda = d\sin(\theta_m(\lambda)) \tag{3.2}$$

where $\theta_m(\lambda)$ is the separation angle, d is the grating period, and m is the diffraction order. If a white light is used and the grating behaves as a dispersive element, at larger angles of the diffracted orders, the larger wavelengths would be measured. If a monocromatic light is employed instead, the diffraction angles depend only on the grating pitch. In this case, the elastic grating deformation induces a laser beam steering for the diffracted order, allowing a fully optical control of light direction, with a selection of different channels (scheme in Figure 3.3). The possibility to integrate liquid crystalline elastomeric structures to remotely switch, through light activation, the optical signal offers a new interesting approach. In perspective, this method responds to the power

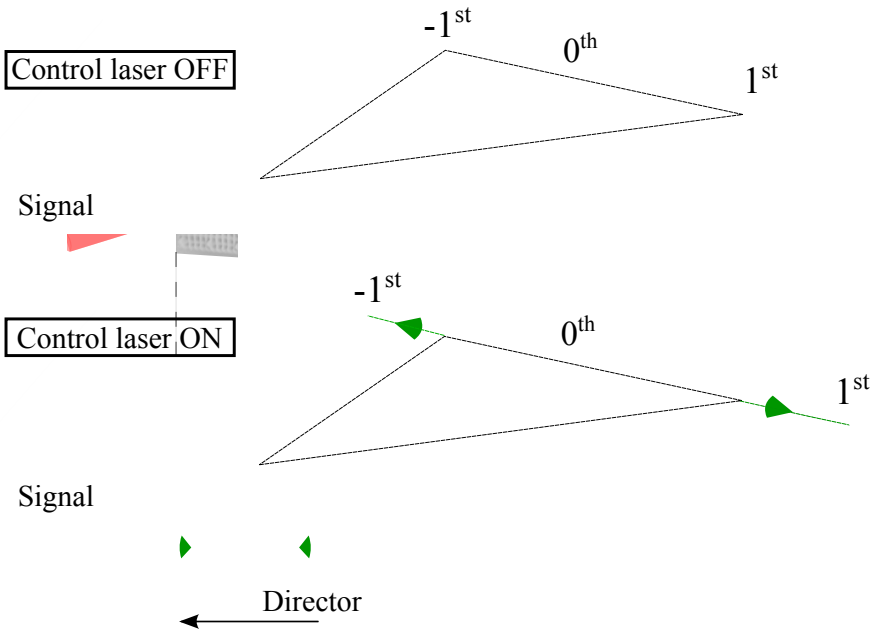

Fig. 3.3: Working mechanism scheme of the LCE grating beam steering.

consuming issues, to the integration of bulky controllers (electrodes, heaters..) and to the time speed actuation problems.

Angular deviation

We propose a tunable liquid crystalline elastomeric micro-grating able to deform, and therefore change the diffraction angle, in response to a light stimulus.
The LCE mixture employed as monomeric matrix for the structure fabrication is the one presented in Section 2.2.3, MM-30. This choice has been driven by the higher rigidity of the mixture, without losing much elasticity. Thanks to the mixture characterization and voxel dimension estimation (reported in the previous chapter and in [24]) with the DLW system, the right power value parameters have been set in the writing program file in such a way to obtain the desired height of the grating slab.
The realized 2D grating has a cell pitch of 1.5 μm as shown in the rendering in Figure 3.4.a. The liquid crystal molecule alignment for these structures is homogeneous uniaxial with the director parallel to one of the grating axis. The structure is sustained from pillars and kept at 5 μm from the glass substrate to increase the refractive index contrast of the photonic slab respect to the surrounding environment and to remove the glass constraint. The number of pillars has been chosen in such a way to guarantee the stability of the structure but trying to minimize their contribute both from the optical point of view, as scatterers, and from the mechanical one as anchors that can limit the grating elasticity. However from the SEM picture, Figure 3.4.b, we can appreciate that due to the softness of the LCE polymer, the structure periodicity is not perfectly preserved. The effect of beam diffraction for a red laser light (He-Ne laser) is however clearly visible. It can be observed in Figure 3.5 as the not perfect structure periodicity convoluted with the device pedestal response results in different intensity diffracted

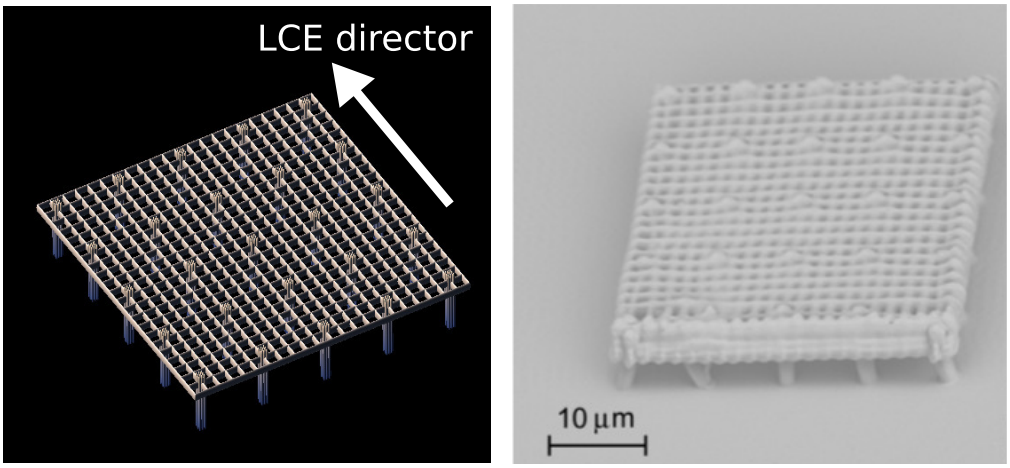

(a) (b)

Fig. 3.4: LCE grating realized with the DLW technique: (a) a 3D rendering of the structure; (b) a SEM image of the real self standing structure.

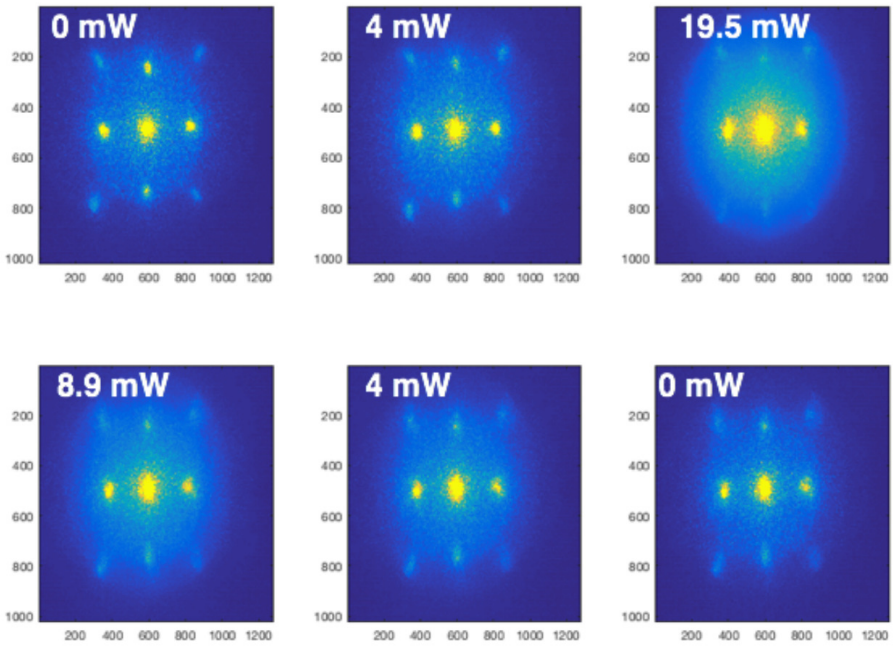

Fig. 3.5: LCE grating diffracted patterns for different green laser powers.

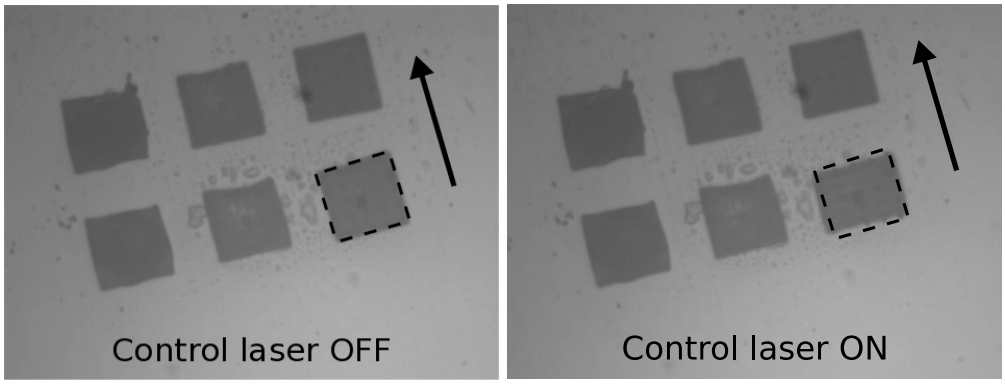

(a) (b)

Fig. 3.6: Optical image of the LCE grating: (a) the green control laser is off and then (b) it has been turned on and the structure contracts along the alignment direction (indicated with the arrow) and expands in the perpendicular one.

peaks and a weak speckle pattern especially around the zero order (not diffracted) beam. Whereas the grating "legs" could have been fabricated from hard polymer, we chose to use a soft elastic material matrix, as the elastomer, to have a larger grating deformation (since the structure contraction is not limited rigid pillar).
To activate the optical deformation and therefore the beam steering, a continuous-wave green laser has been employed. The optical setup for the diffraction experiment is then pretty simple and it is constituted by a probe red light and a green laser pump. Both are slightly focused on the structure to have a beam waist diameter comparable with the structure size, 40 µm. The diffraction pattern is then imaged in two different depending on the type of experiment. To follow the evolution dynamics upon green power variation, a commercial microscope is used. In a second part, the temporal grating response will be analyzed: in this case, a chopper has been used to modulate the laser excitation and a fast camera to record the position of the diffracted beams. Once the green light, through a light-driven effect, converts the light energy in heat, thanks to the dye absorption, and therefore into a mechanical elastic deformation, the grating contracts along the director and expand in the other in-plane direction (Figure 3.6). The result is a pitch reduction along the director with a consequent diffraction angle reduction. An opposite behavior is observed for the other grating axis, perpendicular to the director, where the order parameter change causes a structure expansion and a diffraction angle increase. In Figure 3.5 the diffraction patterns of the LCE grating varying the excitation green laser power are shown. If the diffracted spot intensities, along the x and y directions (Figure 3.7.a-b), are reported as function of the camera pixel position, we can retrieve the relative position shift (Figure 3.7.c-d). To evaluate the central position of the spot and subsequently individuate the structure percentual deformation, a four-Gaussian profile curve has been used to fit the experimental data. The graphs underline that the percentage of the variation of the diffracted beam increases with the green power excitation. Even if we can recognize that the in-plane grating deformation is not perfectly symmetric due to some structural defects, or pedestal strain, the 1st diffraction order displacement achieve the 20% for 19.5 mW. This value is consistent with the LCE maximum contraction (along

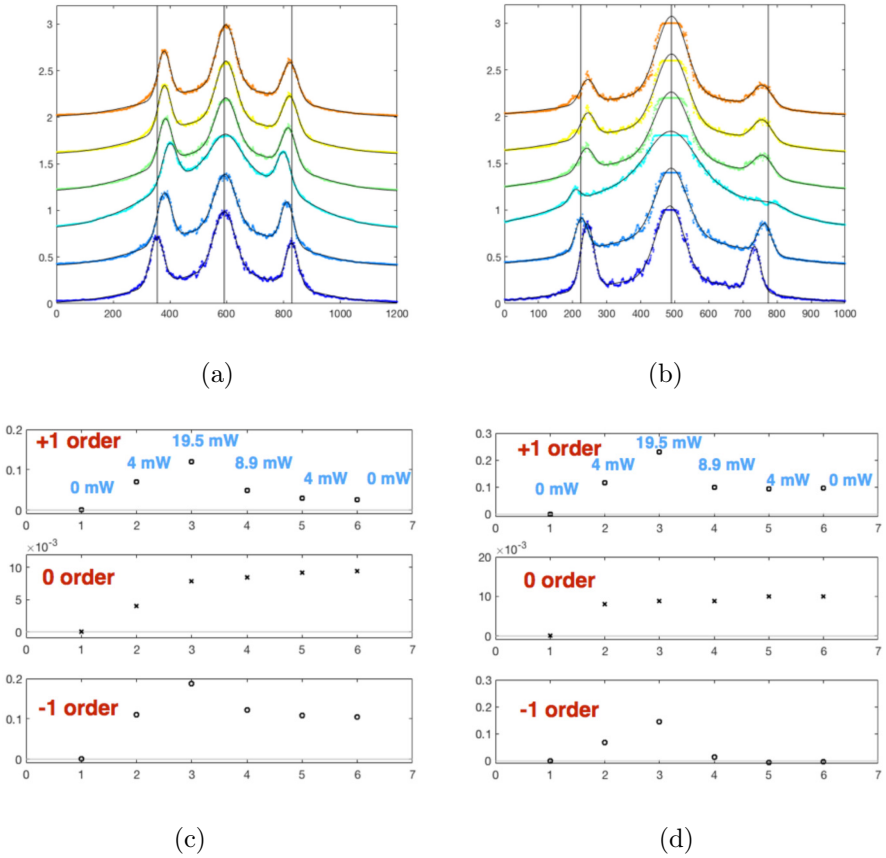

Fig. 3.7: (a) Intensity profiles of the diffracted spots along x.(b) Intensity profiles of the diffracted spots along y. The convolution curves have been fitted with a 4 Gaussian envelop function (one Gaussian curve reproduces the brackground); (c)-(d) The percentage deformations of the diffracted spots is reported for the different powers.

the director). In fact, if we assume that the angular deviation of the first diffracted order is linear with the pitch deformation, the relative beam position variation should be as large as the grating size difference. It is also important to notice that the two in-plane deformations are comparable. This effect is counterintuitive because we expect to have a volume conservation. We measure instead a contraction of 20% along the director axis that should be distributed (following the same behavior of other studied structures) in the two perpendicular directions (i.e. the direction parallel to the glass and perpendicular to the director and the direction perpendicular to the glass). However, due to the particular geometrical shape of the analyzed grating (a drilled thick LCE slab of 5 μm, with squared air holes), it is really difficult to evaluate the volume redistribution of the reduced length in the other two direction. From this measurement and assuming that the diffracted angle variation scales linearly with the grating pitch deformation, we can assume that the grating thickness remains almost unchanged. The zero order beam, that is transmitted through the structure, keeps the starting position (green laser off) with an error of the 1%.

Photo-bleaching

The reversible reshaping of the structures is due to the soft nature of the material that at the same time has an elastic behavior depending on the cross-linker percentage inside the LCE mixture. The elastic response is however triggered by the azo-dye absorption that converts the green laser light into heat allowing the transition from the nematic state to the para-nematic state of the polymeric structures [25, 26]. This transition from the *trans* (liquid crystal molecules aligned along the preferential direction, director) to the *cis* (liquid crystal molecules lose their order reaching the isotropic phase) state - called isomerization - brings the dye molecule in an excited state from which it decays to the fundamental one through a thermal relaxation process. In this way the light energy is transferred to the material into heat. The *trans-cis* transition is a chemical transformation that entails molecule rearrangement and can provoke N=N bond breakdown [27]. The *trans* isomer is of an elongated shape, often nematogenic by itself, while the *cis* isomer is bent and therefore incompatible with nematic ordering. So the light, inducing *cis* isomers in a nematic host, reduces the nematic order and, in LCE, this also results in large deformations. Experiments demonstrate that the main photobleaching mechanism is the photo-chemical decomposition of the chromophore and its azo-bond [28]. Moreover during the photobleaching process, in a strongly absorbing material, the photons responsible for the bleaching reaction can not penetrate deeply into the film, thus converting only chromophores near the surface. Once these molecules are bleached and their absorptivity decreases so that the light can penetrate deeper inside the film. Hence, an interface between bleached and non-bleached polymer gradually moves through the film during the bleaching process.
Considering the diffractive grating structure, we deal with a particular geometry: a thin slab of 5 μm thickness with a periodic pattern of squared air holes. In this case it is difficult to evaluate the photobleaching profile even if we know from some not shown experiments that the absorption length of our LCE polymeric matrix is 6 μm. This is the reason that motivates a direct measurement of photobleaching time of the considered structures. The time is not the only influent parameter in the photobleaching evaluation.

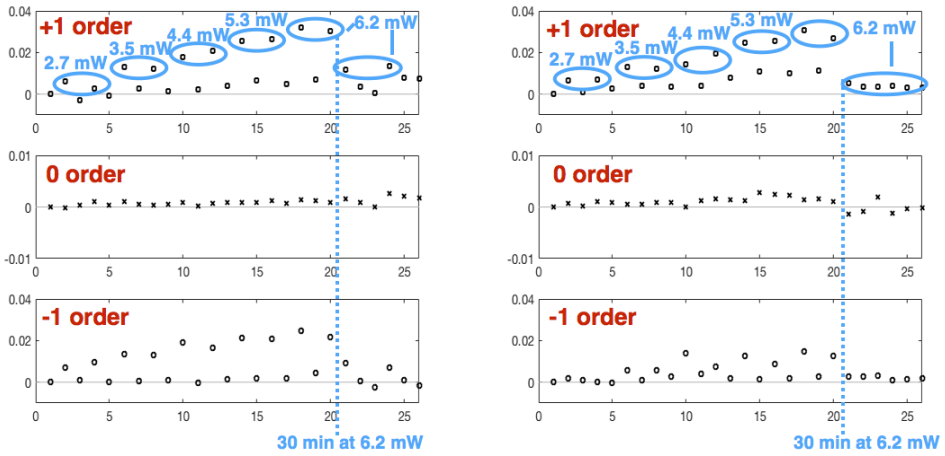

(a) (b)

Fig. 3.8: The percentage deformations of the diffracted spots is reported for the different powers to test the photobleatching times for (a) the x axis contraction and (b) the y axis expansion.

In fact the power of the green laser that activates the *trans-cis* transition, strongly affects the photobleaching process. During an experimental test, a given laser power has been kept for 1 min and then switched to zero. For each laser power, this step has been repeated two times, as reported in Figure 3.8 (the x axis represents the procedure step number). Once reached a laser power of 6.2 mW, the sample was left under these conditions for 30 min. After this time interval, the structure was not able to deform anymore and it only partially recovered the initial shape. It means that our structures, at the moment, suffer photo-bleaching problems. In our laboratories the synthesis of another much stable dye (in other field, mostly textile applications, this dye exhibits a good photo-bleaching endurance [29]) has been already developed but it has not been tested and implemented for the DLW system. We did not bring the laser power to the value which generated the maximum expansion because we would like to find the longer time that the sample could maintain its elasticity. For the moment, photobleaching represents a limitation for technological applications but it is still an on-going research especially from the material point of view.

Temporal steering dynamics

A key feature that characterizes the beam steerer properties is temporal response.
To test the LCE grating response time, evolution measurements have been done with a fast camera recording the diffraction pattern of a He-Ne laser focused (in order to illuminate the whole central part of the structure, avoiding the edge scattering) on the grating structure. The green laser actuation is modulated with a chopper set at 100 Hz. The camera acquisition frame rate is 10 kHz in order to follow the grating dynamics in each modulation period. To determine exactly each chopper period, on the camera field of view also the green modulated laser has been imaged. In this way, both laser lights, the modulation and the diffracted signal, can be monitored and recorded together

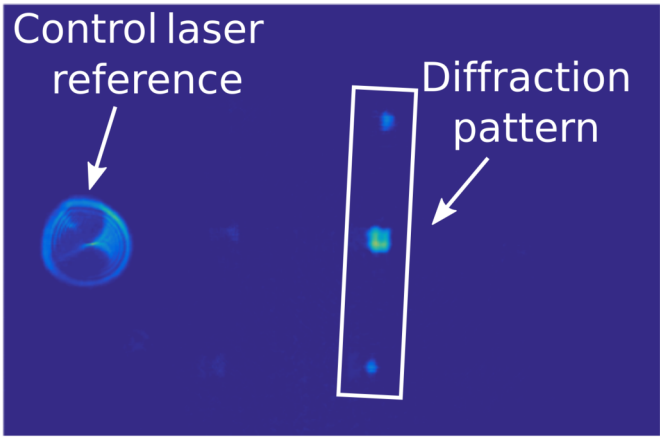

Fig. 3.9: An image taken with the fast camera. On the left the reference signal of the modulated green light, on the right the grating diffraction pattern.

Green laser power	t_{contr}	t_{relax}	Contraction
1.25 mW	0.95 ms	0.47 ms	6%
1.6 mW	0.96 ms	0.46 ms	8.7%
2.25 mW	0.85 ms	0.36 ms	10%
2.8 mW	0.59 ms	0.4 ms	13.4%
1.25 mW	1.02 ms	0.5 ms	4%

Table 3.1: Contraction and relaxation times (respectively t_{contr} and t_{relax}) and light induced contraction of LCE diffraction gratings.

(Figure 3.9). Many cycles have been recorded and a value for the "raising" time (defined as the time needed to reach the maximum grating deformation for each excitation green laser power) and "relaxation" time (defined as the time needed to recover the initial shape once the green laser has been turned off) have been individuated. From the dynamic traces, the exponentials behaviors has been fitted with exponential functions (Figure 3.10). This measurement has been repeated for different power values, before increasing it and decreasing it afterwards. The typical times and contraction percentage for each power are shown in Table 3.1. From the experimental data analysis, two single exponential functions have been used to fit the raise and the decay curve of the relative shift of the first diffraction order. The response times for these diffractive gratings fall in the millisecond time-scale. A power dependence can be recognized; in fact the deformation dynamics is faster if a higher activation power is employed. This effect can be explained because a higher number of photons forces a higher number of *trans-cis* transitions per unit of time and therefore the deformation speed increases. In principle, the higher excitation power the fastest the time evolution but the photobleaching effect occurs above a certain laser power. From Figure 3.10.a, we can notice that there is no delay from the laser switching time and the gradual shift of the diffracted beam but to complete the deformation a certain time is necessary. The two mechanisms that are responsible for the time response of the LCE structures are the heating mechanism and the light induced reduction of the nematic order of the liquid crystal monodomain (in

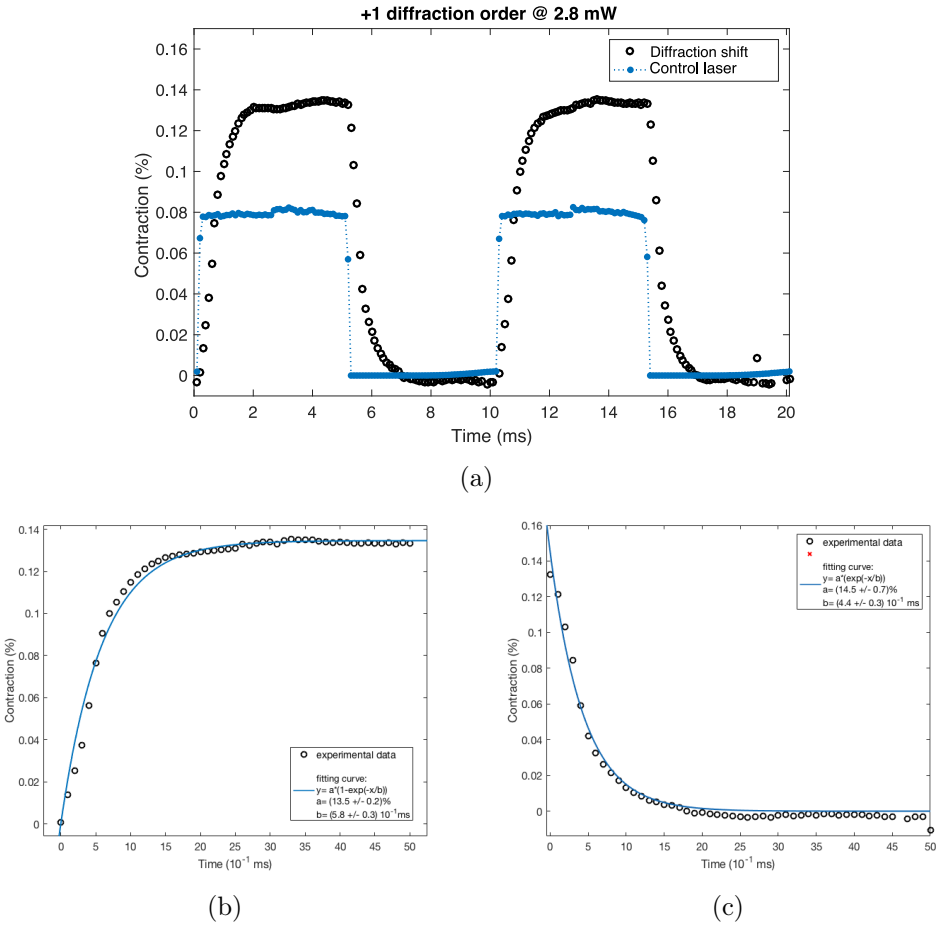

(a)

(b)

(c)

Fig. 3.10: (a) Temporal dynamics of the absolute diffractional order shift: (b) deformation time evolution (green laser "on") and (c) relaxation time (green laser "off").

well aligned structures) [30]. In this case, since the whole structure was placed under the green light spot, we assume that the structure thermalization time is negligible and the LC phase change plays the dominant role. For all the green laser actuation powers, this response time is in the order of millisecond, making our LCE device performance two orders of magnitude better than the other ones already described in literature [18–20]. The relaxation time instead does not show a significant trend depending on the green laser actuation power and assumes values around 4.5 ms. Also in this case a single decay exponential function fits the experimental data. We can then assume that the thermal relaxation time of such drilled LCE slab into air is about $4 - 5$ ms.

3.3 Guided mode resonance filter

For microstructured array with a slightly sub-wavelength periodicity, in the limit of $f \to 1$, GMR (guided mode resonance) effects have been predicted by Wang and Magnusson in [3, 31] through an approximate theoretical analysis. Using standard waveguide equations for weakly modulated diffraction gratings, a typical resonant feature has been demonstrated. When an incident optical wave is coupled by a grating to a leaky waveguide mode, supported by a thin-film system, pronounced resonance reflections can occur (guided-mode resonance, GMR) The principle of optical filtering using guided-mode resonance devices has therefore been applied to different applications not only as reflection and transmission filters [32, 33], laser mirrors [34], and biosensors [35], but also in the realization of nano-electro-mechanical display pixels [36], polarization-independent elements and reflectors for absorption enhancement in solar cells [37]. GMR structures are usually based on weak corrugations and are designed to act as narrow-band reflection filters typically on dielectric materials. Dielectric microstructure arrays, that employ transparent materials, show the feature of having a direct transmission pathway. Away from resonance, a nanostructured array behaves like a slab with an effective permittivity given by an average geometrical permittivity of its compounds. In the resonance vicinity, the direct pathway interacts with light re-emitted by the resonant structure, resulting in transmission spectra with Fano lineshapes [38] with a large contrast, as high as unit. The shape and size of the nanostructures have a strong impact on the resonance mechanism. When a plane electromagnetic wave is incident on the GMR filter at a wavelength for which there is no guided-mode resonance, the transmission and reflection spectra can be understood using conventional thin-film theory [33]. However, a guided wave can be excited if the incident light meets the Bragg diffraction condition. If we consider a 1D grating with a period d (the same geometry of the grating reported in Fig. 3.2), surrounded by air ($n = 1$) the Bragg condition assumes the form

$$k_0 \sin\theta \pm m\frac{2\pi}{d} = \beta \tag{3.3}$$

with m an integer number and β the propagation wave in the GMR layer structure. The grating structure creates a constructive interference in the reflected direction and a dip in the transmission spectra. With ideal, lossless materials, the bandwidth of a GMR filter can be reduced by simply decreasing the grating depth t_{gr} [39, 40]. As the grating depth decreases, the coupling loss of the leaky modes becomes weaker, resulting in a longer photon lifetime in the GMR structures and hence a narrower resonance

linewidth. Therefore for small modulation amplitudes, the resonance linewidths are narrow with high resonance Q factors. Increasing the modulation strength broadens the resonance peaks and reduces the local field amplitudes. The resonance wavenumber and the filter bandwidth of GMR filters all dependent on the structure parameters - referring to Figure 3.2 - such as grating depth t_{gr}, waveguide layer thicknesses t_{slab}, grating period d, and grating filling factor f .[2] Using a Matlab based implementation of the rigorous coupled wave analysis (RCWA) [41, 42], we looked for a parameter configuration, compatible with the fabrication constraints, which showed a quite sharp resonance in the telecommunication range. A typical finger print of the GMRF can be retrieved in the dispersion diagram since guided resonances will turn out to depend critically on their modal properties. In the dispersion diagrams for a unperturbed waveguide/slab, if the waveguide is single mode, one finds a unique linear relation between the wavevector k and the frequency ω, $k = k_g(\omega)$ (the presence of a cutoff frequency determines a lower frequency bound) [43]. The dispersion curve is always situated outside the cone defined by the light line, thus the guided mode cannot be excited by any incident light in this configuration. Modes below the light line are guided modes with infinite lifetime. The guided modes above the light line, on the other hand, can now couple to radiation modes and possess a finite lifetime. If periodicity is introduced, the dispersion curve thus evolves into branches of a Brillouin diagram, that represent the solutions $k = k_g = K$ for all reciprocal vectors $K = 2\pi n/d$ and k_g the wavevector of the in plane guided mode. In this case, some curves lie inside the light cone and the guided mode can be excited by a properly chosen incident plane wave whose x component of the wavevector satisfies $k_{inc} = k_g(\omega) - K$. The modifications of the dispersion relations induced by the presence of a small grating placed on top of the slab by means of a perturbative approach are reported in [44]. These modes therefore become guided resonances. They are called "guided" since they are closely related to the guided mode bands in a uniform slab and should therefore retain significant portions of the electromagnetic power within the dielectric slab. They are generated by a multiple scattering phenomena of each unit cell of the grating structure and this collective resonance are characterized by a strong angular dispersion. The result is that the dispersion curve for a resonant propagating mode is folded in the first Brillouin zone, with bandgaps at $k_x = 0, \pi/d, ...m\pi/d$ with m, an integer number [1].

3.3.1 LCE guided mode resonance filter

The first demonstration of a GMR filter fabricated with liquid crystalline elastomers is here reported. The 1D grating with a pitch periodicity of $d = 1.6\,\mu$m, a thickness $t_{gr} = 1\,\mu$m is fabricated on a LCE homogeneous slab with an height of $t_{slab} = 2.5\,\mu$m. The LCE alignment is parallel to the grating lines in such a way that, at the phase transition, the grating pitch increases. Depending on the light polarization, the resonance shift will exploit the refractive index change (from highly birefringent to a para-nematic state, Paragraph 2.2.3). To enhance the refractive index contrast of this dielectric structure, it has been positioned on LCE pedestal $5\,\mu$m far from the glass substrate. The

[2] The geometrical parameters chosen for our GMR slab are also influenced by fabrication limits due to the minimal and maximal thicknesses realizable with the DLW on liquid crystalline elastomeric mixtures.

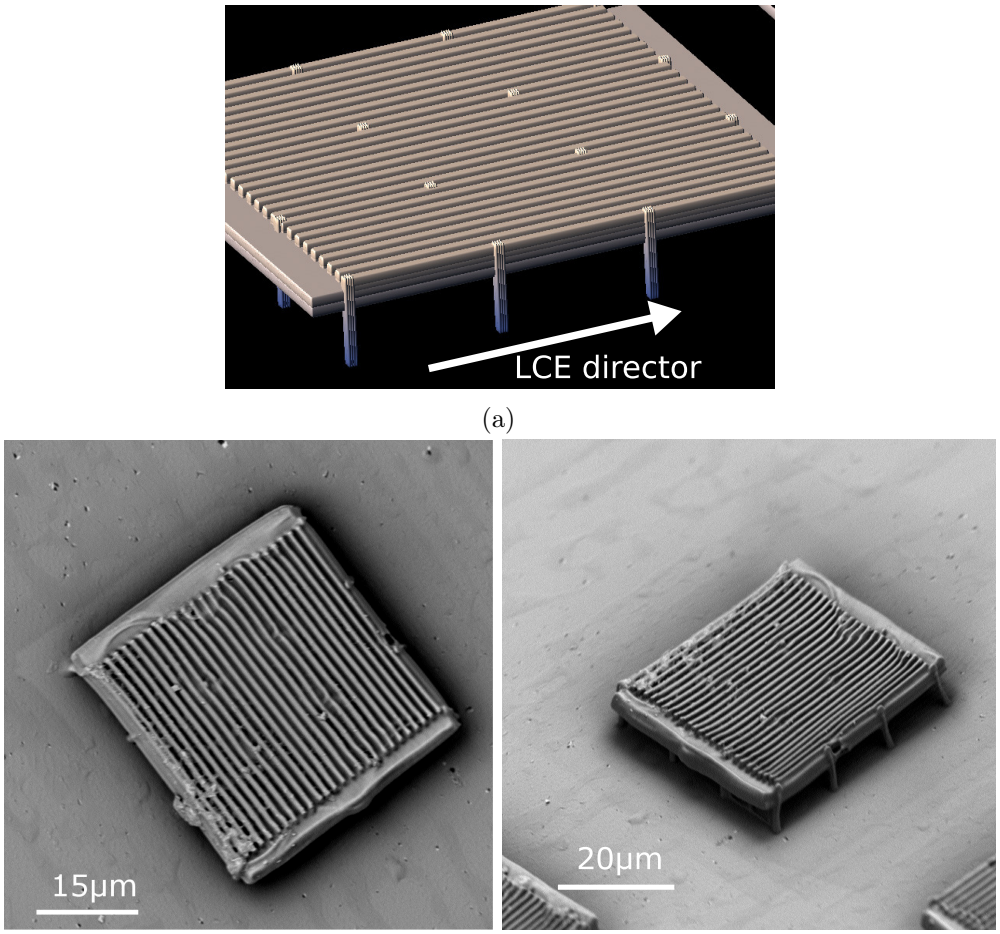

(a)

(b) (c)

Fig. 3.11: (a) 3D rendering of the grating structure. (b) and (c) SEM images of a GMRF.

refractive index contrast is not the only reason that motivates this choice; in fact, the LCE deformation of a thin slab (as the one that is constituting the grating waveguide layer), anchored to the glass substrate, is strongly limited by the strain introduced by the glass adhesion. In this case, only the upper part of the LCE device deforms in response to a determined stimulus, reducing also the maximum expansion/contraction. A quasi free-standing structure, laid on the LCE pedestal as shown in the SEM picture (Figure 3.11), is instead able to contract up to the 20% as demonstrated for the LCE beam steerer. These structures have been fabricated with the MM-30 LCE mixture, because of its better performance in the realization of suspended structures, in a glass cell with a uniaxial alignment with the DLW lithographic technique. The polymerization power and the distance in between the center of the guiding slab layer and the grating lines, are the paramenters that have been varied during the fabrication. Matrices of GMRF, with slightly different fabricational parameters are then present on glass substrates after the monomer development in hot (60°) 2-propanol [24].
The GMR filter optical response has been measured with the experimental setup whose

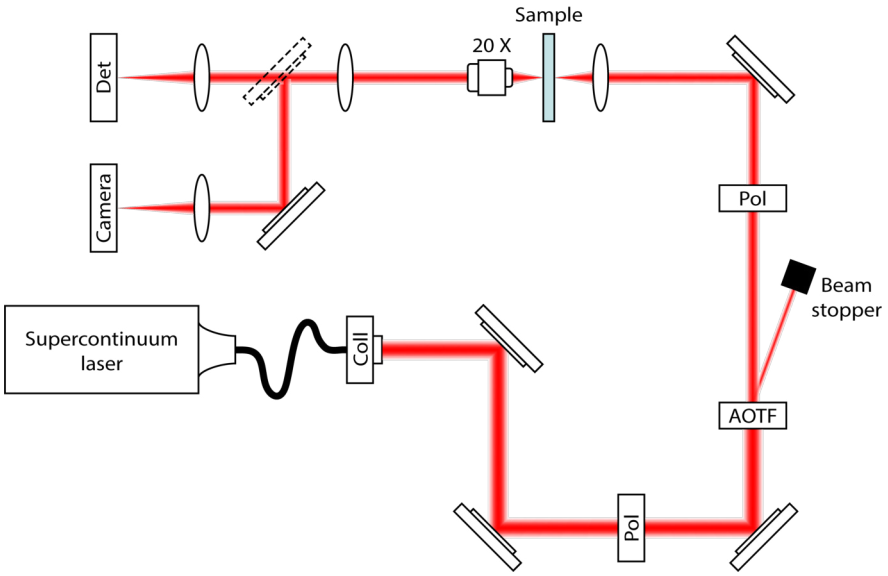

Fig. 3.12: Experimental setup for the optical characterization of GMRFs.

scheme is reported in Figure 3.12. The transmission spectroscopy setup is constituted by a super-continuum source (Fianium Whitelase supercontinuum laser SC-400-4) linearly polarized through a high damage threshold polarizing cube beam splitter. An acousto-optic tunable filter (AOTF) is used to rapidly and dynamically select a specific wavelength from the broadband laser source in the range from 1200 nm up to 2000 nm .[3] The quasi-monocromatic light is therefore focused on the sample with a lens doublet for the infrared with a focal length of 400 mm. The transmitted light is collected with a long working distance objective 20X (Mitutoyo Plan Apo NIR Infinity Corrected Objective). A flipping mirror allows to deviate the beam on a near-infrared camera (Indigo Phoenix) in order to individuate the grating to analyzed with a defocused laser light and put the focused spot in the middle of the chosen structure. Once aligned the sample, the grating transmitted light is collected by an InGaAs photo-diode (Hamamatsu- G12182). The optical characterization of different structures on the same substrate in order to find the best parameter combination underlines a measured filter transmission very different from the expected one. Moreover, due to the not high reproducibility of the fabrication method on soft materials, two nominally identical structures create different transmission spectra. In Figure 3.13, we compare the experimental transmission measured for TM incidence (see Fig. 3.2), and the theoretical response of the same nominal structure .[4] The theoretical prediction of the GMRF behavior has been evaluated with the RCWA software, previously introduced. Even if the optical features for the LCE real structures are very broad and the contrast far to be the 100% of the impinging intensity - as expected for the ideal case -, the first resonance at around 1600 nm is an evidence of the coupled light to the grating resonant mode. For the wavelength range under the

[3] As the applied RF frequency is varied, the transmitted wavelength changes, "tuning" the wavelength of the beam in tens of microseconds or less with resolution bandwidths of less than 1 nm.

[4] In this case, the refractive index that affects the electric field polarization component is the ordinary one and no material birefringence determines the structure features.

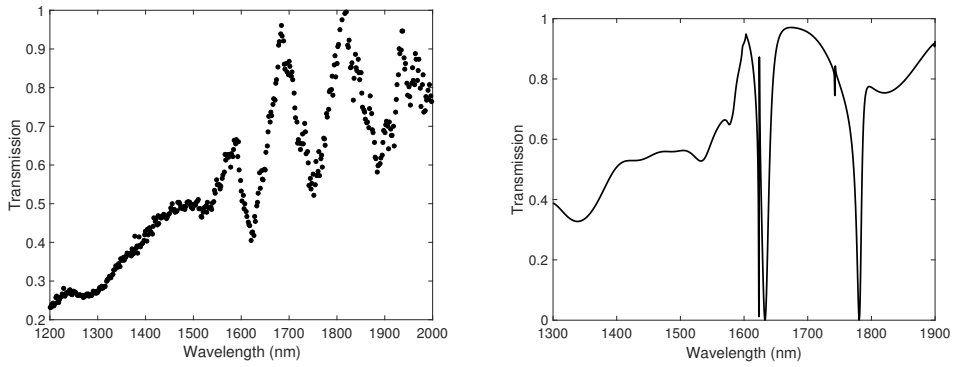

(a) (b)

Fig. 3.13: Transmission spectrum of a guided mode resonance filter with a periodicity d of 1.6 μm: (a) experimental results and (b) RCWA calculation results.

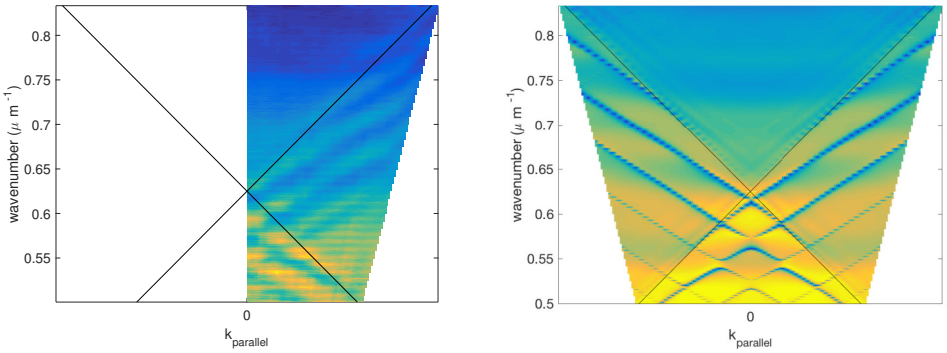

(a) (b)

Fig. 3.14: Dispersion diagram the TM polarization: (a) experimental results retrieved through angular spectroscopy; (b) calculated band dispersion for TM mode with RCWA.

laser wavelength, the grating behaves like a diffractive element and the transmission is modulated and less than the 100%.
Angular transmission $T(\lambda, \theta)$ spectra are measured for various incidence angles θ of an incident collimated beam with a small increment $\delta\theta$. For the evident difficulty to mode the beam direction, we decide to keep the optical axis unchanged and rotate the sample. This measurement requires then a not-banal rotational stage that allows to keep the rotation axis of the translation stage exactly in correspondence with the symmetry axis of the analyzed structure. With a coordinate transformation, they are translated into transmission $T(\omega, k)$ dispersion diagrams that is plotted in a color scale in Figure 3.14.a. The dispersion curves appear as bright or dark bands. The resonance width is related to the total decay rate of optical modes (temporal coherence) and intensity variations reflect both their free-space coupling and internal losses. To perform a comparison with calculated data, the same structure has been implemented in the

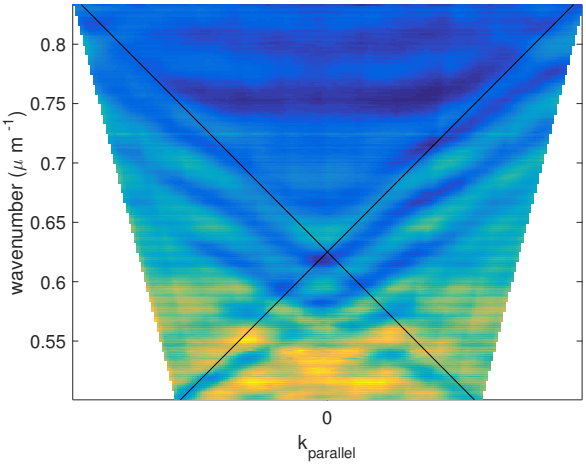

Fig. 3.15: Measured band dispersion for TE mode with RCWA.

RCWA software previously introduced. The geometrical parameters inserted in the calculation correspond to the effective dimension of the fabricated resonant grating. The refractive index has been set to 1.5 since the TM field component is affected only by the refractive index value of the ordinary component (it lies in the perpendicular plane to the LC director). The band diagram is reported in Figure 3.14.b. In both maps, we can distinguish, under the light line (in black), the guided mode resonances. Due some RCWA software limitations, the TE mode can not be evaluated. To have a complete experimental characterization of the band diagram, we repeated the angular transmission measurements for the TE component (Figure 3.15).
For these structure, the possibility to tune their optical properties, i.e. to generate a resonance shift, through an optical control has not been tested yet. We would like, however, to underline how the combination of this particular birefringent material - that can vary its refractive index depending on an external stimulus - and the presented grating geometry - that can increase or decrease its pitch distance depending on the LC alignment - can be opportunely considered to maximize the resonant shift. This characteristic is particularly interesting when the application is a tunable filter. In the described geometry, we report, in Figure 3.16, the spectra of a TM mode impinging on a grating deformable structure, still considering the alignment parallel to the grating lines. In these calculations, we introduce a parameter x that describes the "degree of contraction" and varies from 0 to 0.1 (10% contraction). In our model, the contraction along the alignment direction is followed by an expansion in the perpendicular plane and we assume that the both the grating pitch and the grating thickness increase following this expression

$$a(x) = a_0 \left(1 + \frac{x}{2}\right) \tag{3.4}$$

where a_0 represents both the grating pitch d, the grating t_{gr} and the slab t_{slab} thickness before the excitation. But as a consequence of the LCE transition, also the refractive index changes. For this alignment and polarization component choice,the dielectric

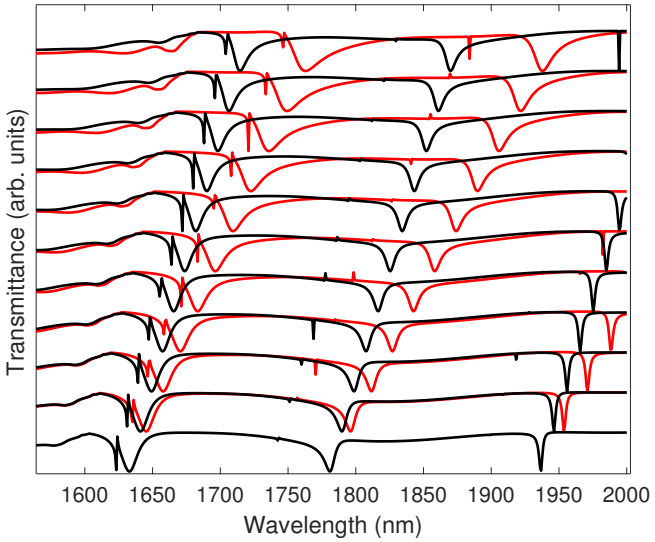

Fig. 3.16: Spectral resonant shift varying only the grating contraction (black curve) and considering also the refractive index variation (red curve). For TM polarization, the two effects sum together increasing the total shift.

permettivity increases. In particular, assuming an ordinary refractive index of 1.5 and an extraordinary one of 1.7, it depends on x parameter as

$$\epsilon(x) = \epsilon_0 \left(\frac{1.5 + (1.57 - 1.5)x}{x} \right)^2 \tag{3.5}$$

where 1.57 is the medium refractive index. In the graph, different "degree of contraction" in the interval are reported. The black curve is the transmission spectrum for a grating structure where only the geometrical reshaping is considered. The red curves consider also the refractive index variation. It is interesting how these two effect that happen simultaneously both contribute to increase the tuning of the resonant dips. The resulting effect exploits by the sum of the two and maximize the spectral shift.

References

[1] S. Collin. "Nanostructure arrays in free-space: optical properties and applications". In: *Reports on Progress in Physics* 77.12 (2014), p. 126402.

[2] K. Busch et al. "Periodic nanostructures for photonics". In: *Physics reports* 444.3 (2007), pp. 101–202.

[3] S. Wang and R. Magnusson. "Theory and applications of guided-mode resonance filters". In: *Applied optics* 32.14 (1993), pp. 2606–2613.

[4] S. Fan and J. Joannopoulos. "Analysis of guided resonances in photonic crystal slabs". In: *Physical Review B* 65.23 (2002), p. 235112.

[5] R. Gómez-Medina, M. Laroche, and J. J. Sáenz. "Extraordinary optical reflection from sub-wavelength cylinder arrays". In: *Optics Express* 14.9 (2006), pp. 3730–3737.

[6] A. W. Lohmann and D. Paris. "Binary Fraunhofer holograms, generated by computer". In: *Applied Optics* 6.10 (1967), pp. 1739–1748.

[7] J. R. Leger, D. Chen, and Z. Wang. "Diffractive optical element for mode shaping of a Nd: YAG laser". In: *Optics letters* 19.2 (1994), pp. 108–110.

[8] E. R. Dufresne and D. G. Grier. "Optical tweezer arrays and optical substrates created with diffractive optics". In: *Review of scientific instruments* 69.5 (1998), pp. 1974–1977.

[9] K. Hirabayashi, T. Yamamoto, and M. Yamaguchi. "Free-space optical interconnections with liquid-crystal microprism arrays". In: *Applied optics* 34.14 (1995), pp. 2571–2580.

[10] K. Hirabayashi and T. Kurokawa. "Liquid crystal devices for optical communication and information processing systems". In: *Liquid Crystals* 14.2 (1993), pp. 307–317.

[11] D. Faklis and G. M. Morris. "Diffractive optics technology for display applications". In: *IS&T/SPIE's Symposium on Electronic Imaging: Science & Technology*. International Society for Optics and Photonics. 1995, pp. 57–61.

[12] J.-J. P. Drolet et al. "Compact, integrated dynamic holographic memory with refreshed holograms". In: *Optics letters* 22.8 (1997), pp. 552–554.

[13] K. Van Acoleyen et al. "Off-chip beam steering with a one-dimensional optical phased array on silicon-on-insulator". In: *Optics letters* 34.9 (2009), pp. 1477–1479.

[14] V. V. Nikulin et al. "Modeling of an acousto-optic laser beam steering system intended for satellite communication". In: *Optical Engineering* 40.10 (2001), pp. 2208–2214.

[15] S. Schauer et al. "Tunable Diffractive Optical Elements Based on Shape-Memory Polymers Fabricated via Hot Embossing". In: *ACS applied materials & interfaces* 8.14 (2016), pp. 9423–9430.

[16] J. Kim et al. "Wide-angle, nonmechanical beam steering using thin liquid crystal polarization gratings". In: *Proc. SPIE*. Vol. 7093. 2008, p. 709302.

[17] H.-C. Jau et al. "Optically-tunable beam steering grating based on azobenzene doped cholesteric liquid crystal". In: *Optics express* 18.16 (2010), pp. 17498–17503.

[18] H.-C. Jau et al. "Light-Driven Wide-Range Nonmechanical Beam Steering and Spectrum Scanning Based on a Self-Organized Liquid Crystal Grating Enabled by a Chiral Molecular Switch". In: *Advanced Optical Materials* 3.2 (2015), pp. 166–170.

[19] Q. Li et al. "Directing Dynamic Control of Red, Green, and Blue Reflection Enabled by a Light-Driven Self-Organized Helical Superstructure". In: *Advanced Materials* 23.43 (2011), pp. 5069–5073.

[20] Z.-g. Zheng et al. "Three-dimensional control of the helical axis of a chiral nematic liquid crystal by light". In: *Nature* 531.7594 (2016), pp. 352–356.

[21] M. Devetak et al. "Micropatterning of light-sensitive liquid-crystal elastomers". In: *Physical Review E* 80.5 (2009), p. 050701.

[22] M. Gregorc et al. "Kinetics of holographic recording and spontaneous erasure processes in light-sensitive liquid crystal elastomers". In: *Materials* 5.5 (2012), pp. 741–753.

[23] B. Tašič et al. "Light-Induced Refractive Index Modulation in Photoactive Liquid-Crystalline Elastomers". In: *Macromolecular Chemistry and Physics* 214.23 (2013), pp. 2744–2751.

[24] S. Nocentini et al. "Photoresist Design for Elastomeric Light Tunable Photonic Devices". In: *Materials* 9.7 (2016), p. 525.

[25] H. Shahsavan et al. "Smart Muscle-Driven Self-Cleaning of Biomimetic Microstructures from Liquid Crystal Elastomers". In: *Advanced Materials* 27.43 (2015), pp. 6828–6833.

[26] D. Liu and D. J. Broer. "Liquid crystal polymer networks: preparation, properties, and applications of films with patterned molecular alignment". In: *Langmuir* 30.45 (2014), pp. 13499–13509.

[27] M. Nakanishi et al. "Ultraviolet photobleaching process of azo dye doped polymer and silica films for fabrication of nonlinear optical waveguides". In: *Applied optics* 37.6 (1998), pp. 1068–1073.

[28] J. Vydra et al. "Photodecay mechanisms in side chain nonlinear optical polymethacrylates". In: *Applied physics letters* 69.8 (1996), pp. 1035–1037.

[29] M. Pellatt, I. Roe, and J. Constant. "Photostable anthraquinone pleochroic dyes". In: *Molecular Crystals and Liquid Crystals* 59.3-4 (1980), pp. 299–316.

[30] N. J. Dawson et al. "Cascading of liquid crystal elastomer photomechanical optical devices". In: *Optics Communications* 284.4 (2011), pp. 991–993.

[31] R. Magnusson and S. Wang. "New principle for optical filters". In: *Applied physics letters* 61.9 (1992), pp. 1022–1024.

[32] S. Tibuleac and R. Magnusson. "Narrow-linewidth bandpass filters with diffractive thin-film layers". In: *Optics letters* 26.9 (2001), pp. 584–586.

[33] S. Wang and R. Magnusson. "Design of waveguide-grating filters with symmetrical line shapes and low sidebands". In: *Optics letters* 19.12 (1994), pp. 919–921.

[34] R. Magnusson, P. P. Young, and D. Shin. *Vertical-cavity laser and laser array incorporating guided-mode resonance effects and method for making the same.* US Patent 6,154,480. Nov. 2000.

[35] D. D. Wawro et al. "Optical fiber endface biosensor based on resonances in dielectric waveguide gratings". In: *BiOS 2000 The International Symposium on Biomedical Optics*. International Society for Optics and Photonics. 2000, pp. 86–94.

[36] R. Magnusson and M. Shokooh-Saremi. "Widely tunable guided-mode resonance nanoelectromechanical RGB pixels". In: *Optics express* 15.17 (2007), pp. 10903–10910.

[37] T. Khaleque, H. G. Svavarsson, and R. Magnusson. "Fabrication of resonant patterns using thermal nano-imprint lithography for thin-film photovoltaic applications". In: *Optics express* 21.104 (2013), A631–A641.

[38] A. E. Miroshnichenko, S. Flach, and Y. S. Kivshar. "Fano resonances in nanoscale structures". In: *Reviews of Modern Physics* 82.3 (2010), p. 2257.

[39] W. Liu et al. "Guided-mode resonance filters with shallow grating". In: *Optics letters* 35.6 (2010), pp. 865–867.

[40] J.-N. Liu et al. "Optimally designed narrowband guided-mode resonance reflectance filters for mid-infrared spectroscopy". In: *Optics express* 19.24 (2011), pp. 24182–24197.

[41] S. Zanotto. *PPML - Periodically Patterned Multi Layer*. 2016. URL: `https://it.mathworks.com/matlabcentral/fileexchange/55401-ppml-periodically-patterned-multi-layer`.

[42] S. Zanotto et al. "Intersubband polaritons in a one-dimensional surface plasmon photonic crystal". In: *Applied Physics Letters* 97.23 (2010), p. 231123.

[43] E. Hecht and A. Zajac. *Optics*. Addison-Wesley publishing company, 1974.

[44] F. Lemarchand et al. "Study of the resonant behaviour of waveguide gratings: increasing the angular tolerance of guided-mode filters". In: *Journal of Optics A: Pure and Applied Optics* 1.4 (1999), p. 545.

CHAPTER 4

Ring resonators as polymeric passive cavities

Nanophotonic integrated circuits allow to achieve complex optical functionality by assembling many individual devices into fullscale systems. The fundamental element of signal transport and manipulation is the waveguide, that, for its non trivial features, can be defined itself as the simplest device that can be integrated on a chip. Combining different waveguides geometries, interferometers and beam splitters can be realized. More circuit functionalities are conveyed by the whispering gallery mode resonator (WGMR) introduction. They create a widespread interest in many different fields in optical communication as filters and sensors, or in cavity quantum electro-dynamics studies due to their peculiar property of sharp resonances, highly sensitive to the external environment. Due to their small mode volume and compact shape, they are easily employed on integrated chips in many configurations and applications. Here, the study and the fabrication have been focused on a basic polymeric structure integrated on a glass substrate. It is constituted by a single mode waveguide for the near-infrared vertically coupled to a WGMR. This quite simple dielectric integrated structure is a basic element of more complex integrated circuit and it is characterized by high stability. Furthermore the three-dimensional lithographic technique of direct laser writing allow the possibility to integrate, on different kind of substrates, different polymeric and functionalized materials.
Through a spectral analysis of the waveguide transmitted light, the photonic properties of different kind of cavities have been measured. For a polymeric micro-ring resonator, the highest quality factor measured in this work is 80000.

4.1 Polymeric single mode waveguide

Before digging into the central topic of this chapter, the whispering gallery mode resonators, a brief introduction about polymeric waveguides is developed. As the

most simple and important circuit element on an optical chip, they represent such a fundamental and delicate (at the same time) brick of this work.
The theory of light propagation into waveguides is exhaustively treated in many books and articles [1–4] and starting from the Maxwell equations and wave equation in a dielectric medium, the field confined inside a linear waveguide can be describes as a propagating mode. If we consider a system of coordinates with the z axis parallel to the guide axis, the characteristics of a waveguide are determined by the transverse profile of its dielectric constant $\epsilon(x,y)/\epsilon_0$, which is independent of the longitudinal (z) direction. The dielectric waveguide permettivity can be therefore described as:

$$\epsilon(x,y) = \epsilon_0 n^2(x,y) \tag{4.1}$$

with ϵ_0 the vacuum permettivity. The function $n(x,y)$ is the refractive index profile for a non-planar waveguide made of an isotropic medium (in a planar waveguide the optical confinement is only in one direction and the refractive index dependence is $n(x)$). One distinctive property of non-planar dielectric waveguides versus planar waveguides is that a nonplanar waveguide supports hybrid modes in addition to TE and TM modes, whereas a planar waveguide supports only TE and TM modes.
A waveguide mode, the transverse field pattern, is defined as a field solution of the form

$$\begin{aligned} \vec{E}(x,y,z,t) &= \vec{E}_\nu(x,y)exp(-j\beta_\nu z - \omega t), \\ \vec{H}(x,y,z,t) &= \vec{H}_\nu(x,y)exp(-j\beta_\nu z - \omega t), \end{aligned} \tag{4.2}$$

where ν is a mode label (indicating the mode number), and β_ν is the propagation constant of the mode. Inserting the modal fields of Eq. 4.2 into Maxwell's equations, we obtain a complete system that can be solved for each vectorial field component, as discussed in detail in [5]. The resulting solutions for dielectric waveguides, are guided modes (bound states), where the energy is confined near the axis, and radiation modes (unbound states) with their energy spread out through the medium surrounding the guide. The guided modes are associated with a discrete spectrum of propagation constants β_ν, while the radiation modes belong to a continuum. The discrete solutions correspond to the fundamental mode ($\beta_\nu = 0$) and to the higher modes ($\beta_\nu = 1, 2...$). There is a cut off wavelength determined by the geometrical dimensions but that for dielectric waveguides does not have an analytic expression. Other solutions are the evanescent modes that have an imaginary propagation constant $\beta_\nu = -j\alpha_\nu$ which decay as $exp(-\alpha_\nu z)$.
The exact solution has been exactly derived for planar waveguide [6] but no analytic solution is available for ridge waveguides. However it has been shown that approximated solutions can be retrieved applying specific simplifications [7]. Except for those few exhibiting special geometric structures, such as circular optical fibers, non-planar dielectric waveguides generally do not have analytical solutions for their guided mode characteristics. In these cases numerical methods, such as the beam propagation method, are typically used for analyzing such waveguides. In this work, we use a finite element method based software to, first of all, design the photonic structures, and once individuated the right geometrical parameters, to calculate the electric field distribution inside the dielectric structures.
A key parameter in guided propagation is the effective refractive index n_{eff}. It assumes

different value for the different guided modes and it can be defined as the ratio of the propagation constant in the waveguide β and the wavenumber of the electric field in the vacuum k_0,

$$n_{eff} = \beta/k_0 = c/v_{phase} = c\beta/\omega \tag{4.3}$$

with the introduction of the phase velocity $v_{phase} = \omega/\beta$.
Polymer based waveguides have the advantages respect to traditional silicon components to be easily integrated on other platforms and especially to be chemically modified (chemical synthesis of functionalized monomers) in order to introduce some new properties to active elements. On the other side, they suffer of low refractive index and the field confinement is reduced. However with respect to traditional optical fibers, on chip integrated polymer waveguides offer a stable and not fragile light transport device. At the same time, they introduce the possibility to split the signal in different branches (directional coupler), to create delay lines or to filter the signal trough ring resonator cavities.

4.1.1 Grating coupler

The light can be easily transferred and manipulated by a system of integrated polymer devices; but how to couple the light from an optical fiber or a free space optic setup into a photonic chip remains a critical problem. Optical prisms [8] or side-polished optical fibers [9] can be used but they require a high precision position control. A different strategy is constituted by grating couplers. In this case, after a proper design of the coupling element to improve the grating performance, they demand high resolution nanofabrication technologies, as e-beam lithography or laser writing techniques, to achieve coupling efficiencies [10]. Grating couplers are also mode-sensitive because their efficiency depends on the effective grating index [11]. Therefore either the TE or TM modes can be selectively excited using a suitably designed input coupler. Moreover, the maximum of the coupling efficiency can easily be shifted spectrally by adjusting the grating period. Exploiting the latter two aspects, grating couplers can couple the incident light to either the TE-like or the TM-like waveguide mode more efficiently in the investigated wavelength regime. To increase the efficiency, different strategy can be adopted. First of all, it has been demonstrated [10] that the beam incident angle that creates the best phase matching conditions is near to vertical coupling (at less 10° but not at normal incidence to avoid the grating reflection). From the geometrical point of view, instead, grating efficiencies can be improved both varying the coupling strength of the grating coupler with a variable groove depth or apodized geometries [12]. Other strategies employ gold mirrors [13] or distributed Bragg reflectors (DBR) [14, 15] to reflect upwards the light radiating towards the substrate. Light collection into the waveguide can be also increased implementing focusing gratings [13, 16].

4.1.2 Direct laser written polymeric waveguides

The DLW has been chosen to fabricate optical waveguides from photosensitive polymers being maskless and allowing rapid and low cost fabrication process respect to the other conventional UV photo-lithographic systems. Moreover, the possibility to achieve the

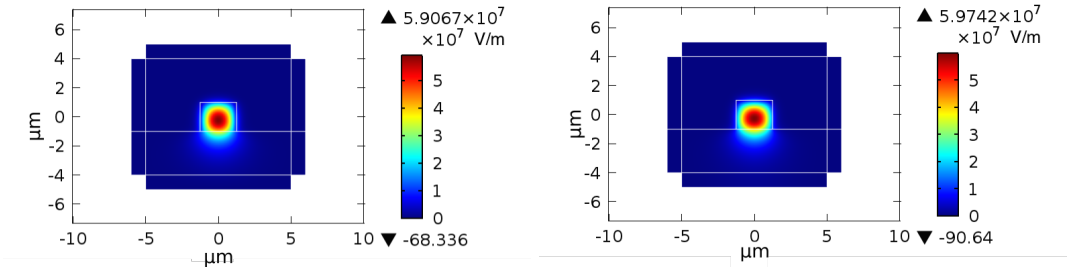

(a) (b)

Fig. 4.1: Electric field distribution for a polymer waveguide on a fused silica substrate: (a) TE mode, (b)TM mode.

third dimension, opens to a higher chip integration and more complex geometries that we exploited also in this work.
Through a two photon photo-polymerization of the commercial polymer Ip-Dip (Nanoscribe GmbH), polymeric single mode waveguides have been realized for the near infrared range. The waveguide core is directly placed on a fused silica glass cover slip with a refractive index of 1.444 at 1550 nm. The choice of such a low refractive index substrate material is motivated to achieve the mode confinement inside the waveguide. In fact, in this way a rectangular ridge waveguide of 2.5 μm width and 2 μm height guarantees the realization of a low refractive index contrast (1.52 over 1.444) single mode waveguide. A finite element method based software has been used to realize the waveguide mode analysis. In Figure 4.1, the electric field distribution for the TE and TM mode are reported. From these calculations, for a polymeric waveguide on glass substrate, we can point out the effective refractive index for the two fundamental modes: for the TE mode n_{eff} is 1.493; for the TM mode is 1.494.
To inject the light into the waveguide, and at the same time to extract the device transmission at the other end, an input and output grating couplers are employed. Once evaluated the effective refractive index of the propagating mode, we used a 2D FEM calculation to find out the grating coupler parameters. The initial parameters of the FEM calculations where individuated from the diffraction law, that for a normal impinging beam (the angle θ in between the orthogonal direction to the grating and the incident k-vector is zero), becomes:

$$2\pi m/d = \beta_m \tag{4.4}$$

where d is the grating pitch and m an integer mode number that defines the order of the propagating mode. But d is not the only quantity that defines the grating geometry. In fact, a determinant role is played from the filling ratio f of dielectric material respect to air for each pitch and from the grating depth, that contributes with f to the grating effective refractive index determination. For this reason, a FEM 2D calculations were necessary to determine all the geometrical quantities. Through parameter sweeps (implemented in the program and not reported here), many configurations have been tested and the best one has been used for the structure fabrication. However the coupling efficiency is pretty low as it could be expected for structures with a low

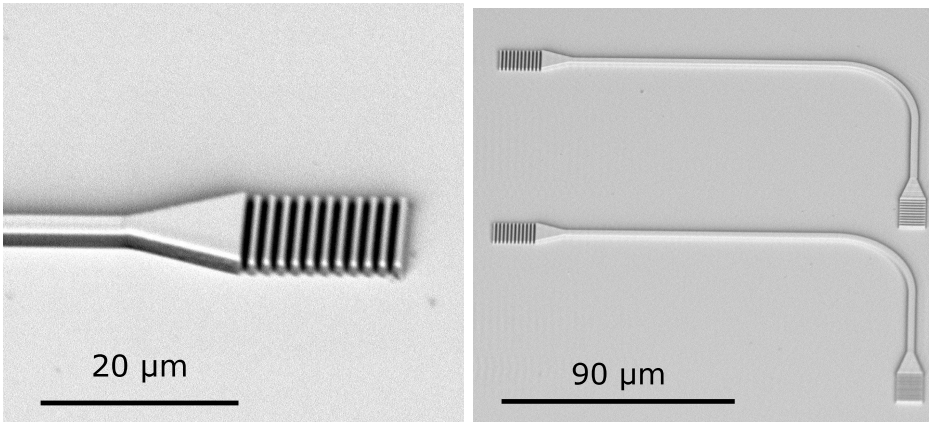

(a) (b)

Fig. 4.2: SEM images of the (a) grating coupler annd (b) two single mode polymeric waveguides.

refractive index contrast and at normal incidence. We are in fact considering a polymer waveguide with an effective refractive index of 1.49 over a dielectric substrate with a 1.444 refractive index. This contrast makes difficult to overcome a 3% coupling efficiency. In literature, for dielectric waveguides, values under the 10% have been reached but for higher refractive index contrast waveguides (for Si_3N_4 waveguides the contrast is 0.5, $n_{Si_3N_4} = 1.95, \quad n_{SiO_2} = 1.45$) [16]. Due to the waveguide geometry and the fabrication process, it is difficult to improve the efficiency adding DBR or a gold layer at the glass-polymer interface. We chose to realize a grating pattern that could contain the beam spot, 10 μm width (bigger that the waveguide), and followed by an in-plane taper to couple to the single-mode waveguide (Figure 4.2.a). The output grating is equal to the input one. In order to measure the waveguide transmission, avoiding the scattering background, 90° bent waveguides have been fabricated and the detection measurement has been done in a cross-polarization configuration. We chose TE polarization for the impinging beam, the polarization vector changes direction along the waveguide and we detect the waveguide outcoupled light selecting a polarization component rotated of 90°. In this way, we eliminate each field component that is not perpendicular to the incoming one. This choice revealed to be fundamental because of the low grating efficiencies.

4.2 Whispering gallery mode resonators

Resonant phenomena in cavities, be they acoustic, optical, mechanical, or otherwise, are frequently dependent on the precise geometric properties, such as size, shape, and composition, of the supporting structure. In fact, these are very sensitive characteristics that should be carefully designed by proper calculations and then determined during the lithographic process. The main characteristic of WGMR is the presence of a traveling wave at the rim of a cylindric symmetric cavity. Optical microcavities are used to confine light both spatially and temporally. Light within the sphere is confined by continuous total internal reflection near the cavity perimeter, and the modes have therefore been called "whispering-gallery" modes (definition introduced by Lord Rayleigh describing the

phenomenon of acoustical wave he had noticed propagating along the interior gallery of Saint Paul's Cathedral [17]). From a geometric perspective, such bound modes are guided by means of repeated reflections, which, neglecting absorption, scattering, and material dispersion, continue ad infinitum. Within a wave description, however, losses through the surface are present via tunneling or frustration, such that the mode, in the absence of an external excitation, experiences a decay in its amplitude bringing it to a finite lifetime. Exploiting one of their peculiar characteristic as the high intensity confined field or its evanescent tail, they have been employed in low threshold lasing [18, 19], highly sensitive sensing [20, 21], nonlinear optics [22, 23], , cavity quantum electrodynamics [24, 25], and optomechanics [26, 27]. A plethora of alternative geometries, such as toroidal, goblet, tubular (including capillary and bottleneck resonators), and microbubble resonators, also exist, each with their own set of relative merits [28–33]. Larger refractive index contrasts between the cavity and the host therefore help to minimize radiative losses via stronger confinement of the WGMs but making them more sensitive to each structural defect. Conversely, a low refractive index contrast facilitates extension of the mode profile beyond the edges of the resonator, thus potentially increasing the WGMR sensitivity as sensor.
Whispering gallery mode theory has been studied following different approaches [34, 35] but here I would like to report the principal optical cavity features without a complete derivation. WGM resonances occur when the light wavelength λ is contained an integer number m (azimuthal mode number) of times inside the cavity - for total internal reflection at the rim of the resonator - of radius R and effective refractive index n_{eff}:

$$m\lambda = 2\pi R n_{eff}. \tag{4.5}$$

A scheme of a WGM in a symmetric axis cavity is shown in Figure 4.3. The spatial and temporal confinement depend on the geometry, the material, and the roughness of the dielectric structure.
A quantity strongly dependent from the microcavity geometry is the free spectral range, FSR. The FSR describes the spectral distance between consecutive azimuthal modes (m and $m+1$) with the same m_ρ and m_z mode numbers, where m_ρ and m_z denote the number of maxima minus one of the energy density in radial and vertical direction respectively (see Fig.4.3). The FSR of WGMS can be calculated from equation Eq. 4.5 and is given by:

$$FSR = \frac{\lambda_0^2}{2\pi R n_{eff} + \lambda_0} \approx \frac{\lambda_0^2}{2\pi R n_{eff}}. \tag{4.6}$$

The approximation in the last step is valid for $R \gg \lambda_0$ and is therefore valid for the cavities investigated in this work. Values for the FSR of optical microcavities in the visible/NIR spectral range are typically in between 1 nm and tens of nanometers. Not only connected with the cavity geometry, the cavity quality factor, Q, is one of the most important features to define the resonator quality. It indicates the energy storage ability of the microcavity. In fact, due to the presence of loss mechanisms such as material absorption, scattering losses or tunnel losses, the optical modes of a resonator are dissipative. The extent to which dissipation is present in a resonant system is

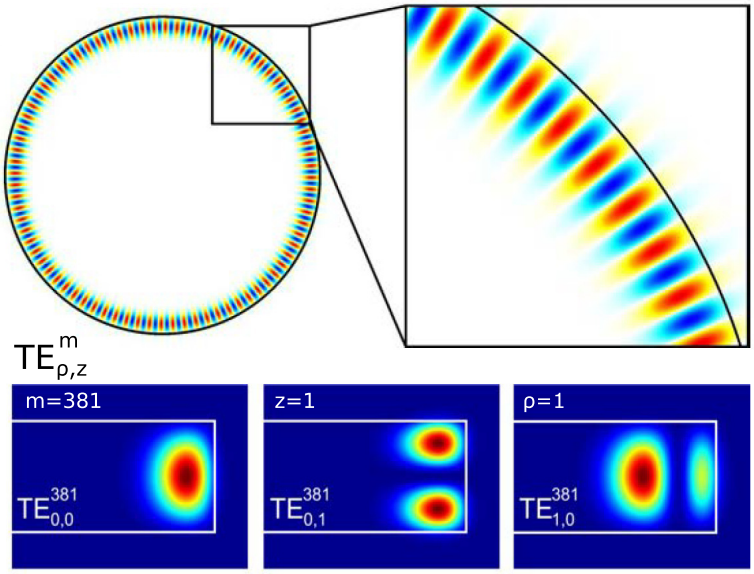

Fig. 4.3: A disk resonator with the electric field intensity distribution for a WGM. Below a schematic description of the mode number definition is reported. The maps show the electrical density calculated with an axial mode analysis.

expressed by the quality factor, which is then defined as:

$$Q = \omega_0 \frac{U_{stored}}{P_{diss}} = \omega_0 \tau \tag{4.7}$$

In this equation ω_0 is the resonance frequency, U_{stored} is the energy contained in the resonant system, and P_{diss} is the dissipated power and it defines the cavity ring-down lifetime τ. To the total amount of losses that determine the energy dissipation, different contributes can be distinguished. The three main intrinsic loss mechanisms are absorption (Q_{abs}), radiation (Q_{rad}) and surface scattering (Q_{scatt}) as well as an extrinsic loss (Q_{ext}). This last contribute occurs only when light is coupled into the resonator by an external coupler, such as a tapered optical

fiber or a prism, and therefore can also be dissipation via this channel. The total Q-factor can then be expressed by the Q-factors resulting from these individual loss mechanisms via

$$\begin{aligned} \frac{1}{Q} &= \frac{1}{Q_{abs}} + \frac{1}{Q_{rad}} + \frac{1}{Q_{scatt}} + \frac{1}{Q_{ext}} \\ &= \frac{1}{Q_{int}} + \frac{1}{Q_{ext}}. \end{aligned} \tag{4.8}$$

The intrinsic loss mechanisms are summarized in the intrinsic Q-factor, Q_{int} with $Q_{int}^{-1} = Q_{rad}^{-1} + Q_{rad}^{-1} + Q_{scatt}^{-1}$. The polymers, used in this work for the cavity fabrication, due to the very small absorption coefficient of Ip-Dip (commercial polymer used for the cavity fabrication with the DLW technique) in the NIR range, are ideal polymers for the microresonator and the absorption losses give the smallest contribute to the energy

dissipation. A small fraction of the energy of the modes is inevitably lost by radiation due to the curve surface of WGM resonators. But, after a radius choice that limits radiation losses, also this contribute can be considered negligible. The main actor in Q factor degradation is scattering. Imperfections along the dielectric cavity interface cause surface-scattering losses. Especially in lithographically structured microcavities, surface scattering is the dominating loss mechanism due to cavity roughness. However all these effects can be mitigated giving rise to very high quality factor up to $Q = 10^8 - 10^9$ [28, 36].
The last physical quantity that will be introduced is the whyspering gallery mode volume, V.

$$V = \frac{Tot.Energy}{max(Energy\ Density)} \tag{4.9}$$

The mode volume is an important parameter for microlasers (see Chapter 5) as both the spontaneous and stimulated emission rates are proportional to $1/V$ and the lasing threshold is proportional to V [37]. WGM microcavities usually provide small mode volumes so that they are desirable candidates for microlasers.
The simplest configuration to exploit and investigate the WGM resonator properties is a unidirectional coupling through a fiber or a waveguide. In both cases, the output is affected by the cavity properties and we can retrieve the spectral dependence starting from the Q definition in Eq. 4.7. From this equation, remembering that $U_{stored} = U$ (for simplicity) is the energy stored in the cavity, results

$$Q = \omega_0 \frac{U}{-\frac{dU}{dt}}. \tag{4.10}$$

We can then reconstruct the time dependence:

$$U(t) = U(t = 0)e^{-\omega_0 t/Q}. \tag{4.11}$$

This equation shows that the cavity Q-factor can be directly determined by measuring the temporal decay of the energy in so-called cavity-ringdown measurements [28]. This type of measurement is difficult to perform experimentally. An alternative and more practical way to determine the Q-factor is the measurement of the resonance linewidth in the frequency domain. This approach is derived and discussed in the following. Due to the relation $U(t) = u(t)^2$, the time dependency of the electric

field u is given by:

$$u(t) = u_0 e^{-\omega_0 t/2Q} e^{-i\omega_0 t}. \tag{4.12}$$

Fourier transformation of equation Eq. 4.12 results in the Lorentzian-shaped intensity I distribution of the resonance

$$I(\omega) \propto \frac{1}{(\omega - \omega_0)^2 + (\omega_0/2Q)^2} \tag{4.13}$$

This Lorentzian lineshape has a full width at half maximum of $\delta\omega = \omega_0/Q$. The Q-factor

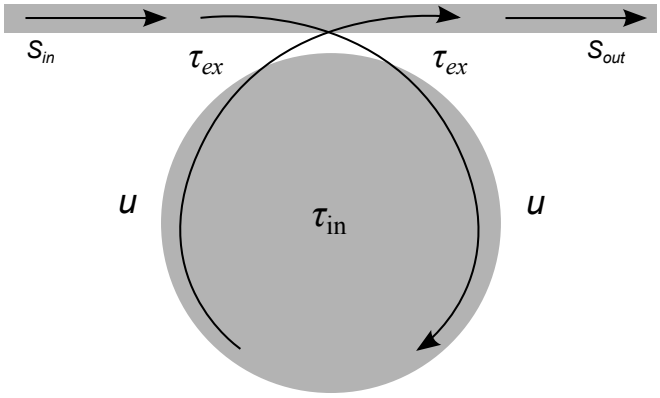

Fig. 4.4: Scheme of waveguide-resonator coupling. A fraction of the power of the waveguide mode s_{in} is coupled in the resonator mode u. The transmitted signal s_{out} is a superposition of the transmitted part of s and the fraction of u, which is coupled back from the resonator into the waveguide.

can be therefore experimentally determined as:

$$Q = \frac{\omega_0}{\delta\omega} \approx \frac{\lambda}{\delta\lambda} \tag{4.14}$$

and can thus be directly inferred from the linewidth of the resonance.

WGM resonator-waveguide coupling

Whispering-gallery-mode (WGM) resonances correspond to light trapped in circling orbits just within the surface of the particle, being continuously totally internally reflected from the surface. A crucial point of these studies is that light has to be coupled into and out of the cavity. If the evanescent field of the fiber is brought in the proximity of a microcavity -such as a microsphere, microdisk or microtoroid cavity-, the fundamental optical mode will exhibit overlapping with the whispering-gallery type modes of the microcavity. The coupling from a resonator to a waveguide is fundamentally described by three parameters, the resonant frequency ω_0, the decay rate $1/\tau_{int} = Q_{int}$ of the mode due to internal cavity losses, and the cavity decay rate $1/\tau_{ext} = Q_{ext}$ due to coupling to the waveguide mode. The input signal field s_{in} is coupled to the resonator mode (whose amplitude is noted as u) with a characteristic lifetime τ_{ext}. The light trapped inside the resonator can escape from the cavity (Fig. 4.4): through radiative or absorptive processes with a characteristic duration τ_{int} and through back coupling to the output field s_{out} in the access line, still with a characteristic duration τ_{ext}. Using the coupled mode theory (CMT) [38] the dynamic evolution of the system can be calculated by integrating

$$\frac{du}{dt} = i\omega_0 u - \left(\frac{1}{2\tau_{int}} + \frac{1}{2\tau_{ext}}\right) u + \kappa s \tag{4.15}$$

where u is still the resonator mode and s the waveguide mode .[1] The coupling coefficient is designated as κ and can be expressed by τ_{ext} using time reversal symmetry [38]: $\kappa^2 = 1/\tau_{ext}$. In the stationary regime at the angular frequency ω, the input field can be written $s = s_0 e^{(i\omega t)}$ and

$$s_{out} = -s_{in} + \sqrt{\frac{2}{\tau_{ext}}} u(t). \tag{4.16}$$

Inserting the mode expression of s inside Eq. 4.15, we obtain

$$u = \frac{\kappa u}{i(\omega - \omega_0) + (2\tau_{int})^{-1} + (2\tau_{ext})^{-1}} \tag{4.17}$$

The transmitted

field s_{out} in the waveguide is a superposition of the transmitted waveguide mode and the fraction of u, which is coupled back from the resonator into the waveguide. Using the conservation law and combining Eq. 4.16 and Eq. 4.17, we can define the linear transfer function $x(\omega)$

$$x(\omega) = \frac{s_{out}(t)}{s_{in}} = \sqrt{T} \exp j\phi = \frac{\tau_{ext}^{-1} - \tau_{int}^{-1} + j(\omega - \omega_0)}{\tau_{ext}^{-1} + \tau_{int}^{-1} + j(\omega - \omega_0)} \tag{4.18}$$

where T is the intensity transfer function and ϕ is the phase shift introduced by the system. The intensity transmission spectrum $T =\mid x \mid^2$ thus reads

$$T(\omega) = \frac{(\tau_{ext}^{-1} - \tau_{int}^{-1})^2 + (\omega - \omega_0)^2}{(\tau_{ext}^{-1} + \tau_{int}^{-1})^2 + (\omega - \omega_0)^2}. \tag{4.19}$$

The transmission properties are commonly characterized by over-coupled, critically coupled and under-coupled. Under-coupling refers to the case where the waveguide coupling is weak and the cavity decay rate τ_{int}^{-1} exceeds the cavity coupling rate τ_{ext}^{-1}. In this case the amplitude of the cavity leakage field $u/(2\tau_{int})$ is much smaller than the amplitude of the transmitted waveguide field. The cavity leakage field exhibits a phase shift of $\pi > \phi > 0$. In the over-coupled regime, instead, the rate of cavity coupling exceeds the cavity decay rate, $\tau_{ext}^{-1} > \tau_{int}^{-1}$. The amplitude of the cavity decay field in this case is larger than transmitted pump field, and reaches a value of twice the waveguide amplitude in the case of strong over-coupling. But the most interesting case in optics is the critical coupling. Critical coupling occurs when the external lifetime is matched to the intrinsic cavity decay rate $\tau_{ext}^{-1} = \tau_{int}^{-1}$. In this case the transmission after the resonator ideally vanishes, and a complete power transfer of the optical power, carried by the wave to the cavity mode, occurs. The signal s_{out} vanishes due to the interference of the cavity leakage field and transmitted pump field, which exhibit equal magnitude but a relative phase shift π [34].

[1] The quantities u and s have different units: $\mid u \mid^2$ is a normalized energy and $\mid s \mid^2$ is a normalized power.

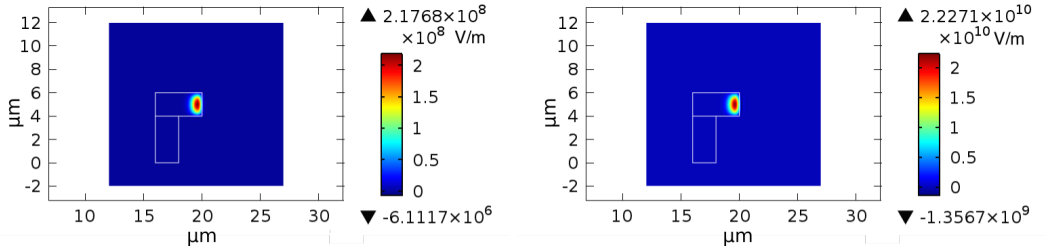

(a) TE mode. (b) TM mode.

Fig. 4.5: FEM mode analysis results for the electric field distribution of a ring resonator using an axial symmetric configuration.

4.3 Integrated polymeric waveguide with a ring resonator

Very often the coupling though a tapered optical fiber is proposed but using the same physical coupling principle we chose to integrate an optical waveguide into the chip to improve the integration level and the coupling stability. The waveguide configuration on the glass substrate is the same described in paragraph 4.1.2. The WGM cavity is constituted by a low refractive index polymer (Ip-Dip, $n = 1.52$) ring resonator. To increase the mode confinement, an air suspended geometry (instead of a lying cavity on the substrate) has been preferred. In Figure 4.5 the results of the FEM mode analysis is reported. The calculation is an axial symmetric calculation, where the rotation axis is along $x = 0$ direction. The internal radius of the ring pedestal is 16 μm and the ring external radius 20 μm as can be observed in the cross-section image 4.5. Depending on the field polarization, TE mode, with the electrical field component lying in the cavity plane, and TM mode, with the electrical field component perpendicular to the cavity plane can be defined. The cavity can support azimhutal modes and higher order ones in function of the ring thickness. Examples of higher order modes for a cavity thickness of 2 μm are reported in Fig. 4.6.
A critical parameter that is difficult to control with high precision is the coupling distance between the waveguide and the the resonator that determines the coupling regime. A typical configuration to study the physics of the planar whispering-gallery mode (WGM) resonators consists of exciting the cavity modes from an adjacent waveguide and collecting the transmitted light [39]. The resonator waveguide coupling (RWC) takes place via an overlap of the evanescent fields of the waveguide and the resonator optical modes. In an in-plane geometry, where the waveguide and the resonator lay on the same plane, the mode coupling is known to grow exponentially when the gap x between these two is decreased. This behavior has important implications in the amplitude and in the linewidth of resonant dips that appear in the waveguide transmission spectrum $T(\omega)$ at cavity mode frequencies. As the gap x is reduced, the cavity mode linewidth increases monotonically. More important, the transmission T_{dip} at resonance, in turn, vanishes (in an ideal case) at a single critical coupling gap x when the field propagating in the waveguide and the secondary emission by the resonator interfere destructively on the exact resonance. This behavior can also be found looking at the equation Eq. 4.19 that returns a null transmission for $\omega = \omega_0$ and $\tau_{int} = \tau_{ext}$. In-plane geometries are not the only configurations to reach the ring-waveguide coupling. In fact, many examples

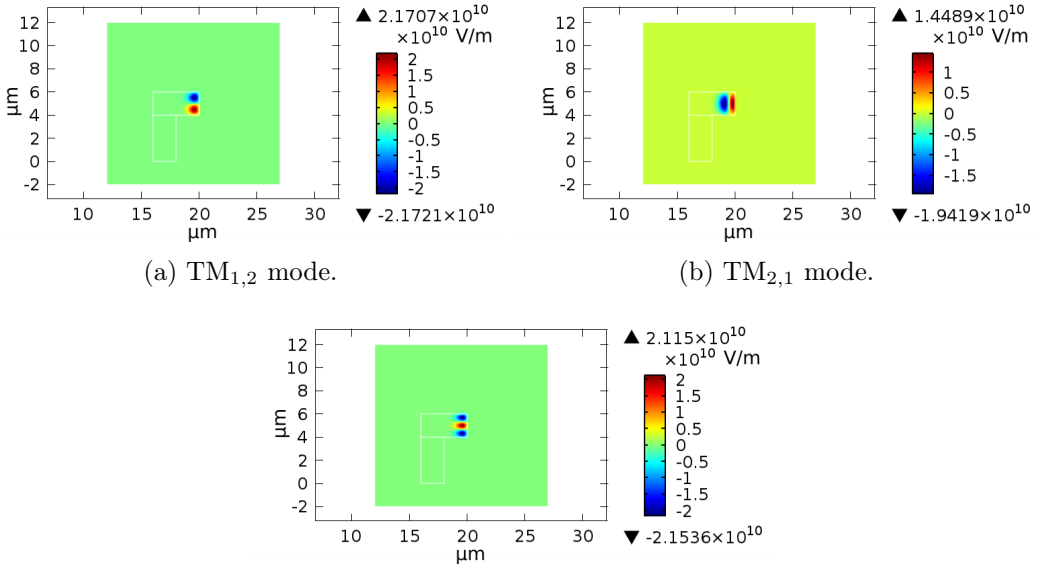

(a) $TM_{1,2}$ mode.

(b) $TM_{2,1}$ mode.

(c) $TM_{1,3}$ mode.

Fig. 4.6: FEM mode analysis results for the electric field distribution of a ring resonator using an axial symmetric configuration. Higher order modes are reported.

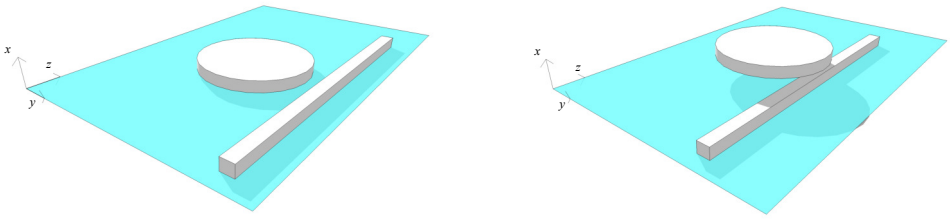

(a) (b)

Fig. 4.7: Sketches of the in-plane (a) and the vertical (b) resonator-waveguide coupling geometries.

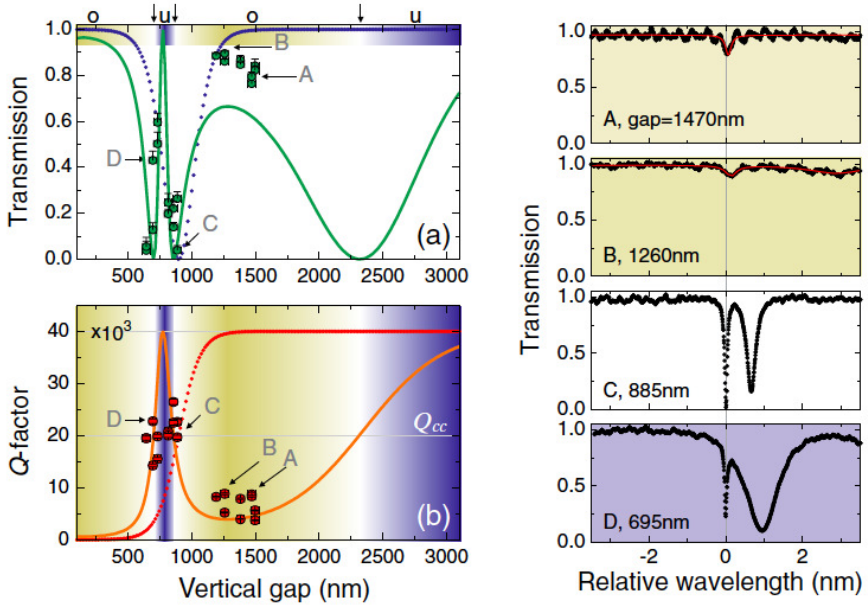

Fig. 4.8: Vertical gap dependence of the resonant transmission T_{dip} (a) and the resonance Q factor (b) for the mode of the wavelength closest to 1.58 μm. Experimental points are compared to the theoretical predictions (solid line). For comparison, the T and Q trends for the point coupling model are reported as dotted lines. The background colors underline the regions where undercoupling (blue), critical coupling (white), and overcoupling (yellow) are expected. The right panels show the experimental spectra around $\lambda = 1.58\,\mu$m for a few specific values of the gap as indicated in the left panels by the A, B, C, D labels: the x-axis zero is set to the center of the resonance dip. (Figure from [43])

in present-day integrated optics can be found of a vertical coupling geometry. In this configuration, the resonator and the waveguide lay on different planes (Figure 4.7) [40–42]. In the vertical coupling scheme, the resonator and the waveguide remains almost at the right distance over a larger distance along the waveguide axis z. Within this flat zone, the waveguide and the resonator can be modeled as a pair of coupled parallel waveguides for which the coupled mode theory predicts a periodic exchange of optical power as a function of the propagation distance [43]. In contrast to the monotonic exponential dependence of the effective RWC in the inplane geometry, the vertical one is characterized by an oscillating effective coupling as a function of vertical gap y, with alternating under-and over-coupling regions, separated by several critical coupling points. Correspondingly, both the cavity mode linewidth and the dip transmission T_{dip} show oscillating dependencies (Figure 4.8). We exploit this advantage to have more ring-waveguide positions to facilitate the achievement of the critical coupling.

4.3.1 The fabrication

Thanks to the potentiality of DLW that consents to create three dimansional structures in one step process, we manage to fabricate firstly the waveguide and subsequently the

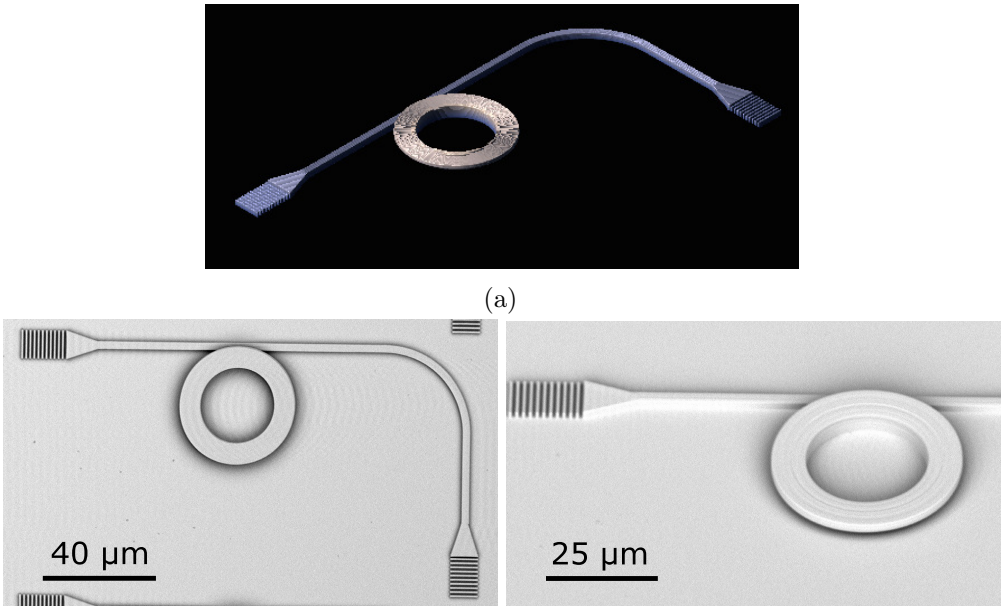

(a)

(b)

(c)

Fig. 4.9: (a) Scheme of waveguide-resonator geometry. This rendering has been created with the commercial software Describe (Nanoscribe GmbH). (b)-(c) SEM images of the waveguide resonator system.

ring resonator (radius 20 μm, height 1.5 μm). We chose a ring height of 1.5 μm that guarantees no higher order modes inside the ring.
A drop of the monomer (Ip-Dip) has been put on the fused silica substrate and glued on the lithographic sample holder. The resist drop in this configuration is in contact with the objective [44] playing also the role of the immersion fluid between the microscope lens ($100X$, $NA = 1.3$ by Zeiss) and the glass substrate. A rendering image of the simple integrated circuit is shown in Figure 4.9.a. The waveguide parameters are the same employed for the devices in Paragragh 4.1.2. Different coupling distances x have been tested to verify the best coupling conditions. But, as demonstrated in [41], also the lateral alignment of the waveguide and the ring strongly affects the coupling. To achieve the best coupling, the maximum intensity of the two modes (the WGM of the cavity and the propagating mode in the waveguide) should be vertically aligned. Also this parameter has been determined though fabrication tests followed by the optical characterizations of the different configuration circuits. The sample after the polymerization is developed in PGMEA and isopropanol and optically characterized. The final device is reported in the SEM images in Figure 4.9.b-c.

4.3.2 The optical characterization

For the WGMR integrated circuits we use a simple transmission setup where some precautions have to be taken. The scheme is reported in Figure 4.10. The circuit has been realized to work in the telecommunication band. The source is a continuous tunable NIR laser (Photonetics TUNICS-plus SC) with a tunable range from 1460 nm up to

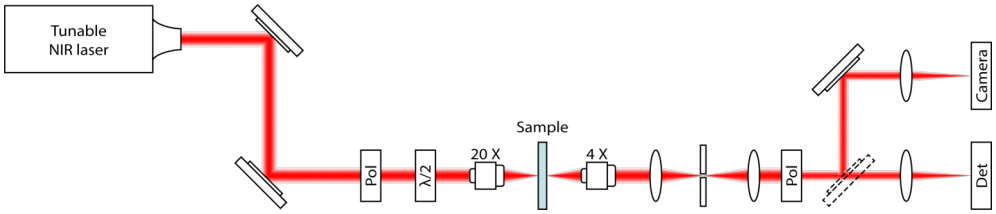

Fig. 4.10: Scheme of experimental setup for the spectral characterization of the integrated waveguide-resonator circuits.

1570 nm and a minimum step of 1 pm. The laser light is not polarized so in order to have an impinging TE mode on the input coupler, a polarizer and a half wave plate (for the NIR range) are placed in front of the sample. The light is then focused on the input grating through a 20X objective (Mitutoyo Plan NIR). A 4X objective is used instead to collect the light coming out from the output grating at the end of the waveguide. To selectively detect only the guided light from the 90° bent waveguide, a second polarizer, in a cross-polarization configuration, is placed after the sample. In the sample image plane, a pinhole is positioned to spatially filter the output grating. This image is then reconstructed through a doublet or on the NIR camera (Phoenix Camera System INDIGO) or on the NIR photodiode, using a flipping mirror. The optical image allows to see when the incoming beam is well focused on the input coupler. Once the light is coupled into the waveguide, at the waveguide output grating, a bright spot appears: the guided and transmitted light. The spectral measurement is then realized flipping the mirror that switch the light from the camera to the photo-diode. A wavelength sweep of the tunable laser is set to record the waveguide spectrum. Because of the grating low-efficiency and a resulting low waveguide output, a modulated signal is employed and through a lock-in amplifier the transmission is deconvolved. The waveguide transmission is then normalized to the glass substrate transmitted signal. A typical spectrum is reported in Fig. 4.11. The FSR is 12.5 nm as expected for a WGM cavity with a radius of 20μm and we can therefore estimate the resonant mode effective refractive index $n_{eff} = 1.52$. This value is reasonable because the mode in the cavity is strongly confined and it is not affected by the surrounding air. The measured Q-factor in this case is 43000. The highest Q measured for this sample geometry is $Q = 78000$. Due to the fabrication parameter sweep and the not well reproducible lithographic results, cavities with quality factor from hundreds up to tens of thousands have been fabricated.

Two preliminary results that exploit two different peculiar characteristics of the DLW technique are now described. For the moment a complete characterization is not presented due to the still on-going research. However the fabrication results constitute themselves a first new step for integrating different functionalities on the same substrate.

4.3.3 Vertically coupled cavities

The possibility of creating 3D microstructures pushed forward the integration level. Not only a vertical coupling between the waveguide and the resonator can be realized; in fact a more complex geometry with two vertically coupled WGM resonators was explored. The fabricated structures are reported in Figure 4.12. The lithographic procedure remains the same but another additional critical parameter is added: the coupling distance in

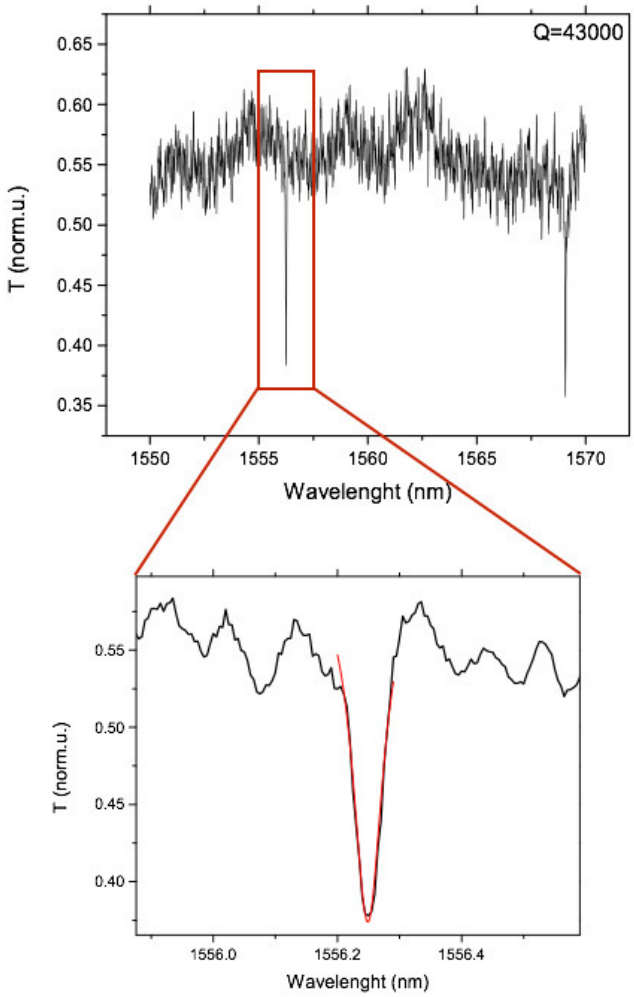

Fig. 4.11: Transmission spectrum of a single mode waveguide vertically coupled to a ring resonator.

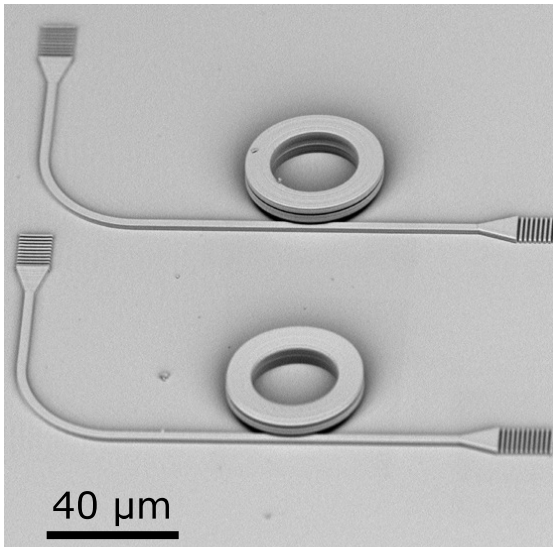

Fig. 4.12: SEM pictures of two vertically coupled cavities. The coupling scheme remains the same as for the single WGM resonantor.

between the two vertically aligned cavities. In this case, due to higher mode confinement inside the ring resonators, the coupling distance should be shorter in order to achieve the overlapping of the resonant mode evanescent tails.

The spectral response of such device is reported in Figure 4.13. Two pairs of dips, with the same width and separated from a spectral distance comparable with expected FRS, are present. We suppose that they can be the fundamental modes of the two vertically coupled cavities but for a certain attribution, further studies are scheduled.

4.3.4 LCE integrated ring resonators

It has already been demonstrated the possibility to fabricate with the DLW different structures on different substrates [16, 45]. But here we demonstrate that in a two step process, structures made of different materials can be polymerized on the same substrate. In particular a polymeric waveguide, as the one previously described, and a liquid crystalline elastomeric ring resonator have be realized (Figure 4.14). The LCE structure shows a quite smooth surface that does not many losses to the resonant mode. In fact a quality factor of 19000 has been measured. In the spectrum, however, many higher order modes appear due the higher refractive index material and a larger ring thickness caused by the swelling of liquid crystalline monomers inside the polymerized network (during the writing process, see Paragraph 2.2.3). For the moment, the possibilty of tuning the resonant features has not been evaluated but it will introduce the variation of many parameters as the refractive index, the resonator shape and the coupling distance. For this complexity, we evaluate that a different geometry should be explored as described in Chapter 5.

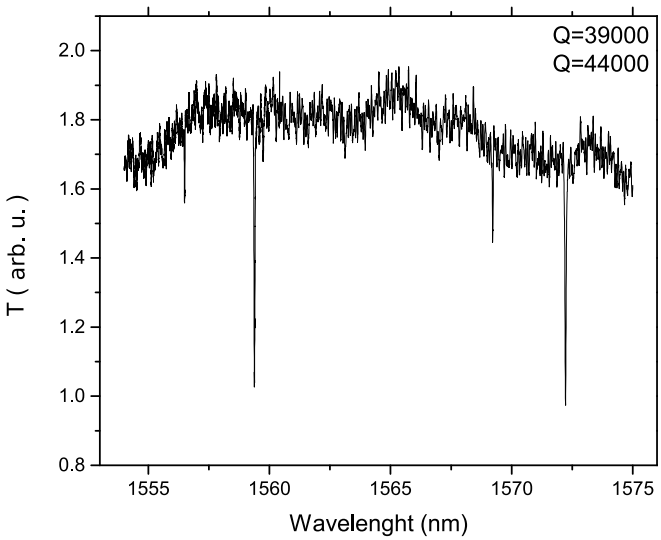

Fig. 4.13: Transmission spectrum of a single mode waveguide vertically coupled to two ring resonators.

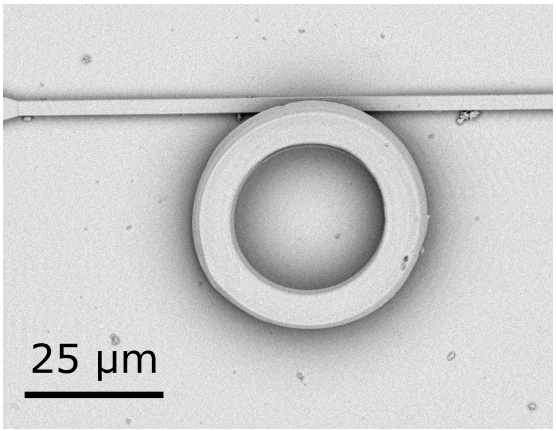

Fig. 4.14: SEM image of a LCE WGM resonator.

References

[1] E. Hecht and A. Zajac. *Optics*. Addison-Wesley publishing company, 1974.

[2] K. Okamoto. *Fundamentals of optical waveguides*. Academic press, 2010.

[3] A. Yariv. "Coupled-mode theory for guided-wave optics". In: *IEEE Journal of Quantum Electronics* 9.9 (1973), pp. 919–933.

[4] B. E. Saleh, M. C. Teich, and B. E. Saleh. *Fundamentals of photonics*. Vol. 22. Wiley New York, 1991.

[5] D. Marcuse. *Light transmission optics*. Van Nostrand Reinhold New York, 1972.

[6] A. W. Snyder and J. Love. *Optical waveguide theory*. Springer Science & Business Media, 2012.

[7] E. A. Marcatili. "Dielectric rectangular waveguide and directional coupler for integrated optics". In: *Bell System Technical Journal* 48.7 (1969), pp. 2071–2102.

[8] V. Braginsky, M. Gorodetsky, and V. Ilchenko. "Quality-factor and nonlinear properties of optical whispering-gallery modes". In: *Physics Letters A* 137.7-8 (1989), pp. 393–397.

[9] G. Griffel et al. "Morphology-dependent resonances of a microsphere–optical fiber system". In: *Optics Letters* 21.10 (1996), pp. 695–697.

[10] G. Maire et al. "High efficiency silicon nitride surface grating couplers". In: *Optics express* 16.1 (2008), pp. 328–333.

[11] D. Taillaert et al. "Grating couplers for coupling between optical fibers and nanophotonic waveguides". In: *Japanese Journal of Applied Physics* 45.8R (2006), p. 6071.

[12] X. Chen et al. "Apodized waveguide grating couplers for efficient coupling to optical fibers". In: *IEEE Photonics Technology Letters* 22.15 (2010), pp. 1156–1158.

[13] F. Van Laere et al. "Compact and highly efficient grating couplers between optical fiber and nanophotonic waveguides". In: *Journal of Lightwave Technology* 25.1 (2007), pp. 151–156.

[14] S. K. Selvaraja et al. "Highly efficient grating coupler between optical fiber and silicon photonic circuit". In: *Conference on Lasers and Electro-Optics*. Optical Society of America. 2009, CTuC6.

[15] H. Zhang et al. "Efficient silicon nitride grating coupler with distributed Bragg reflectors". In: *Optics express* 22.18 (2014), pp. 21800–21805.

[16] M. Schumann et al. "Hybrid 2D-3D optical devices for integrated optics by direct laser writing". In: *Light: Science and Applications* 3.6 (2014), e175.

[17] L. Rayleigh. "The problem of the whispering gallery". In: *Scientific Papers* 5 (1912), p. 617.

[18] S. McCall et al. "Whispering-gallery mode microdisk lasers". In: *Applied physics letters* 60.3 (1992), pp. 289–291.

[19] V. Sandoghdar et al. "Very low threshold whispering-gallery-mode microsphere laser". In: *Physical Review A* 54.3 (1996), R1777.

[20] J. Zhu et al. "On-chip single nanoparticle detection and sizing by mode splitting in an ultrahigh-Q microresonator". In: *Nature Photonics* 4.1 (2010), pp. 46–49.

[21] J. Su, A. F. Goldberg, and B. M. Stoltz. "Label-free detection of single nanoparticles and biological molecules using microtoroid optical resonators". In: *Light: Science & Applications* 5.1 (2016), e16001.

[22] S. Weis et al. "Optomechanically induced transparency". In: *Science* 330.6010 (2010), pp. 1520–1523.

[23] S. Spillane, T. Kippenberg, and K. Vahala. "Ultralow-threshold Raman laser using a spherical dielectric microcavity". In: *Nature* 415.6872 (2002), pp. 621–623.

[24] K. J. Vahala. "Optical microcavities". In: *Nature* 424.6950 (2003), pp. 839–846.

[25] M. Bayer et al. "Inhibition and enhancement of the spontaneous emission of quantum dots in structured microresonators". In: *Physical review letters* 86.14 (2001), p. 3168.

[26] D. Van Thourhout and J. Roels. "Optomechanical device actuation through the optical gradient force". In: *Nature Photonics* 4.4 (2010), pp. 211–217.

[27] T. J. Kippenberg and K. J. Vahala. "Cavity opto-mechanics". In: *Optics Express* 15.25 (2007), pp. 17172–17205.

[28] D. Armani et al. "Ultra-high-Q toroid microcavity on a chip". In: *Nature* 421.6926 (2003), pp. 925–928.

[29] T. Grossmann et al. "High-Q conical polymeric microcavities". In: *Applied Physics Letters* 96.1 (2010), p. 013303.

[30] J. Wang et al. "Optical microcavities with tubular geometry: properties and applications". In: *Laser & Photonics Reviews* 8.4 (2014), pp. 521–547.

[31] M. Sumetsky. "Whispering-gallery-bottle microcavities: the three-dimensional etalon". In: *Optics letters* 29.1 (2004), pp. 8–10.

[32] M. Sumetsky. "Mode localization and the Q-factor of a cylindrical microresonator". In: *Optics letters* 35.14 (2010), pp. 2385–2387.

[33] W. Lee et al. "A quasi-droplet optofluidic ring resonator laser using a micro-bubble". In: *Applied Physics Letters* 99.9 (2011), p. 091102.

[34] G. Righini et al. "Whispering gallery mode microresonators: fundamentals and applications". In: *Rivista del Nuovo Cimento* 34.7 (2011), pp. 435–488.

[35] S. Yang, Y. Wang, and H. Sun. "Advances and prospects for whispering gallery mode microcavities". In: *Advanced Optical Materials* 3.9 (2015), pp. 1136–1162.

[36] L. Collot et al. "Very high-Q whispering-gallery mode resonances observed on fused silica microspheres". In: *EPL (Europhysics Letters)* 23.5 (1993), p. 327.

[37] Y. Ido et al. "Reduced lasing threshold in thiophene/phenylene co-oligomer crystalline microdisks". In: *Applied physics express* 3.1 (2009), p. 012702.

[38] H. A. Haus. *Waves and fields in optoelectronics*. Prentice-Hall, 1984.

[39] A. B. Matsko. *Practical applications of microresonators in optics and photonics*. CRC Press, 2009.

[40] B. Little et al. “Vertically coupled glass microring resonator channel dropping filters”. In: *IEEE Photonics Technology Letters* 11.2 (1999), pp. 215–217.

[41] M. Ghulinyan et al. “Monolithic whispering-gallery mode resonators with vertically coupled integrated bus waveguides”. In: *IEEE Photonics Technology Letters* 23.16 (2011), pp. 1166–1168.

[42] F. Ramiro-Manzano et al. “A fully integrated high-Q whispering-gallery wedge resonator”. In: *Optics express* 20.20 (2012), pp. 22934–22942.

[43] M. Ghulinyan et al. “Oscillatory vertical coupling between a whispering-gallery resonator and a bus waveguide”. In: *Physical review letters* 110.16 (2013), p. 163901.

[44] T. Bückmann et al. “Tailored 3D mechanical metamaterials made by dip-in direct-laser-writing optical lithography”. In: *Advanced Materials* 24.20 (2012), pp. 2710–2714.

[45] T. Grossmann et al. “Direct laser writing for active and passive high-Q polymer microdisks on silicon”. In: *Optics express* 19.12 (2011), pp. 11451–11456.

CHAPTER 5

Ring resonators as polymeric active cavities

The application fields of whispering gallery mode resonators are not limited to passive elements in integrated circuits. In fact many examples of active devices based on axial symmetric resonators have been demonstrated. Polymeric microcavities, for example, enable straightforward integration of additional gain media, offering new possibilities for the realization of optically pumped, low-cost coherent light sources on a chip. WGMR micro lasers constitute a fascinating application because of their small mode volume and their easily integrability. Using e-beam lithography, polymeric dye doped cavity with a high quality factor can be fabricated. The Q factors achieved by this method are on the order of 10^6 *and one of their relevant property is the low laser threshold power. As for any emitting source, tunability is an important feature in order to control the light emitted wavelength. In this chapter we demonstrate that optical tuning of the resonant frequency can be achieved by the integration of photo-responsive liquid crystalline elastomer micro-structure into dye-doped polymeric micro-goblet cavity. The LCE micro cylinder is fabricated with the direct laser writing technique and placed on the polymeric cavity. This generates the possibility of a non-invasive light-driven reshaping of the cavity and thus a fully reversible tuning of the lasing modes. The micro-laser, we present, is compact, reliable, tunable over a large spectral range and can be completely implemented in integrated optical circuits as tunable emitting source. The same tuning principle can be transferred to passive cavities leading to the realization of optically tunable filters, devices largely employed in the existing telecommunication filter technology. With this technique we demonstrate a new method to optically control the optical path length of high quality factor cavities that can be potentially integrated in many other different photonic devices. This work has been done in collaboration with the group of Prof. H. Kalt (KIT, Karlsruhe Institute of Technology).*

5.1 Active whispering gallery mode resonators

The broad diffusion of whispering gallery mode resonator (WGMR) devices, as the micro-laser we proposed, is motivated by their small mode volume and high quality factor. The high quality factor of the resonators allows for significant reduction of the lasing threshold. Adding laser dyes [1–3], quantum dots [4, 5] or quantum wells [6] to the polymeric/semiconductor matrix, they can be turned from passive cavities into WGM micro-laser.
The first WGM lasers were realized in solid materials [7, 8] but more recently also WGM-based lasers occurred in liquid aerosols and individual liquid droplets [9, 10]. The advantage of using polymeric based matrices for the cavities fabrication is given by the possibility of a lasing wavelengths in the whole visible spectrum due to easy doping of polymers with various dye molecules, which exhibit high internal quantum efficiencies [11, 12].
In literature there are many demonstration of different geometries and different active media but, inside this work, we focus on the possibility of tuning the lasing wavelength.

5.2 Tunable WGMR

The stable and reversible optical tuning of the characteristic sharp resonance increases the cavity functionality and makes them highly attractive for both fundamental physics and applications in optical sensing or communication technology. The demonstrated cavity tunability is different for semiconductor-based WGM resonators where tuning of the cavity resonances is achievable by temperature-, field- or carrier-induced changes of the optical properties [13–16].
Liquid WGM resonators have been tuned by changing the size of the droplet resonators [17] or by mechanical size stretching[18, 19]. But functional facility and reversibility are difficult to attain. By utilizing the birefringence and electric-field induced structural deformation of liquid crystals (LCs), researchers also reported shifting of cavity modes using LCs as a cladding layer [20], LC-droplet resonators [10] or by immersing semiconductor microcavities in LC solution [21]. However, all these methods do not show controllable reversible tunability and are not suitable to be integrated into a single on-chip device at the same time. We will introduce a possibility for reversible, dynamic tuning of polymeric WGM resonators. This tunability is based on the photo-induced shape modification of liquid crystalline elastomer (LCE) actuators integrated into goblet resonators.

5.3 A LCE actuator to remotely tune a goblet micro-laser

We achieved a control on the emitted wavelength all along the WGM free spectral range through an elastomeric micro-actuator. A new concept for control of the resonant wavelength over a large spectral range exploiting a light-induced elastic deformation is developed. Optical tuning is achieved by integration of photo-responsive liquid crystalline elastomer micro-structures into micro-goblet active cavities.

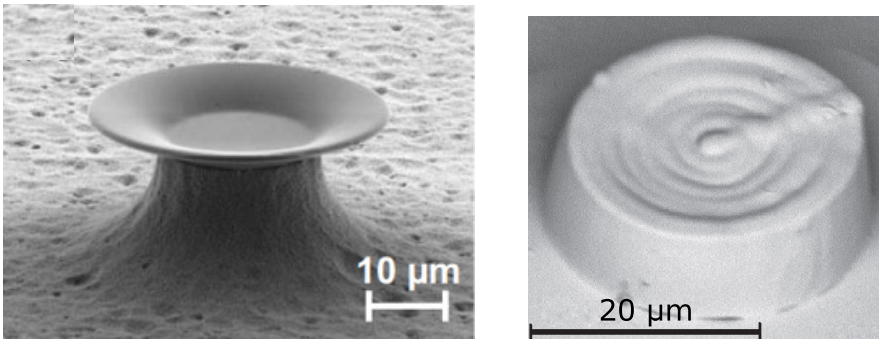

(a) (b)

Fig. 5.1: SEM images of (a) a micro-goblet resonator obtained by e-beam lithography and (b) a LCE micro-cylinder patterned by DLW.

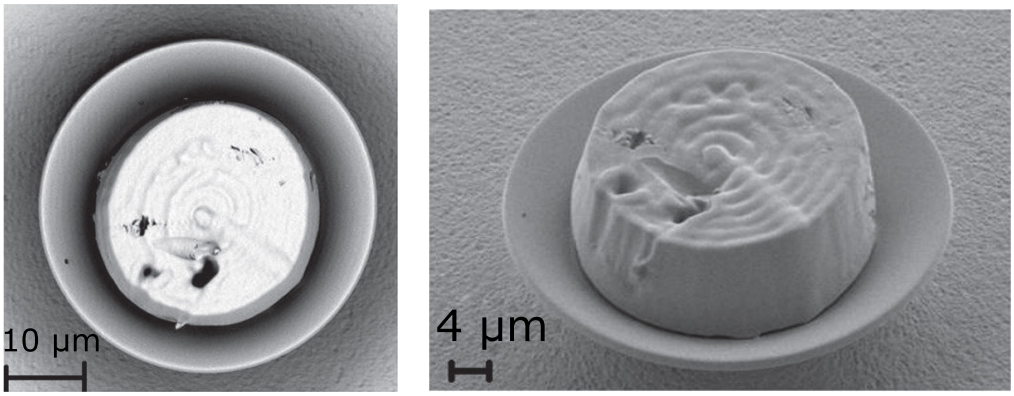

(a) (b)

Fig. 5.2: SEM images of the micro-goblet resonator and the LCE actuator in the center: (a) top view and (b) top-side view.

5.3.1 The sample fabrication

The polymeric WGM resonators are lithographically structured Poly(methyl methacrylate) (PMMA) disks on a silicon chip using a subsequent thermal procedure to achieve the goblet-type cavity geometry [22] (Figure 5.1.a). These resonators are compatible with large-scale fabrication and are mechanically stable and they are fabricated as active polymeric WGM lasers. To achieve the lasing property, the laser dye Pyrromethene 597 (PM 597) was doped into the PMMA host matrix with a dye concentration of 12 μmol/g solid PMMA. This laser dye emits in the visible spectrum near 600 nm, has a high molar absorption coefficient ($\sim 10^5$ $M^{-1}cm^{-1}$) and near unity quantum yield [23].The doped PMMA (MicroChem PMMA 950k A7 dissolved in anisole) (Micro Resist Technology GmbH, Berlin, Germany) is spin coated on the top of a silicon wafer to result in a 1 mm thick layer. Circular resonator structures are patterned into the PMMA layer using e-beam lithography (with a dose current of 500 pA). Developing the sample and isotropically etching the exposed silicon using XeF_2 results in polymeric micro-disk resonators on a silicon pedestals (see [22]).

Tunability of the cavity resonances is linked to the control of the resonator diameter. To this end, a photoresponsive smart material, the nematic LCE containing an azo-dye is integrated into the goblet geometry. In order to achieve this purpose a second constituent of each tunable resonator, namely the photo-responsive nematic LCE micro-cylinders is produced using two-photon absorption induced polymerization of LC mixtures with direct laser writing (DLW) (Figure 5.1.b). In this case, since the actuating part does not have any photonic propertied and no good resolution properties are required indeed, the chosen LCE mixture is MM-20 (see 2.2.3), that does not possess a good rigidity but its deformation reaches the 20%. This mixture is infiltrated into a cell made from glass plates with 50 μm gap. The glass plates are coated with special polyimide (PI1211 Nissan Chemical Industries) to initiate 90° pretilt angle uniaxial alignments of the LC molecules (perpendicular to the glass substrate). Two photon absorption polymerization of the infiltrated LC monomer mixture was induced the DLW work station. The LCE micro-cylinder structures were written on the bottom inner surface of the glass plate, and the sample position is controlled by 3D piezo translational stage. DLW followed by developing the sample with toluene leads to LCE micro-cylinder structures. The molecular alignment is along the axis of the cylinder. After fabrication by DLW, the LCE cylinders are centered on top of the PMMA micro-disk resonators using a micro-positioning system. The cylinders can easily be detached from its glass substrate upon heating the sample to 100℃ for 10–15 min. We used micro-tips (made from optical fibers) to place the LCE micro-cylinders on top of polymeric micro-disk resonators as shown in Figure 5.2. The next step is a thermal reflow treatment which leads to the surface-tension induced goblet structure, smoothens the surface of the cavity and fuses the LCE into the base of the goblet resonator. To this end the resonators are placed for 30–40 s on a hot plate at temperature of 125℃ (slightly above the glass transition temperature of PMMA). The shape transition reduces the diameter of the cavity to 45 μm. SEM images of a LCE/goblet resonator are shown in Figure 5.2.

5.3.2 The optical characterization

Quality factor measurement

The first test that has been performed on such cavities is the quality factor measurement of both the passive and the active ones to evaluate how the dye introduction can perturb the optical quality of this resonator. For such passive cavities a quality factor of 10^6 has been measured [22] while the dye doped PMMA matrix lowers the cavity quality factor to 10^4. It is important to test whether the optical quality of the goblet resonators is affected by the integration of the LCE micro-cylinders. To measure the Q factor, we used a tapered fiber to evanescently couple visible light (of wavelength around 630 nm) into the LCE/microgoblet resonator.

The transmitted light is collected via a photo-diode (the experimental set-up is shown in Fig. 5.3). The transmission spectrum (Figure 5.4) of the fiber recorded with a narrow-band, continuously swept tunable diode laser (632.5˘637 nm) reveals the typical WGM structures including fundamental as well as higher order resonator modes. The free spectral range ($\delta\lambda_{FSR}$), which is observed from the periodic repetition of the modal pattern, is 1.95 nm near 635 nm wavelength range. This is in a good agreement with the theoretically expected value of 1.90 nm for a 45 μm diameter PMMA based micro-

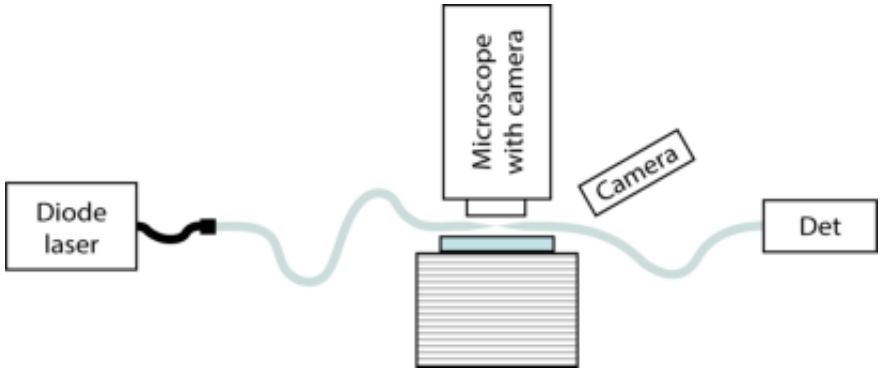

Fig. 5.3: Optical setup used for the cavity quality factor measurement.

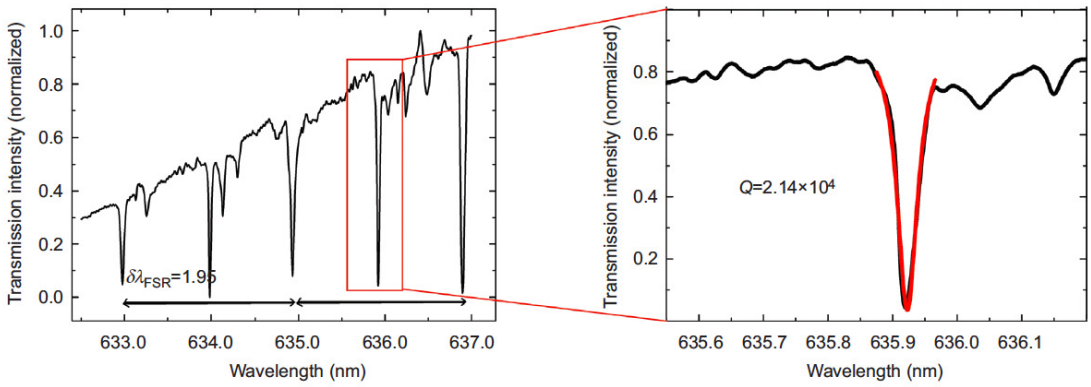

Fig. 5.4: Transmission spectrum of a tapered fiber coupled to a passive goblet PMMA resonator with a LCE actuator in the center. In the right inset the resonance dip with the Lorentzian fit is reported.

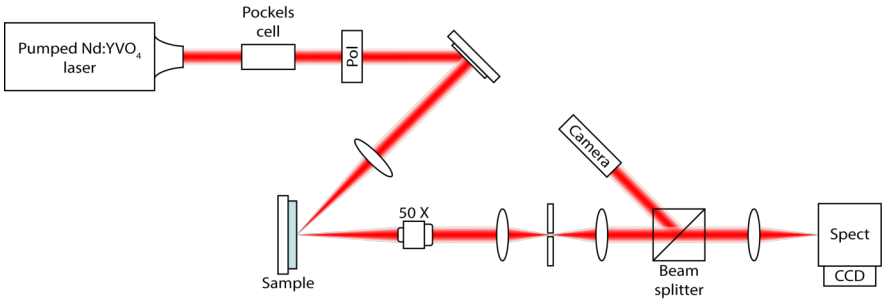

Fig. 5.5: Experimental micro-photoluminescence setup.

goblet. The Q factor is determined from the full width at half maximum of one of the Lorentzian-shaped resonances (see inset of Figure 5.4). We find a Q factor of about 2.143104 which is in similar order to the Q factor achieved for dye-doped polymeric resonators without LCEs. The Q factor obviously does not deteriorate which is actually no surprise since the WGMs are confined near the rim of the cavity.

The lasing and the tuning

Illumination of the LCE/PMMA goblet resonators with nanosecond laser pulses in the green spectral range has two consequences. First one, the LCE exhibits a pronounced photo-induced mechanical deformation: the LCE micro-cylinder shows a radial expansion perpendicular to the alignment of the LCE molecules and a simultaneous contraction parallel to the cylinder axis. Second the PM 597 dye-doped polymeric cavity is pumped into laser emission. It is important to note the involved time scales of the experiment: the time scale for the thermal response of the LCE is long compared to the temporal spacing of the pump pulses nanosecond excitation. The (stimulated) recombination time of the excited laser dye, however, is short compared to the nanosecond pulse duration. Thus, LCE/goblet laser system can be operated under controlled quasi-stationary conditions. The LCE/PMMA micro-goblet laser cavities were pumped with 10 ns pulses from a frequency-doubled neodymium-doped yttrium orthovanadate (Nd:YVO_4) laser at a pump wavelength of 532 nm and a repetition rate of 1 kHz. The pulse duration below 100 ns is essential to prevent triplet formation of the dye molecules, which would inhibit lasing. The excitation pump beam is focused in a free-space micro-photoluminescence (μ-PL) set-up under an angle of 45° to a spot size of about 65 μm diameter to achieve nearly homogeneous excitation of the whole cavity .[1] The emission from the cavity is collected perpendicular to the resonator axis by a microscope objective of $NA = 0.4$ (50X) and directed to a spectrometer (grating with $1200 lines \cdot \mathrm{mm}^{-1}$, of resolution 60 pm) equipped with CCD (charge coupled device) camera. This set-up also provides spatially resolved information about the emitted laser mode distribution along the vertical diameter of the cavity utilizing the dimension of the CCD pixel array parallel to the alignment of the spectrometer entrance slit. This data are not reported here but can be found in [24].

[1] The laser cavity and the LCE are here pumped by the same laser pulse. This is due to the fact that the azo-dye had to be chemically modified by changing its aromatic ring to shift the absorption wavelength. For realistic applications, it is straightforward to separate the excitation of the laser and the LCE, e.g., by splitting the beam and chose different foci

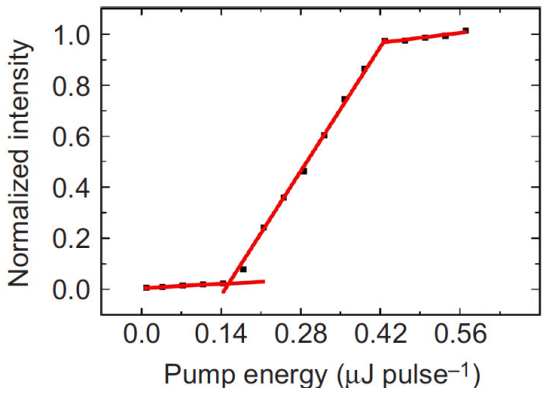

Fig. 5.6: Input–output curve of a PM 597 dye-doped LCE/PMMA goblet micro-laser.

The experimental setup is shown in Figure 5.5. The excitation energy density of the pump laser was varied using a Pockels cell along with a linear polarizer. The output emission of the microcavity was then recorded as a function of the pump energy deposited on the cavity per pulse. A characteristic input-output curve of LCE/PMMA micro-goblet dye laser is depicted in Figure 5.6. The output intensity at certain pump energy was determined by integrating the intensity of a single lasing mode. The onset of lasing was inferred from the super-linear increase of the intensity resulting from the dominance of stimulated emission over spontaneous emission. The lasing threshold was found to be 0.14 $\mu J\ pulse^{-1}$. The wavelengths of the laser modes are stable for fixed pump energy since the thermally determined size of the cavity is stationary for a repetition rate of 1 kHz. For pump energies well above the threshold, several narrow lasing peaks appear in the spectrum. The spectral distance between adjacent lasing peaks is below the free spectral range of the cavity (about 1.7 nm in the displayed wavelength range). This shows that besides the fundamental modes, also several higher order cavity modes contribute to the lasing spectrum well above lasing threshold. The confirmation that the lasing modes are strictly confined near the rim of the goblet resonator and that the LCE micro-cylinder does not affect the modal structure of the cavity is given by the spatially resolved micro-photoluminescence spectroscopy.
The response of the LCE to the optical pumping has significant influence on the spectral position of the cavity resonances. Once reached the mode saturation level (without any further spectrum change due to new emerging modes), continuously increasing the laser power, the LCE deformation causes a laser red shift. In fact, in Figure 5.7, we find a pronounced reversible red shift of the lasing modes. The maximum shift is as high as 3.5 nm for the first mode surpassing lasing threshold. The explanation of such effect has can be found in the pump laser induced local temperature increase. As a result, the aligned molecular network of the LCE, which has been intentionally aligned along the axis of the cylinder, becomes more disordered, evoking an in-plane symmetrical expansion of the microcylinder (see illustration in Figure 5 (right)). This in turn leads to a symmetrical expansion of the goblet resonators and thus the red shift o the lasing modes. The photo-induced change in the shape of the LCE/PMMA goblets is found to be linear dependent on pump energy and perfectly reversible. As the pump energy is decreased,

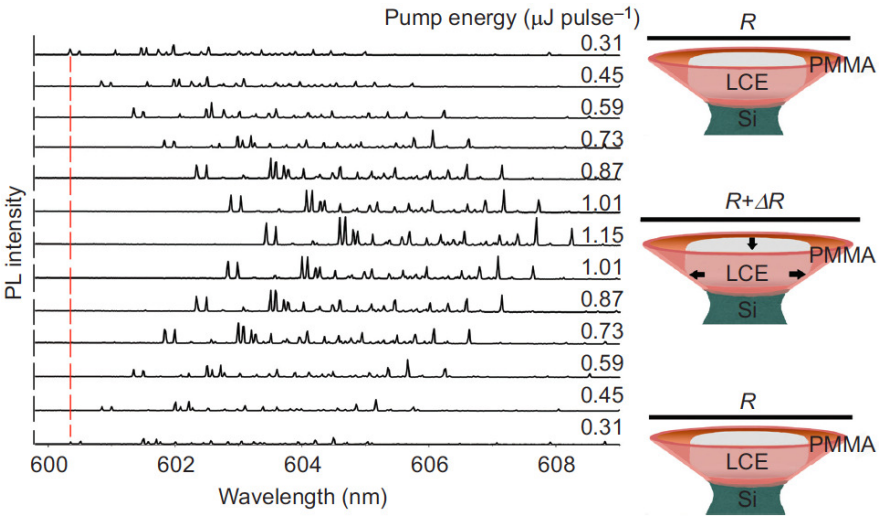

Fig. 5.7: Left: Photo-induced tuning of LCE/goblet laser modes for different pump energies. Increasing the excitation energy from 0.31 mJ $pulse^{-1}$ to 1.15 mJ $pulse^{-1}$ leads to a red shift of the modes of about 3.1 nm. Decreasing the pump power back results in a reversed spectral shift (blue shift). Right: Schematic diagram of LCE/goblet resonators. Increasing the pump energy increases the disorder in the molecular network of the LCE micro-cylinder and leads to a symmetrical expansion of the LCE structure and the goblet resonator. Decreasing the pump power restores the ordered phase of the elastomer, leading to a perfectly reversible resonator size deformation and tuning of the lasing modes.

the decrease in the temperature of LCE micro-cylinder restores the nematic ordering of the LCE and the goblet shrinks back to its original size. The lasing modes show red shift of about 0.51 nm for every increase in the excitation energy by 0.14 μJ $pulse^{-1}$. A decrease in the pump energy by the same amount leads to 100% reversible spectral shift in the first two cycles. Further measurement in the excitation energy density cycles show the reversibility of the laser modes with fluctuations of the exact modal positions in the 0.1 nm range. This corresponds to an expansion (contraction) of the radius of the cavity by nearly 27.3 nm for every 0.1 μJ increase (decrease) in input pump energy for the here discussed regime near the saturation level of the micro-laser.
To really exclude other contributes to the lasing spectral shift, we verified that he modification of the modal wavelengths of the polymeric cavity is not caused by heating of the cavity itself. In principle heat can cause a shift of the cavity modes due to the negative thermo-optic coefficient of PMMA. Thus, we replaced the LCE micro-cylinders by negative photo-resist (IP–L; Nanoscribe GmbH) micro-cylinders of similar size doped with azo-dye (same concentration as in LCE mixture) and fabricated using 3D laser writing. We find no spectral shift of the cavity modes when pumping in the energy-density range used for the experiments described above. Hence, we can exclude a direct heating of the PMMA cavity and the observed spectral shifts of LCE/goblet resonator modes is solely due to the photo-induced deformation of the LCE.
The presented device that combines the lasing properties of high Q dye-doped cavities and the light-induced elastic deformation of LCE microstructure brought to the realization of a tunable micro-laser integrated on a single chip. Thanks to the properties of the DLW system the cylindric actuator can be also realized directly on the top of the resonator (DiLL system, see Paragraph 2.1.1) to facilitate the fabrication process of such device.

References

[1] T. Grossmann et al. "Strongly confined, low-threshold laser modes in organic semiconductor microgoblets". In: *Optics express* 19.10 (2011), pp. 10009–10016.

[2] M. Kuwata-Gonokami. "Laser emission from dye-doped polystyrene microsphere". In: *Lasers and Electro-Optics Society Annual Meeting, 1993. LEOS'93 Conference Proceedings. IEEE*. IEEE. 1993, pp. 300–301.

[3] S. I. Shopova et al. "Optofluidic ring resonator based dye laser". In: *Applied physics letters* 90.22 (2007), p. 221101.

[4] A. Flatae et al. "Strongly confining bare core CdTe quantum dots in polymeric microdisk resonators". In: *APL Materials* 2.1 (2014), p. 012107.

[5] S. Shopova et al. "Microsphere whispering-gallery-mode laser using HgTe quantum dots". In: *Applied physics letters* 85.25 (2004), pp. 6101–6103.

[6] S. McCall et al. "Whispering-gallery mode microdisk lasers". In: *Applied physics letters* 60.3 (1992), pp. 289–291.

[7] C. Garrett, W. Kaiser, and W. Bond. "Stimulated emission into optical whispering modes of spheres". In: *Physical Review* 124.6 (1961), p. 1807.

[8] P. Walsh and G. Kemeny. "Laser operation without spikes in a ruby ring". In: *Journal of Applied Physics* 34.4 (1963), pp. 956–957.

[9] H.-M. Tzeng et al. "Laser emission from individual droplets at wavelengths corresponding to morphology-dependent resonances". In: *Optics letters* 9.11 (1984), pp. 499–501.

[10] M. Humar et al. "Electrically tunable liquid crystal optical microresonators". In: *Nature Photonics* 3.10 (2009), pp. 595–600.

[11] A. Kurian et al. "Studies on fluorescence efficiency and photodegradation of rhodamine 6G doped PMMA using a dual beam thermal lens technique". In: *Laser Chemistry* 20.2-4 (2002), pp. 99–110.

[12] M. Fischer and J. Georges. "Fluorescence quantum yield of rhodamine 6G in ethanol as a function of concentration using thermal lens spectrometry". In: *Chemical physics letters* 260.1 (1996), pp. 115–118.

[13] Q. Chang et al. "A tunable broadband photonic RF phase shifter based on a silicon microring resonator". In: *IEEE Photon. Technol. Lett* 21.1 (2009), pp. 60–62.

[14] H. Tapalian, J.-P. Laine, and P. Lane. "Thermooptical switches using coated microsphere resonators". In: *IEEE photonics technology letters* 14.8 (2002), pp. 1118–1120.

[15] D. Armani et al. "Electrical thermo-optic tuning of ultrahigh-Q microtoroid resonators". In: *Applied physics letters* 85.22 (2004), pp. 5439–5441.

[16] A. Guarino et al. "Electro–optically tunable microring resonators in lithium niobate". In: *Nature Photonics* 1.7 (2007), pp. 407–410.

[17] S. K. Tang et al. "Continuously tunable microdroplet-laser in a microfluidic channel". In: *Optics express* 19.3 (2011), pp. 2204–2215.

[18] M. Saito, H. Shimatani, and H. Naruhashi. "Tunable whispering gallery mode emission from a microdroplet in elastomer". In: *Optics express* 16.16 (2008), pp. 11915–11919.

[19] R. Chen, H. D. Sun, et al. "Tuning whispering gallery mode lasing from self-assembled polymer droplets". In: *Scientific reports* 3 (2013), p. 1362.

[20] C.-T. Wang et al. "Optical bistability in a silicon nitride microring resonator with azo dye-doped liquid crystal as cladding material". In: *Optics express* 21.9 (2013), pp. 10989–10994.

[21] K. A. Piegdon et al. "Tuning quantum-dot based photonic devices with liquid crystals". In: *Optics express* 18.8 (2010), pp. 7946–7954.

[22] T. Grossmann et al. "High-Q conical polymeric microcavities". In: *Applied Physics Letters* 96.1 (2010), p. 013303.

[23] J. Banuelos Prieto et al. "Photophysical properties of the pyrromethene 597 dye: solvent effect". In: *The Journal of Physical Chemistry A* 108.26 (2004), pp. 5503–5508.

[24] A. M. Flatae et al. "Optically controlled elastic microcavities". In: *Light: Science & Applications* 4.4 (2015), e282.

CHAPTER 6

Conclusions and further prospectives

In this work we deeply investigated the macro and micro-scale properties of a unique class of materials, liquid crystalline elastomers, in order to modulate their chemical and physical properties for the realization of photonic devices. To achieve this ambitious goal, material characterization has been carried out to test and optimize the fabrication strategy, a commercial laser writing lithographic technique, and to determine the suitable parameters for the generation of structures with desired and customized properties. In this way three dimensional prototypes of different materials have been obtained, allowing to combine the best material choice and the fabrication procedure, to reach the required lithographic resolution. The first proof of concept demonstration was the preparation of photonic structures such as 2D optical tunable beam steering devices that we characterized through an analysis of light-driven beam angular deviation, photo-bleaching effects and temporal steering dynamics. Another class of photonic devices largely employed in the integrated circuits are whispering gallery mode resonators. For their small mode volume and large quality factors, they are employed both as passive devices, for example in filtering and sensing application, and as active cavities. Firstly, a study of the physical behavior of a polymeric ring resonator employed as a passive cavity in the vertical coupling configuration with a single mode waveguide is reported. The characterization showed that with the designed polymer fabrication procedure and spatial design a Q factor of 78000 can be reached. This investigation on passive structures has been then expanded towards active cavities. We demonstrated the use of LCE actuators to remotely tune the lasing wavelength of a goblet micro laser. This thesis, at its end, resulted in the investigation and demonstration of the application of unique materials, as liquid crystal elastomers, for optically controlled photonic applications. This is a active research field and our studies open to many other applications. For example, we would like to mention the possibility of using liquid crystal elastomer as polymeric matrix for the realization of tunable three dimensional photonic crystals. Moreover the material research can improve polymeric properties as resolution and elasticity, allowing

to fabricate more challenging structures.

List of publications

- Nocentini S., Martella D., Parmeggiani D., & Wiersma D.S. Photoresist design for elastomeric light tunable photonic devices. *Materials* **9**,7, 525 (2016)
- Nocentini S., Martella D., Parmeggiani D., Zanotto S. & Wiersma D.S. Towards liquid crystalline elastomer optically tunable photonic microstructures. *SPIE Nanoscience+ Engineering*, 992025 (2016)
- Flatae A. M., Burresi M., Zeng H., Nocentini S., Wiegele S., Parmeggiani C. Kalt H. & Wiersma D.S. Optically controlled elastic microcavities. *Light: Science and Applications* **4**, e282 (2015)
- Flatae A. M., Burresi M., Zeng H., Nocentini S., Wiegele S., Parmeggiani C. Kalt H. & Wiersma D.S. Optically controlled elastic microcavities. *Conference on Lasers and Electro-Optics Europe - Technical Digest 2014-January*, 6989248 (2014)